6

Dielectric Spectroscopy on Emulsion and Related Colloidal Systems—A Review

Yuri Feldman
The Hebrew University of Jerusalem, Jerusalem, Israel

Tore Skodvin
University of Bergen, Bergen, Norway

Johan Sjöblom
Statoil A/S, Trondheim, Norway

I. INTRODUCTION

In general, there seems to be a shortage in modern process industry of elegant and nonintrusive techniques to describe accurately the process with regard to yield, competing reactions, external parameters, contaminations, and formation of disturbing colloidal states. It goes without saying that the development of such techniques will highly secure the success of many uncertain processes in operation today. In reviewing possible techniques one can point out dielectric (or capacitance), ultrasound, and analytical techniques, together with spectroscopic alternatives.

In this review we have chosen to highlight the pros and cons of dielectric spectroscopy applied to emulsified and related systems. The reason for the choice of these systems is that they represent multiphase systems containing phase boundaries or interfaces. It is shown that dielectric spectroscopy scanning over large frequency intervals (from some kilohertz up to several gigahertz) is extremely sensitive towards interfacial phenomena and interfacial polarization. Hence, there exist many possibilities for this technique to map processes taking place in the bulk phases as well as at the phase boundaries. This is one of several reasons why the technique is so powerful and frequently used in the study of heterogeneous systems.

In a large number of processes, one factor determining failure or success may be the state of colloids present in the system at some stage in the process. This is true whether the process is the manufacture of pharmaceuticals, application of paint, separation of water from crude oil, blood flow, preparation of carrier matrices for catalysts, preparation of novel materials, food production, etc. (the list could be expanded several times without becoming complete). Even though the science of colloids has reached a high level of sophistication, new or improved techniques that can shed light on the complex and highly dynamic interactions taking place in colloidal systems are still needed.

In the following we combine dielectric spectroscopy and colloidal systems. We belive this to be a fruitful combination of two highly important and current topics. Dielectric measurements have roots from over a hundred years ago; in the belinning of course only simple capacitance measurements were made. However, the findings made especially

on more complex systems encouraged scientists to analyze the physics and chemistry of what we call heterogeneous systems. A prediction of the dielectric properties of such systems was a main concern of scientists such as Maxwell, Wagner, Debye, and Sillars. Historically, we find a genuine interest in understanding dielectric properties of chemically very intricate systems. Depending on the problem, either the theory or the experiments have been in the lead.

Today, both dielectric measurements and colloidal systems (as a representative of heterogeneous systems) are of great interest both with regard to basic as well as applied science.

Dielectric measurements have developed from cumbersome Wheatstone-bridge measurements to an efficient, precise, and rapid spectroscopic technique. The new technique dielectric spectroscopy soon found interesting applications within the field of colloid chemistry. The technique can be applied as a precision method in a thorough mapping of the static and dynamic properties of colloidal systems. Industrially, dielectric measurements can be utilized in the online characterization of such complex systems.

First, we give an introduction to the basic concepts underlying the measuring technique, before the technique itself is reviewed. Finally, experimental work is presented. The experimental part has three main sections, i.e., one section covers equilibrium systems, in the second non-equilibrium systems are regarded and the last one is on the application of dielectric spectroscopy to biological systems.

In the writing of this review we have not sought to cover every aspect of the dielectric properties of colloidal systems. Our aim has rather been to demonstrate the usefulness of dielectric spectroscopy for such systems, using the application to selected systems as illustrations.

II. DIELECTRIC POLARIZATION —- BASIC PRINCIPLES

Recently a new field, mesoscopic physics, has emerged. It is interesting to understand the physical properties of systems that are not as small as a single atom, but small enough that the properties can be dramatically different from those in a larger assembly. All these new mesoscopic phenomena can easily be observed in the dielectric properties of colloid systems. Their properties strictly depend on the dimensional scale and the time scale of observation. Self-assembling systems such as micellar surfactant solutions, microemulsions, emulsions, aqueous solutions of biopolymers, and cell and lidposome suspensions all together represent this population of complex liquids that have their almost unique dynamic and structural properties emphasized on the mesoscale.

Consequently, let us consider different types of polarization that can take place in such structures. There can be two considerations in this case. One from a phenomenological point of view, in terms of the macroscopic polarization vector, another from the molecular point of view, taking into account all possible contributions to the macroscopic polarization vector of unit sample volume.

A. Dielectric Polarization in Static Electric Fields

Being placed in an external electric field, a dielectric sample acquires a nonzero *macroscopic dipole moment*. This means that the dielectric is polarized under the influence of the field. The polarization P of the sample, or dipole density, can be presented in a very simple way:

$$\boldsymbol{P} = \frac{\boldsymbol{M}}{\boldsymbol{V}} \tag{1}$$

where M is the macroscopic dipole moment per unit volume, and V is the volume of the sample. In a linear approximation the polarization of the dielectric sample is proportional to the strength of the applied external electric field E(1):

$$\boldsymbol{P} = \chi \boldsymbol{E} \tag{2}$$

where × is the *dielectric susceptibility* of the material. If the dielectric is isotropic, x is scalar, whereas for an anisotropic system x is a tensor.

In the Maxwell approach, in which matter is treated as a continuum, we must in many cases ascribe a dipole density to matter. Let us compare the vector fields D and E for the case in which only a dipole density is present. Differences between the values of the field vectors arise from differences in their sources. Both the external charges and the dipole density of the sample act as sources of these vectors. The external charges contribute to D and E in the same manner (2). The electric displacement (electric induction) vector D is defined as

$$\boldsymbol{D} = \boldsymbol{E} + 4\pi \boldsymbol{P} \tag{3}$$

For a uniform isotropic dielectric medium, the vectors D, E, P have the same direction, and the susceptibility is coordinate independent, therefore

$$\boldsymbol{D} = \boldsymbol{E}(1 + 4\pi\chi)\boldsymbol{P} = \varepsilon\boldsymbol{E} \qquad (4$$

where ε is *the dielectric permittivity*. It is also called the dielectric constant, because it is independent of the field strength. It is, however, dependent on the frequency of the applied field, the temperature, the density (or the pressure), and the chemical composition of the system.

1. Types of Polarization

For isotropic systems and static linear electric fields, we have

$$\boldsymbol{P} = \frac{\varepsilon - 1}{4\pi}\boldsymbol{E} \qquad (5)$$

The applied electric field gives rise to a dipole density through the following mechanisms:

Deformation polarization — This can be further divided into two independent types:

Electron polarization — the displacement of nuclei and electrons in the atom under the influence of the external electric field. As electrons are very light they have a rapid response to the field changes; they may even follow the field at optical frequencies.

Atomic polarization — the displacement of atoms or groups of atoms in the molecule under the influence of the external electric field.

Orientation polarization — The electric field tends to direct the permanent dipoles. The rotation is counteracted by the thermal motion of the molecules. Therefore, the orientation polarization is strongly dependent on the temperature and the frequency of the applied electric field.

Ionic polarization — In an ionic lattice, the positive ions are displaced in the direction of an applied field while the negative ions are displaced in the opposite direction, giving a resultant dipole moment to the whole body. The mobility of ions also strongly depends on the temperature, but contrary to the orientation polarization the ionic polarization demonstrates only a weak temperature dependence and is determined mostly by the nature of the interface where the ions can accumulate. Most of the cooperative processes in heterogeneous systems are connected with ionic polarization.

To investigate the dependence of the polarization on molecular quantities it is convenient to assume the polarization P to be divided into two parts: the induced polarization P_α, caused by translation effects, and the dipole polarization P_μ, caused by orientation of the permanent dipoles.

$$\frac{\varepsilon - 1}{4\pi}\boldsymbol{E} = \boldsymbol{P}_\alpha + \boldsymbol{P}_\mu \qquad (6)$$

We can now define two major groups of dielectrics: polar and nonpolar. A *polar dielectric* is one in which the individual molecules possess a dipole moment even in the absence of any applied field, i.e., the center of positive charge is displaced from the center of negative charge. A *nonpolar dielectric* is one where the molecules possess no dipole moment, unless they are subjected to an electric field. The mixture of these two types if dielectrics is common in the case of complex liquids and the most interesting dielectric processes are going on at their phase borders or at liquid-liquid interfaces.

Owing to the long range of the dipolar forces an accurate calculation of the interaction of a particular dipole with all other dipoles of a specimen would be very complicated. However, a good approximation can be made by considering that the dipoles beyond a certain distance, say some radius *a*, can be replaced by a continuous medium having the macroscopic dielectric properties of the specimen. Thus, the dipole whose interaction with the rest of the specimen is calculated may be considered as surrounded by a sphere of radius *a* containing a discrete number of dipoles, beyond which there is a continuous medium. To make this a good approximation the dielectric properties of the whole region within the sphere should be equal to those of a macroscopic specimen, i.e., it should contain a sufficient number of molecules to make fluctuations very small (3, 4). This approach can be successfully used for the calculation of dielectric properties of ionic self-assembled liquids. In this case the system can be considered to be a monodispersed system consisting of spherical water droplets dispersed in the nonpolar medium (5).

Inside the sphere where the interactions take place, the use of statistical mechanics is required. This is a second method for calculating the polarization from molecular parameters that allows us to take into account the short range of dipole-dipole interaction (1, 2). Here, we may write for the dipole density ***P*** of a homogeneous system:

$$\boldsymbol{P}V = \langle \boldsymbol{M} \rangle \qquad (7)$$

where V is the volume of the dielectric under consid eration and ⟨M⟩ is its average total dipole moment and ⟨ ⟩ denote a statistical mechanical average. For an iso-tropic system, using Eq. (4), we find:

$$(\varepsilon - 1)\boldsymbol{E} = \frac{4\pi}{V}\langle \boldsymbol{M} \rangle \tag{8}$$

Further calculations, using all necessary statistical mechanical approaches for the appropriate border conditions, allow us to obtain the well-known Kirkwood-Frolich relationship for static dielectric per mittivity:

$$g\mu = \frac{9kT}{4\pi}\frac{(\varepsilon - \varepsilon_\infty)(2\varepsilon + \varepsilon_\infty)}{\varepsilon(\varepsilon_\infty + 2)^2} \tag{9}$$

where μ is the dipole moment of the molecule in the gas phase, k is the Boltzmann constant, T is the abso lute temperature, ε_∞ is the high-frequency limit of complex dielectric permittivity, and g is a correlation factor. Kirkwood introduced the correlation factor in his theory in order to take into account the short-range order interactions in associated polar liquids.

An approximate expression for the Kirkwood cor relation factor can be derived by taking into account only the nearest-neighbors' interactions. In this case the sphere is reduced to contain only the Jth molecule and its z nearest neighbors. For this definition it is possible to derive the following relationship for the parameter g:

$$g = 1 + z\langle \cos\theta_{ij} \rangle \tag{10}$$

where $\langle \cos\theta_{ij} \rangle$ gives the average angle of orientations between the ;th and y'th dipoles in the sphere of short-range interactions. From Eq. (10) it is obvious that when $\langle \cos\theta_{ij} \rangle \neq 0$, g will be different from 1. It means that the neighboring dipoles are correlated between themselves. The parallel orientation of dipoles leads to a positive value of the average cosines and *g* larger than 1. When the antiparallel orientation of dipoles can be observed, *g* will be smaller than 1. Both cases are observed experimentally (1, 2, 4). This parameter will be extremely useful in the understanding of the short-range molecular mobility and interaction in self-assembled systems.

B. Dielectric Polarization in Time-dependent Electric Fields

When an external field is applied the dielectric polar ization reaches its equilibrium value, not instantly, but over a period of time. By analogy, when the field is removed suddenly, the polarization decay caused by thermal motion follows the same law as the relaxation or decay function:

$$\alpha(t) = \frac{\boldsymbol{P}(t)}{\boldsymbol{P}(0)} \tag{11}$$

The relationship, E_q. (4), for the displacement vector in the case of time-dependent fields may be written as follows (1, 3):

$$\boldsymbol{D}(t) = \varepsilon_\infty \boldsymbol{E}(t) + \int_{-\infty}^{t} \boldsymbol{E}(t')\dot{\Phi}(t - t')\mathrm{d}t' \tag{12}$$

where $\boldsymbol{D}(t) = \boldsymbol{E}(t) + 4\pi\boldsymbol{P}(t)$, ε_∞ is the high-frequency limit of the complex dielectric permittivity $\varepsilon^*(w)$, and Φ (t) is the dielectric response function (Φ(t) - (ε_S=ε_∞) [1= α(t)] where α(t) is the relaxation function or the decay function of dielectric polarization). (ε_S is the low-frequency limit of the permittivity, commonly denoted the static permittivity.) The point denotes the time derivative in Eq. (12). The complex dielectric permit tivity $\varepsilon_*(\omega)$ is connected with the relaxation function by a very simple relationship:

$$\frac{\varepsilon^*(\omega) - \varepsilon_\infty}{\varepsilon_s - \varepsilon_\infty} = L\{-\dot{\alpha}(t)\} \tag{13}$$

where L is the operator of the Laplace transform, which is denned for the arbitrary time-dependent functionf(t) as:

$$L\{f(t)\} \equiv F(\omega) = \int_0^\infty \mathrm{e}^{-s} f(t)\mathrm{d}t, \qquad s = i\omega + x, \text{ where } x \to 0 \tag{14}$$

If

$$\alpha(t) \sim \exp(-t/\tau_m) \tag{15}$$

where τ_m repi-esents the dielectric relaxation time, then the relation first obtained by Debye, is true for the frequency domain (1, 3, 4):

$$\frac{\varepsilon^*(\omega) - \varepsilon_\infty}{\varepsilon_s - \varepsilon_\infty} = \frac{1}{1 + i\omega\tau_m} \tag{16}$$

For most of the systems being studied such a rela tion does not sufficiently describe the experimental results. This makes it necessary to use empirical rela tions which formally take into account the distribution of relaxation times with the help of various parameters (α,β) (3). In the most general way such nonDebye dielectric behavior can be described by the so called Havriliak-Negami relationship (3, 4, 6):

$$\varepsilon(\omega) = \varepsilon_\infty + \frac{\varepsilon_s - \varepsilon_\infty}{[1 + (i\omega\tau)^\alpha]^\beta}, \qquad \alpha, \beta > 0 \tag{17}$$

The specific case $\alpha=1$, $\beta=1$ gives the Debye relaxa tion law, $\beta=1$, $\alpha\neq 1$ corresponds to the so-called Cole-Cole equation, whereas the case $\alpha=1$, $\beta\neq 1$ corresponds to the Cole-Davidson formula. Recently, some progress in the understanding of the physical meaning of the empirical parameters (α, β) has been made (7, 8). Using the conception of a self-similar relaxation process it is possible to understand thenature of a nonexponential relaxation of the Cole-Cole, Cole-Davidson, or Havriliak-Negami type.

An alternative approach is to obtain information on the dynamic molecular properties of a substance directly in the time domain. Relation E_q. (13) shows that the equivalent information on the dielectric relaxation properties of a sample being tested can be obtained both in the frequency and the time domains. Indeed, the polarization fluctuations caused by thermal motion in the linear response case are the same as for the macroscopic reconstruction induced by the electric field (9, 10). This means that one can equate the relaxa tion function $\alpha(t)$ and the macroscopic dipole correlation function $\Gamma(t)$:

$$\alpha(t) \cong \Gamma(t) = \frac{\langle \boldsymbol{M}(0)\boldsymbol{M}(t)\rangle}{\langle \boldsymbol{M}(0)\boldsymbol{M}(0)\rangle} \tag{18}$$

where M(t) is the macroscopic fluctuating dipole moment of the sample volume unit which is equal to the vector sum of all the molecular dipoles. The rate and laws govering the decay function $\Gamma(t)$ are directly related to the structural and kinetic properties of the sample and characterize the macroscopic properties of the system studied. Thus, the experimental function $\Phi f(t)$ and hence$\alpha(t)$ or $\Gamma(t)$ can be used to obtain infor mation on the dynamic properties of a dielectric in terms of the dipole correlation function.

C. Dielectric Polarization in Heterogeneous Systems

Complex fluids composed of several pseudophases with a liquid-liquid interface (emulsions, macroemul-sions, cells, liposomes) or liquid-solid interface (suspensions of silica, carbon black, latex, etc.) can, from a dielectric point of view, be considered as classical heterogeneous systems. Several basic theoretical approaches have been developed in order to describe the dielectric behavior of such systems. Depending on the concentration, the shape of the dispersed phase, and the conductivity of both the media and disperse phase, different mixture formulas can be applied to describe the electric property of the complex liquids (11-15).

Two general theoretical approaches have been applied in the analysis of heterogeneous materials. The macroscopic approach, in terms of classical electrodynamics, and the statistical mechanics approach, in terms of charge-density calculations. The first is based on the application of the Laplace equation to calculate the electric potential inside and outside a dispersed spherical particle (11, 12). The same result can be obtained by considering the relationship between the electric displacement D and the macroscopic electric field Ein a disperse system (12, 13). The second approach takes into account the coordinate-dependent concentration of counterions in the diffuse double layer, regarding the self-consistent electrostatic poten tial of counterions via Poisson's equation (5, 16, 17). Let us consider these approaches briefly.

The first original derivation of mixture formula for spherical particles was performed by Maxwell (18) and was later extended by Wagner (19). This Maxwell-Wagner (MW) theory of interfacial polarization usually can be successfully applied only for dilute dis persions of spherical particles. The dielectric permittiv ity of such a mixture can be expressed by the well-known relationship:

$$\varepsilon = \varepsilon_1 \frac{(2\varepsilon_1+\varepsilon_2) - 2\phi(\varepsilon_1-\varepsilon_2)}{(2\varepsilon_1+\varepsilon_2) + \phi(\varepsilon_1-\varepsilon_2)}, (\phi \ll 1) \tag{19}$$

Here, $\varepsilon_1$and ε_2 are the dielectric permittivities of the continuous phase and inclusions, respectively, and ϕ is the volume fraction of inclusions.

Fricke and Curtis (20) and then Sillars (21) general ized the MW theory for the case of ellipsoidal particles. Bruggemann (22) and Hanai (23) in his series of papers extended the theory also for the case of concentrated disperse systems. For a system containing homoge neously distributed spherical particles Hanai found that the complex permittivity of the system is given by

$$\left(\frac{\varepsilon_2^* - \varepsilon^*}{\varepsilon_2^* - \varepsilon_1^*}\right)\left(\frac{\varepsilon_1^*}{\varepsilon^*}\right)^{1/3} = 1-\phi \tag{20}$$

Boned and Peyrelasse (24) and Boyle (25) made extensions of the MW theory to include nonspherical droplets and concentrated emulsions. In the case of disperse systems containing spheroidal particles aligned in parallel, the total permittivity according to Boyle may be found from (25):

$$\left(\frac{\varepsilon_2^* - \varepsilon^*}{\varepsilon_2^* - \varepsilon_1^*}\right)\left(\frac{\varepsilon_1^*}{\varepsilon^*}\right)^{A_a} = 1-\phi \tag{21}$$

where A_a is a depolarization factor dependent on the axial ratio a/b describing the spheroids. When A_a= 1/3, Eq. (21) is reduced to Eq. (20).

In3 the cases where spheroidal particles are randomly oriented, the Boned-Peyrelasse equation may be applied (24):

$$\left(\frac{\varepsilon_1^*}{\varepsilon^*}\right)^{3d}\left(\frac{\varepsilon_2^*-\varepsilon^*}{\varepsilon_2^*-\varepsilon_1^*}\right)\left(\frac{\varepsilon_1^*(1+3A)+\varepsilon_2^*(2-3A)}{\varepsilon^*(1+3A)+\varepsilon_2^*(2-3A)}\right)^{3K} = 1-\phi \tag{22}$$

Here, $A = (1\text{-}A_a)/2$ is the depolarization factor while d and K are functions of A. Also in this case, when all three axis are equal, i.e., the particles are spherical, A = 1/3 and Eq. (22) simplifies to Eq. (20).

The main assumption in all these approaches is that the characteristic sizes of the single-phase regions are much larger than the Debye screening length (26). Provided that the dielectric permittivity and electric conductivity of the individual phases are known, the MW models enable us to calculate the total frequency-dependent permittivity of the system.

An essential feature of the MW polarization effect in complex liquids with liquid-liquid interfaces is the appearance of an accumulated charge at the bound aries between differing dielectric media as a result of ionic migration processes (12, 13). It is further assumed in the MW theory that the conductivities of each phase are uniform and constant. However, the presence of spatial charges in the suspending medium alters the potential gradient near the interface. Thermal motions and ion concentration effects result in this surface-charge layer. In emulsion systems, where the water droplet also contains counterions, a considerable part of the dielectric response to an applied field originates from the redistribution of counterions (27). It is known (12, 28-31) that counterions near the charged surface can be distributed into two regions: the Stern layer and the Gouy-Chapman diffuse double layer. Counterions in the Stern layer are considered fixed on the inner surface of the droplet and are unable to exchange posi tion with the ion in the bulk. The distribution of coun terions in the diffuse double layer is given by the Boltzmann distribution in terms of the electrostatic potential. This potential is given, self-consistently, in terms of these counterion charges by Poisson's equation instead of Laplace's equation just as it was performed in the models of interfacial polarization.

The distribution of counterions is essentially deter mined by their concentration and the geometry of the water core. Thus, in the case of large droplets, the assumption can be made that the droplet radius is much larger than the length of the diffuse double layer as measured by the Debye screening length. In such an approximation, the counterions can be consid ered to form a thin layer near the inner surface of the droplet. The difference between the Stern layer and the diffuse double layer peters out and the polarization can be described by the Schwarz model (32). In the Schwarz model the mechanism controlling the relaxa tion is the diffusion of the counterions along the sur face. This model is more relevant to the dielectric behavior of macroemulsions than to microemulsions, for example. The above approach (unlike the "classi cal" MW) institutes the dependence of the dielectric properties on the characteristic size of mesoscale struc tures (e.g., on the radius of dispersed particle), and the ionic strength or dissociation ability of substances.

III. BASIC PRINCIPLES OF DIELECTRIC SPECTROSCOPY

The dielectric spectroscopy (DS) method occupies a special place among the numerous modern methods used for physical and chemical analysis of material, because it allows investigation of dielectric relaxation processes in an extremely wide range of characteristic times (10^4-10^{-12} s). Although the method does not possess the selectivity of NMR or ESR it offers impor tant and sometimes unique information on the dynamic and structural properties of substances. DS is especially sensitive to intermolecular interactions, and cooperative processes may be monitored. It pro vides a link between the properties of the individual constituents of a complex material and the character ization of its bulk properties (see Fig. 1).

However, despite its long history of development, this method is not widespread for comprehensive use, because the wide frequency range (10^{-5}-10^{12} Hz), overlapped by discrete frequency domain methods, have required a great deal of complex and expensive equipment. Also, for different reasons, not all the ranges have been equally available for measurement. Investigations of samples with variable properties over time (e.g., nonstable emulsions or biological systems) have thus been difficult to conduct. The low-frequency measurements of conductive systems had a strong lim itation due to electrode polarization. All the above-mentioned reasons led to the fact that information on dielectric characteristics of a substance could only be obtained over limited frequency ranges. As a result the investigator had only part of the dielectric spectrum at his/her disposal to

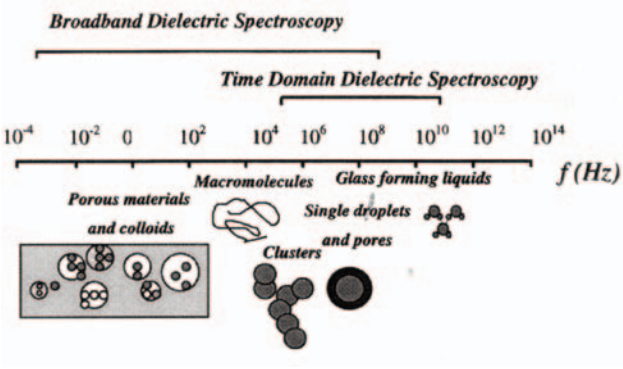

Figure 1 Electromagnetic wave scale of DS applicability for complex materals.

determine the relaxation parameters.

The successful development of the time-domain dielectric spectroscopy method (generally called time-domain spectroscopy - TDS) (33-38) and of broad band dielectric spectroscopy (BDS) (39-41) have radi cally changed attitudes toward DS, making it an effective tool for the investigation of solids and liquids, on the macroscopic, microscopic, and mesoscopic levels.

The basic approaches, the principles of experimental realization, sample holders for different applications, data treatment and presentation, and different TDS methods, which enable one to obtain the complete spectrum of $\varepsilon^*(\omega)$ in the frequency range 10^5-10^{10} Hz, are given below.

A. Basic Principles of the TDS Method

TDS is based on transmission-line theory in the time domain that aids in the study of heterogeneities in coaxial lines according to the change in shape of a test signal (33-38). As long as the line is homogeneous the shape of this pulse will not change. However, in the case of a heterogeneity in the line (the inserted dielectric, for example) the signal is partly reflected from the air-dielectric interface and partly passes through it. Dielectric measurements are made along a coaxial transmission line with the sample mounted in a cell that terminates the line. A simplified block diagram of the set-up common for most TDS methods (except transmission techniques) is presented in Fig. 2. Differences mainly include the construction of the measuring cell and its position in the coaxial line. These lead to different kinds of expressions for the values that are registered during the measurement and for the dielectric characteristics of the objects under study.

A rapidly increasing voltage step $V_0(t)$ is applied to the line and recorded, along with the reflected voltage R(t) returned from the sample and delayed by the cable propagation time (Fig. 2). Any cable or instrument artifacts are separated from the sample response as a result of the propagation delay, thus making them easy to identify and control. The entire frequency spectrum is captured at once, thus eliminating drift and distor tion between frequencies.

The complex permittivity is obtained as follows: for nondisperse materials (frequency-independent permit tivity), the reflected signal follows the RC exponential response of the line-cell arrangement; for disperse materials, the signal follows a convolution of the line-cell response with the frequency response of the sample. The actual sample response is found by writing the total voltage across the sample:

$$V(t) = V_0(t) + R(t) \tag{23}$$

and the total current through the sample (38, 42, 44):

$$I(t) = \frac{1}{Z_0}[V_0(t) - R(t)] \tag{24}$$

where the sign change indicates direction and Z_0 is the characteristic line impedance. The total current through a conducting dielectric is composed of the displacement current $I_D(t)$, and the low-frequency current between the capacitor electrodes $I_R(t)$- Since the active resistance at zero frequency of the sample-containing cell is (38) (see Fig. 3):

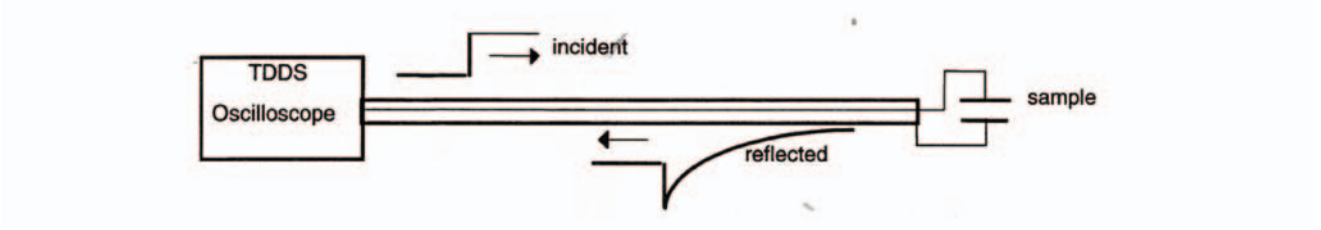

Figure 2 Basic TDS set-up.

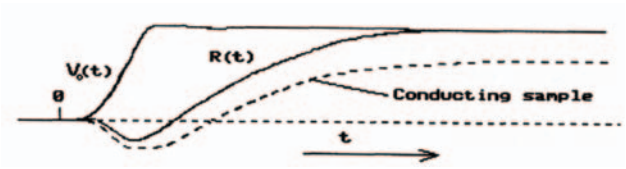

Figure 3 Characteristic shape of the signal recorded during a TDS experiment; $V_0(f)$: incident pulse, $R(t)$: reflected signal.

$$r = \lim_{t\to\infty} \frac{V(t)}{I(t)} = Z_0 \lim_{t\to\infty} \frac{V_0(t) + R(t)}{V_0(t) - R(t)} \tag{25}$$

the low-frequency current can be expressed as:

$$I_R(t) = \frac{V(t)}{r} = \frac{V_0(t) + R(t)}{Z_0} \lim_{t\to\infty} \frac{V_0(t) - R(t)}{V_0(t) + R(t)} \tag{26}$$

Thus, Eq. 24 can be written as:

$$I_D(t) = \frac{1}{Z_0}\left\{[V_0(t) = R(t)] - [V_0(t) + R(t)] \lim_{t\to\infty} \frac{V_0(t) - R(t)}{V_0(t) + R(t)}\right\} \tag{27}$$

Relations (23) and (27) represent the basic equations that relate $I(t)$ and $V(f)$ to the signals recorded during the experiment. In addition, Eq. (27) shows that TDS permits one to determine the low-frequency conductivity a of the sample directly in the time domain (36—38):

$$\sigma = \frac{\varepsilon_0}{Z_0 C_0} \lim_{t\to\infty} \frac{V_0(t) - R(t)}{V_0(t) + R(t)} \tag{28}$$

where $\varepsilon_0 = 8.85 \times 10^{-12}$ F/m, and C_0 is the electric capacity of the coaxial sample cell terminated to the coaxial line. Using $I(t)$ and $V(t)$ or their complex Laplace transforms $i(\omega)$) and $\upsilon(\omega)$ one can deduce the relations that will describe the dielectric characteristics of a sample being tested either in frequency or time domain. The final form of these relations depends on the geometric configuration of the sample cell and its equivalent presentation (33—38).

The sample admittance for the sample cell terminated to the coaxial line is then given by

$$Y(\omega) = \frac{i(\omega)}{v(\omega)} \tag{29}$$

and the sample permittivity can be presented as follows:

$$\varepsilon(\omega) = \frac{Y(\omega)}{i\omega C_0} \tag{30}$$

where C_0 is the geometric capacitance of the empty sample cell. To minimize line artifacts and establish a common time reference, Eq. (29) is usually rewritten in differential form, to compare reflected signals from the sample and a calibrated reference standard and thus eliminate $V_0(t)$ (33—38).

If one takes into account the definite physical length of the sample and multiple reflections from the air-dielectric or dielectric-air interfaces, Eq. (30) must be written in the following form (33—36, 44):

$$\varepsilon^*(\omega) = \frac{c}{i\omega(\gamma d)} Y(\omega) X \cot X \tag{31}$$

where $X = (\omega d/c)\sqrt{\varepsilon^*(\omega)}$, d is the effective length of the inner conductor, c is the velocity of light, and γ is the ratio between the capacitance per unit length of the cell and that of the matched coaxial cable. Equation (31), in contrast to Eq. (30), is a transcendental one, and its exact solution can be only obtained numerically (33—37, 42). The essential advantage of TDS methods in comparison with frequency methods is the ability to obtain the relaxation characteristics of a sample directly in the time domain. Solving the integral equation one can evaluate the results in terms of the dielectric response function $\Phi(t)$ (38, 43, 44). It is then possible to associate $\varphi(t) = \Phi(t) + \varepsilon_\infty$ with the macroscopic dipole correlation function $\Gamma(t)$ (9, 46) in the framework of linear-response theory.

B. Experimental Tools

1. Hardware

The standard time-domain reflectometers used to measure the inhomogeneities of coaxial lines (38, 42, 47, 48) are the basis of the majority of modern TDS setups. The reflectometer consists of a high-speed voltage step generator and a wide-band registering system with a single- or double-channel sampling head. In order to meet the high requirements of TDS measurements such commercial equipment must be considerably improved. The main problem is due to the fact that the registration of incident $V(f)$ and reflected $R(f)$ signals is accomplished by several measurements. In order to enhance the signal-to-noise ratio one must accumulate all the registered signals. The high level of drift and instabilities during generation of the signal and its detection in the sampler are usually inherent to serial reflectometry equipment.

The new generation of digital sampling oscilloscopes (36, 45) and specially designed time-domain measuring setups (TDMS) (38) offer comprehensive, high precision, and automatic measuring systems for TDS hardware support. They usually have a small jitter factor (< 1.5 ps), important for rise time, a small flatness of incident pulse (< 0.5% for all amplitudes), and in some systems a unique option for

parallel-time nonuniform sampling of the signal (38).

The typical TDS set-up consists of a signal recorder, a two-channel sampler, and a built-in pulse generator. The generator produces 200-mV pulses of 10 μs duration and short rise time (~ 30 ps). Two sampler channels are characterized by an 18 GHz bandwidth and 1.5 mV noise (RMS). Both channels are triggered by one common sampling generator that provides their time correspondence during operation. The form of the voltage pulse thus measured is digitized and averaged by the digitizing block of TDMS. The time base is responsible for major metrology TDMS parameters. The block diagram of the described TDS set-up is presented in Fig. 4 (38).

a. Nonuniform Sampling

In highly disperse materials, as described in this review, the reflected signal *R(t)* extends over wide ranges in time and cannot be captured on a single time scale with adequate resolution and sampling time. In an important modification of regular TDS systems, a non-uniform sampling technique (parallel or series) has been developed (38, 49).

In the series realization, consecutive segments of the reflected signal on an increasing time scale are registered and linked into a combined time scale. The combined response is then transformed using a running Laplace transform to produce the broad frequency spectra (49).

In the parallel realization, a multiwindow time scale of sampling is created (38). The implemented time scale is the piecewise approximation of the logarithmic scale. It includes $nw \subseteq 16$ sites with the uniform discretization step determined by the following formula:

$$\delta_{nw} = \delta_1 \times 2^{nw} \tag{32}$$

where δ_1 = 5 ps is the discretization step at the first site, with the number of points in each step except for the first one being equal to $npw = 32$. At the first site, the number of points $npw_1 = 2npw$. The doubling of the number of points at the first site is necessary in order to have the formal zero-time position, which is impossible in the case of the strictly logarithmic structure of the scale. In addition, a certain number of points located in front of the zero-time position is added. They serve exclusively for the visual estimation of the stability of the time position of a signal and are not used for the data processing.

The structure of the time scale described allows the overlapping of the time range from 5 ps to 10 μs during one measurement, which results in a limited number of registered readings. The overlapped range can be shortened, resulting in a decreasing number of registered points and thus reducing the time required for data recording and processing.

The major advantage of the multiwindow time scale is the ability to obtain more comprehensive information. The signals received by using such a scale contain information within a very wide time range and the user merely decides which portion of this information to use for further data processing. Also, this scale provides for the filtration of registered signals close to the optimal one already at the stage of recording.

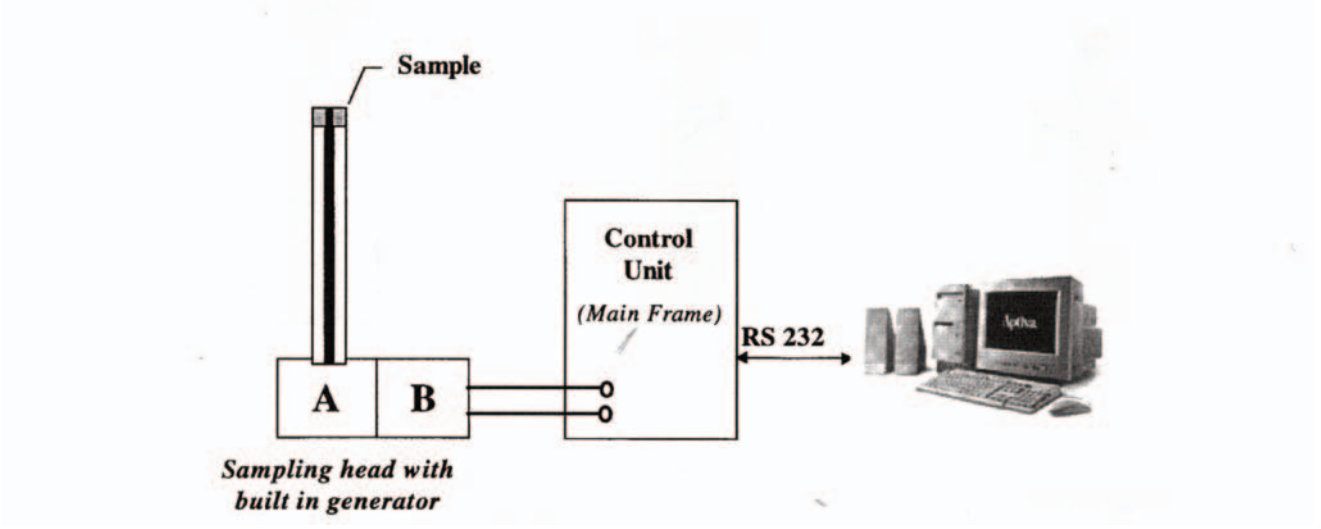

Figure 4 Circuit diagram of a TDS set-up.

b. Sample Holders

A universal sample holder that can be used for both liquid and solid samples in both the low- and high-frequency regions of the TDS method is unfortunately not yet available. The choice of its configuration depends on the measurement method and data-treatment procedure. In the framework of the lumped capacitor approximation one can consider three general types of sample holders (38, 44) (Fig. 5a): a cylindrical capacitor filled with sample. This cell (a cut-off cell) can also be regarded as a coaxial line segment with the sample having an effective *yd* length characterized in this case by the corresponding spread parameters. This makes it possible to use practically identical cells for various TDS and BDS method modification (50). For the total-reflection method the cut-off cell is the most frequent configuration (33-37, 42). The theoretical analysis of the cut-off sample cell (Fig. 5a) showed that a lumped-element representation enables the sample-cell properties to be accurately determined over a wide frequency range (50). Another type of sample holder that is frequently used is a plate capacitor terminated to the central electrode on the end of the coaxial line (Fig. 5b) (38, 44, 51, 52). The most popular now for different applications is an open-ended coaxial line sensor (Fig. 5c) (53—59). In lumped-capacitance approximation the configurations in Fig. 5a,b have high-frequency limitations, and for highly polar systems one must take into account the finite propagation velocity of the incident pulse or, in other words, the spread parameters of the cell (34-38). The choice of cell shape is determined to a great extent by the aggregate condition of the system studied. While cell (a) is convenient for measuring liquids (see Fig. 6a), configuration (b) is more suitable for the study of solid disks and films (Fig. 6b). Both cell types can be used to measure powder samples. While studying anisotropic systems (liquid crystals, for instance) the user may replace a coaxial line by a strip line or construct a cell with the configuration providing the measurements under various directions of the applied electric field (35, 36). The (c) type cell (see Fig. 5c) is used only when it is impossible to place the sample in the (a) or (b) type cells (38, 54—61). The fringing capacity of the coaxial-line end is the working capacity for such a cell. This kind of cell is widely used now for investigating the dielectric properties of biological materials and tissues (56—58), petroleum products (58), constructive materials (45), soil (60), and numerous other nondestructive permittivity and permeability measurements. The theory and calibration procedures for such

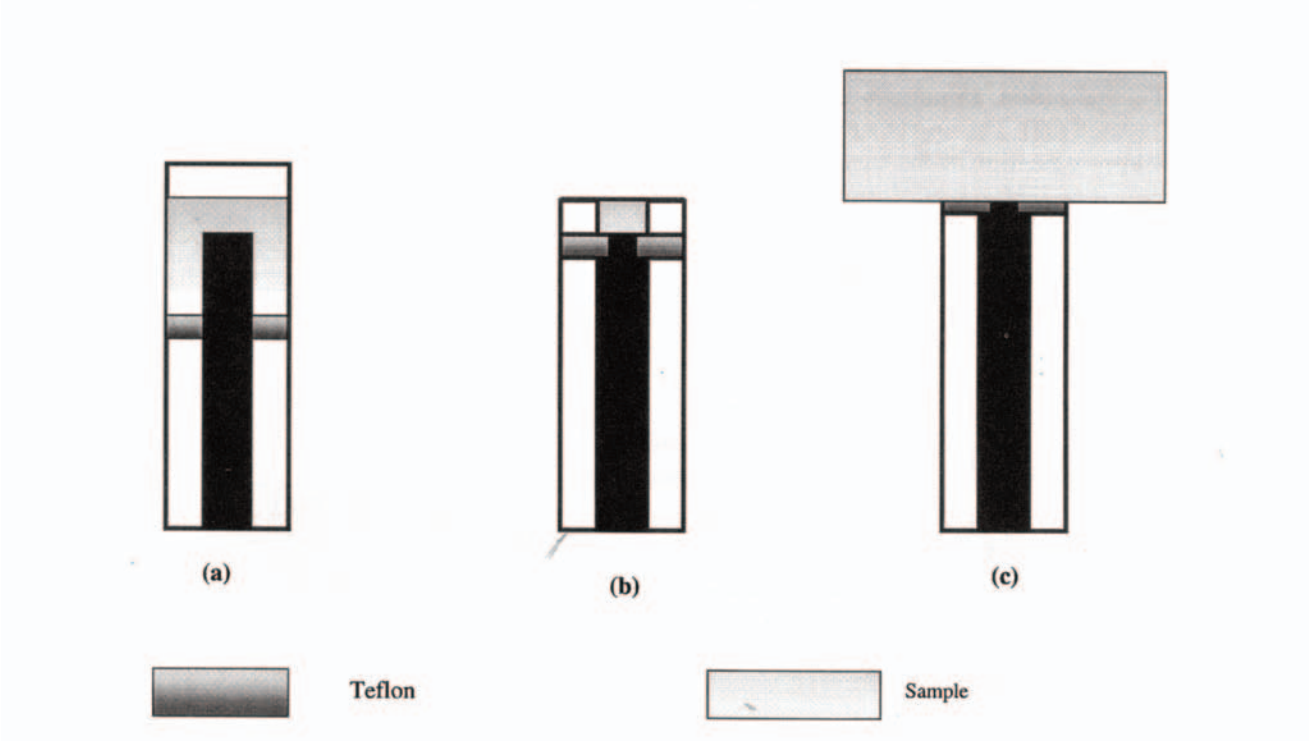

Figure 5 Simplified drawings of sample cells: (a) open coaxial line cell; (b) lumped capacitance cell; (c) end capacitance cell.

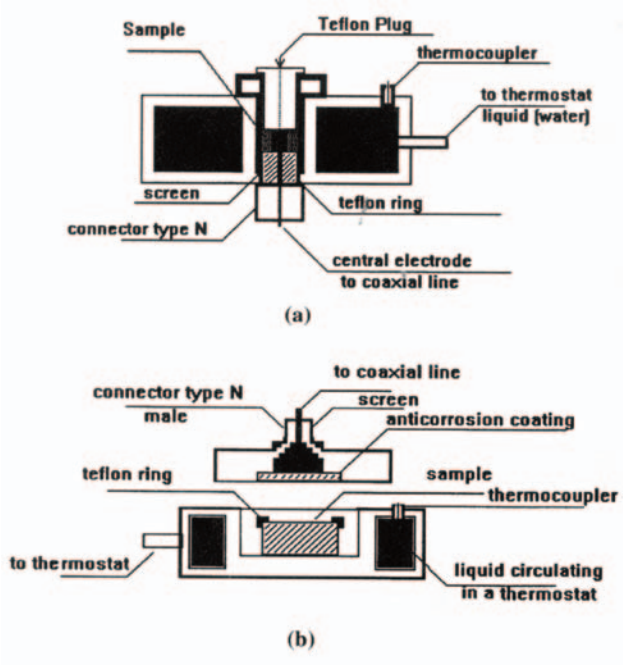

Figure 6 (a) Sample cell for high-frequency measurements of liquids; (b) sample cell for low-frequency measurements of liquids, solids, and powders. (From Ref. 38. With permission from American Institute of Physics.)

open-coaxial probes are well developed (61, 62) and the results are meeting the high standards of modern measuring systems.

2. Software

Measurement procedures, registration, storage, time referencing, and data analyses are carried out automatically in modern TDS systems. The process of operation is performed in on-line mode and the results can be presented both in frequency and time domains (34, 36, 38, 45, 49). There are several features of the modern software that control the process of measurement and calibration. One can define the time windows of interest that may be overlapped by one measurement. During the calibration procedure precise determination of the front-edge position is carried out and the setting of the internal autocenter on this position applies to all the following measurements. The precise determination and settings of horizontal and vertical positions of calibration signals are also carried out. All parameters may be saved in a configuration file, allowing for a complete set of measurements, using the same parameters and without additional calibration.

A typical flow chart of the data-processing software is presented in Fig. 7. It includes the options of signal corrections, correction of electrode polarization and d.c. conductivity, and different fitting procedures both in time and frequency domains.

C. Electrode Polarization Corrections

Many dielectric materials are conductive. This complicates the TDS study of conductive samples, and the effect of low-frequency conductivity needs to be corrected for. Usually, for a low-conductivity system the value of the d.c. conductivity can be evaluated as described in Sec. III.A.

One of the greatest obstacles in TDS measurements of conductive systems is the parasitic effect of electrode polarization. This accumulation of charge on electrode surfaces results in the formation of electric double layers (63—67). The associated capacitance and complex impedance due to this polarization is so large that the correction for it is one of the major requisites in obtaining meaningful measurements on conductive samples, especially in aqueous biological and colloidal systems (65—71). The details of electrode polarization depend microscopically upon the electrode surface topography and surface area, as well as upon the surface chemistry (reactive surface groups or atoms) and the interactions with the dielectric material or sample being examined. In the case of complex conductive liquids, the principal motivation of this work, surface ionization and ionexchange processes in the electric double layer, can depend critically upon the chemical nature of the sample being investigated as well as upon the chemical and physical nature of the electrodes used. Because these many effects can be so diverse, no simple correction technique has been widely accepted. Several equivalent circuits have been proposed for describing the essential elements of a sample cell containing electrolyte solution (15, 65, 68), and the most generally accepted approach is shown in Fig. 8. Under the assumption that the electrodes are blocking with respect to Faradaic electron transfer, the polarization impedance of the electrodes Z, may be expressed as

$$Z_p = R_p + \frac{1}{i\omega C_p} \tag{33}$$

where $i = \sqrt{-1}$. . Both C_p and R_p vary with frequency and Z_p is often considered negligible at sufficiently high frequencies. This high-frequency limit for electrode polarization has been estimated in different ways, depending on the

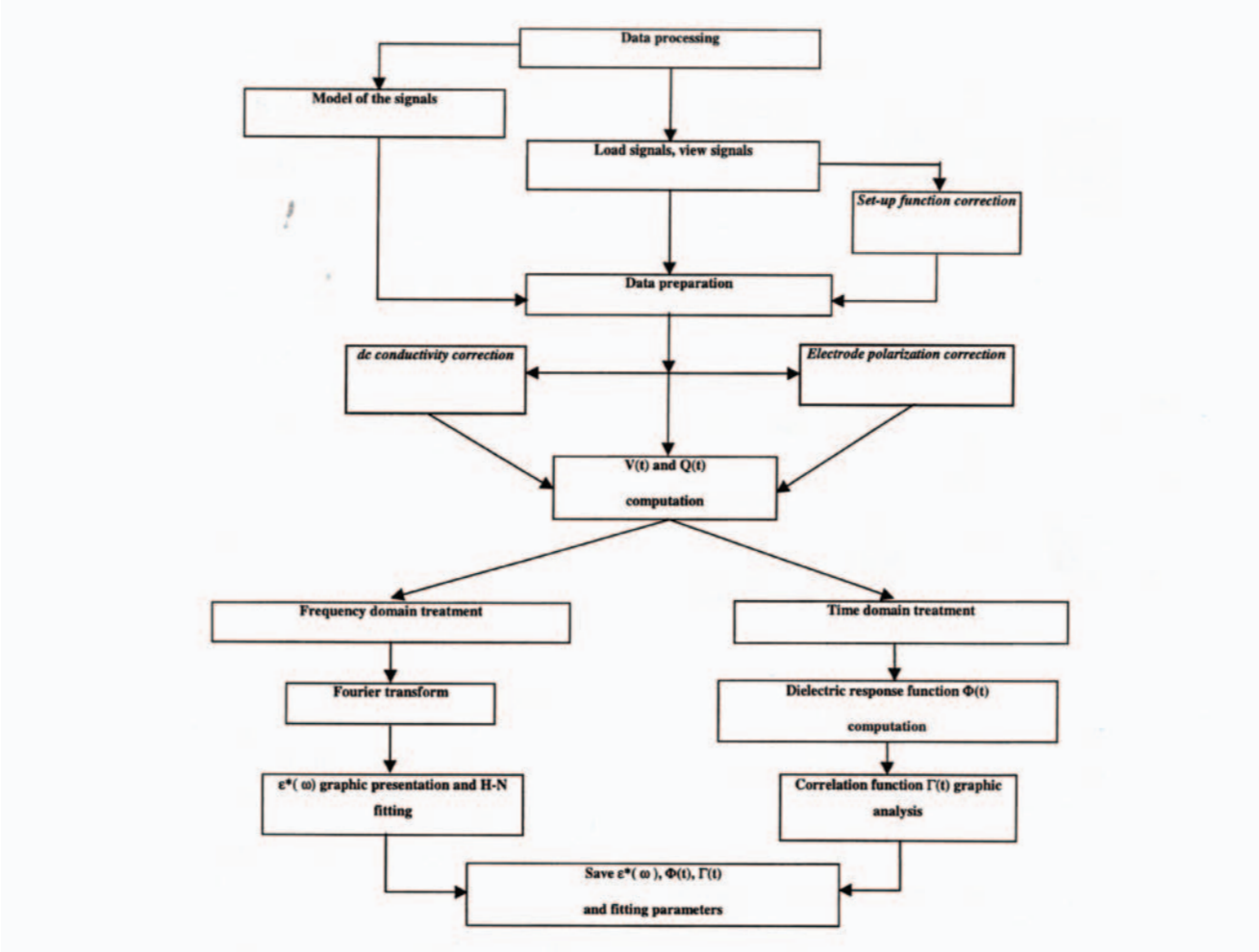

Figure 7 Flow chart of data-treatment software. (From Ref. 38. With permission from American Institute of Physics.)

particular type of electrode assembly and DS experiment, but has generally fallen in the interval 100-500 kHz. Owing to the diverse nature of the processes that can contribute to electrode polarization, such as sample-dependent chemical processes alluded to above, it is difficult to estimate an upper bound for this frequency limit.

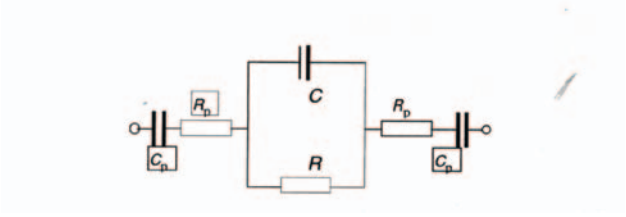

Figure 8 Equivalent circuits for a conductive dielectric sample with electrode polarization impedance described by C_p and R_p.

Two different approaches (71, 72) have been developed to correct for this phenomenon in TDS measurements directly in the time domain. One of them is applicable to weak electrolytes with a small level of low-frequency conductivity and hence a comparatively small effect of electrode polarization (72). In the other approach, applied to very conductive systems, the fractal nature of electrode polarization is considered (71). Let us consider these approaches.

In the case of TDS we can present a double layer with a capacitance C_p that is connected in series to the sample cell filled with the conductive material (Fig. 9). The characteristic charge time of C_p is much larger than the relaxation time of the measured sample. This allows us to estimate the parameters of parasitic capacitance in the long-time window where only the parasitic electrode polarization takes place. Considering the relationship for the current *i(s)*

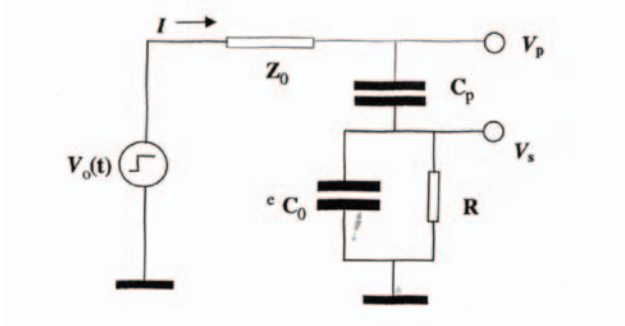

Figure 9 Equivalent circuit accounting for the electrode-polarization effect. $V_0(t)$ is a rapidly increasing voltage step; I(i) is a current; Z_0 is the coaxial line impedance; Cp is the capacitance of electrode polarization; C_o is an empty cell capacitance filled with a dielectric sample of permittivity ε and conductivity 1/R; $V_p(t)$ and $V_s(i)$ are the voltages at the appropriate parts of the circuit. (From Ref. 72. With permission from Elsevier Science B.V.)

($s = \gamma + i\omega$, $\gamma \longrightarrow 0$ is a generalized frequency in the Laplace transform) and voltage $\upsilon_p(s)$ in the frequency domain (Fig. 9) and making an inverse Laplace transform in the limit $t \longrightarrow \infty$, one can obtain the analytical expression for the electrode polarization correction function $V_{ec}(t)$ as follows (72):

$$V_{ec}(t) = \frac{2\tau_p}{\tau_R + \tau_p}(1 - e^{-t/\tau_2}) \tag{34}$$

where $\tau_p = Z_0C_p$, $\tau_R = RC_R$ and $\tau_0 = C_0R = C0/\sigma$. The parameter τ_2 may be obtained from the tail of the signal where only the electrode polarization effect takes place:

$$\tau_2 = \lim_{t\to\infty} \frac{2 - V_p(t)}{V_p(t)} \tag{35}$$

In order to eliminate the influence of the polarization capacitance it is necessary to subtract the exponential function with the appropriate parameters from the raw signal of the conductive sample. The exponential function $v_{ec}(t)$ of electrode polarization correction can easily be fitted to the real signal (see Fig. 10).

The TDS measurements on aqueous solutions of proteins and cell suspensions at up to several gigahertz (70-73) have shown that electrode polarization has to be taken into account even at frequencies as high as several hundred megahertz. Schwan noted the porous nature of electrode polarization phenomena (67). We nowadays often attribute such porosity to fractality and characterize porous tortuosity in terms of fractal dimension. Schwan also mentioned the increasing magnitude of this effect with increasing frequency.

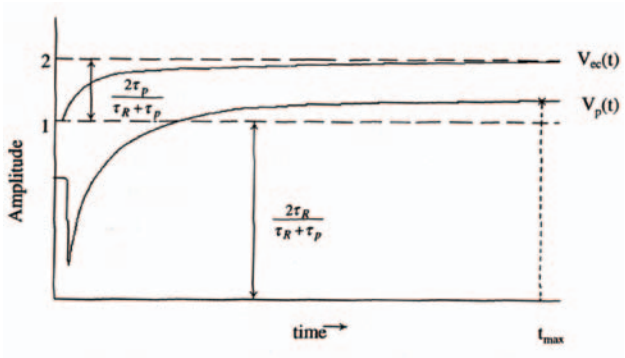

Figure 10 Schematic presentation of signal from a sample with conductivity [signal $V_p(t)$] and the correction exponential function described by the electrode polarization curve Vec(t). (From Ref. 72. With permission from Elsevier Science B.V.)

While the fractal nature of electrode surfaces is now well appreciated (74-79), no applications for making polarization corrections, capitalizing upon the fractal nature of electrode polarization, appear to have been developed previously.

A general form for depicting the fractal nature of an electrode double-layer impedance is given by

$$Z_v(j\omega) = A(v)(j\omega)^{-v} \tag{36}$$

where $0 < \upsilon < 1$, $A(\upsilon)$ is an adjustable paramter, and the frequency ω is located in a certain range $\omega_{min} \leq \omega \leq \omega_{max}$ due to the self-similar electrode-polarization properties of the electrode surface (74-78). At sufficiently high and low frequencies the self-similarity of the electrode polarization disappears.

The exponent v has often been connected with the fractal dimension of the electrode surface, but this connection is not necessary. Pajkossy and coworkers (76, 77) have shown, however, that specific adsorption effects in the double layer necessarily do appear for such a dispersion. We can connect the exponent to the fractality of the dynamical polarization and show that the polarization is self-similar in time, in contrast to the self-similar geometrical structure.

The specific frequency dependence in Eq. (36) is known as the constant phase angle (CPA) dependence (78-80). This impedance behavior occurs for a wide class of electrodes (75-77) and suggests the introduction of a new equivalent circuit element with impedance characteristics similar to those of Eq. (36). We call this element a recap element (derived from resistance and capacitance). The electric and fractal properties for this recap complex impedance $C_v(s)$ are given by:

$$C_v(s) = R(RC)^{-v}s^{-v} \qquad 0 < v < 1 \tag{37}$$

This circuit element occupies an intermediate position between $R_p(v = 0)$ and $C_p(v = 1)$ and expresses its impedance in the finite range of frequencies articulated above. Using the definition of Eq. (37) we can rearrange the equivalent circuit of the measuring sample cell filled with electrolyte solution, as shown in Fig. 11.

The impedance of the sample cell (electrodes) containing an electrolyte solution can then be derived using one of these recap elements for the impedance at each electrode. Since the electrodes in general are not perfectly identical, each can be defined according to Eq. (37) to give

$$C_{v_i}(s) \equiv C_{v_i} \cdot s^{-v_i} = R_i(R_iC_i)^{-v_i}s^{-v_i} \tag{38}$$

with i = 1 and 2. In this fractal representation the measuring cell is defined in terms of the fractal impedance of the electrode polarization.

In order to derive the current-voltage relationship obtained for the equivalent circuit of Fig. 10, it is convenient to note the following identity (81):

$$s^{-v}i(s) = \frac{1}{\Gamma(v)}\int_0^t (t-t')^{v-1}I(t')\mathrm{d}t' \tag{39}$$

where I(t) is a time-dependent current, $\Gamma(\upsilon)$ is the gamma function, s is a complex frequqency, and i(s) is the Laplace transformation of I(t). This resulting current-voltage relationship:

$$V(t) = \frac{C_{v_1}}{\Gamma(v_1)}\int_0^t (t-t')^{v_1-1}I(t')\mathrm{d}t' + \frac{C_{v_2}}{\Gamma(v_2)}\int_0^t (t-t')^{v_2-1}I(t')\mathrm{d}t' + \frac{1}{C}\int_0^t \exp[-(t-t')/\tau_c]I(t')\mathrm{d}t' \tag{40}$$

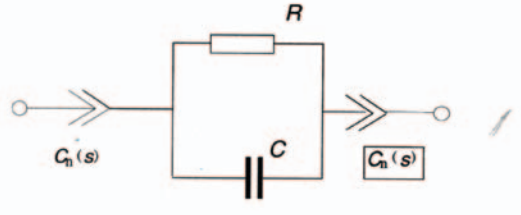

Figure 11 Equivalent circuits for a conductive dielectric sample with electrode-polarization impedance described by recap $C_v(s)$. (From Ref. 71. With permission from American Physical Society.)

has two terms describing the polarization of the respective electrodes and a third term describing the contribution from the bulk sample, where $\tau_c = RC$. Equation (40) shows how *V(t)* and *I(t)* are related for different kinds of measuring cells (i.e., different $C_{\upsilon i}$ υ_i) containing conductive solutions that polarize electrodes in conformity with the equivalent circuit illustrated in Fig. 11.

When I(t) is constant, as will be the case at long times after all the transients associated with sample relaxation have died out, Eq. (40) reduces to

$$V(t) \propto \frac{C_{v_1}}{v_1\Gamma(v_1)}t^{v_1} + \frac{Cv_2}{v_2\Gamma(v_2)}t^{v_2} + R[1-\exp(-t/\tau_c)] \tag{41}$$

where τ_c defines the time scale wherein the recap elements (the electrode polarization) affect the *V(t)* measured for the sample cell containing a conductive solution. If we make the simplifying assumptions that (1) both electrodes of the sample cell have the same (or equivalent) fractal polarization ($\upsilon_1 = \upsilon_2$; $C_{\upsilon 1} = C_{\upsilon 2}$); and (2) that there is no dispersion of the conductive solution (sample) in the time window defined by $\tau_c (> t_{mjn} = 1/\omega_{max})$, Eq. (41) can be rewritten in the following way:

$$V(t) = Bt^v + Rt/\tau_c \qquad \text{for } t/\tau_c \ll 1 \tag{42}$$

and

$$V(t) = Bt^v + R \qquad \text{for } t/\tau_c \gg 1 \tag{43}$$

Equations (41) and (42) are particularly useful in illustrating how the contribution of electrode polarization Bt^υ should be substracted from *V(t)*.

The voltage *V(t)* and the current I(t) observed at the sample cell [plate or cylindrical capacity (72, 73)] at the end of a coaxial line are presented by Eqs (23) and (24), respectively. In the case of conductive solutions, Eqs. (23) and (24) show that both the voltage and the current flow are influenced by electrode polarization. The observed voltage V(t) monotonically increases in the TDS time window of observation and the current I(t) monotonically decays. The electrode polarization correction is then obtained by subtracting the function Bt^υ from *V(t)*. The incident pulse $V_0(t)$ generally is an approximation to a step function with zero long-time slope, and the monotonically increasing behavior of V(t), associated with the correction Bt^υ, is a component of the reflected pulse R(t). Since this component is subtracted in Eq. (23) from R(t), it needs to be added ($+Bt^\upsilon/Z_0$) to I(t) in Eq. (24) and only after this can the correction of conductivity contribution by relation (27) be taken into account.

The experimental signal, *V(t)*, for a strong electrolyte solution of NaCl in water at 25°C (adjusted to pH 1.25 with 0.05 M HC1 and with a low-frequency conductivity of 1.57 S m^{-1}) is illustrated on a log-log scale in Fig. 12 (71). The TDS multiwindow measurement (38) allow a long-time (up to 10 us) registration of signal tails, where the signal from a dielectric with low-frequency conductivity has completely relaxed (decayed) and only the signal from the electrode polarization remains. The fractality index v was determined to be 0.785 with B = 0.593 by linear regression of the asymptotically linear portion. The fractality is strictly dependent on the electrode material (82), the electrode polishing (71), and the chemistry related to the interactions between aqueous electrolyte and the electrode surfaces.

The electrode polarization correction applicable for TDS measurements of conductive colloidal samples can be summarized in the following way. A refrence sample with an electrolyte composition and conductivity equal to the continuous phase is measured, and these data are subsequently used to fit the parameters v and B (as was illustrated above for the data in Fig. 12; then, as long as the conductivity and electrolyte composition of the continuous phase remain equal to that of the reference, the sample may be measured with the same electrodes. The polarization correction embodied in the v and B obtained earlier is applied by substraction of Bt^v from *V(t)* and by adding this same function (scaled by Z_0) to I(t). These corrected signals are then Fourier transformed (71) to obtain the resulting dielectric spectra, ε'(ω) and ε"(ω). In this exposition of the correction procedure we have illustrated the method, focusing upon the polarization properties of a simple two-component electrolyte solution. After correction in this case we are left with the properties of the neat solvent, water.

A comparison between the dielectric spectra of a simple electrolyte solution (pH = 1.25) with and without electrode polarization correction is presented in Fig. 13. The permittivity before and after the correction is illustrated in Fig. 13a. The uncorrected permittivity exhibits an anomalously large value at low frequencies and seemingly undergoes

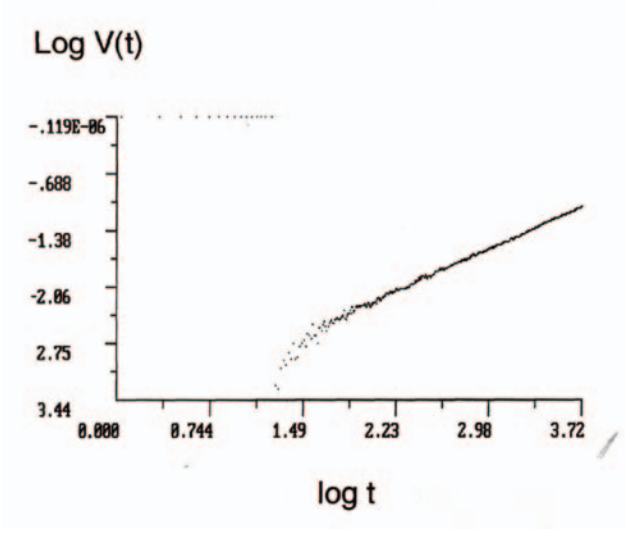

Figure 12 Voltage V(t) applied to the electrolyte solution; v = 0.785, V = 0.593 (with polished stainless-steel electrodes). (From Ref. 71. With permission from American Physical Society.)

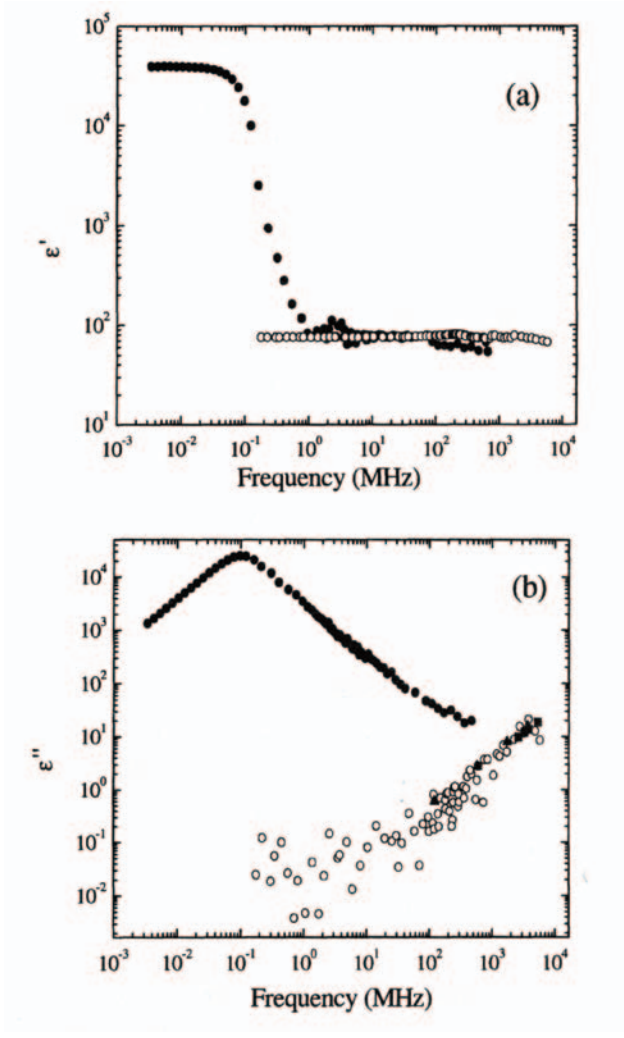

Figure 13 Fractal electrode-polarization correction for dielectric spectrum (a) ε' and (b) ε" of simple electrolyte solution; 0.1 M NaCl at pH 1.25; ● - uncorrected; ○ - corrected; ▲ - pure water at 20°C (from Ref. 83); ■ - pure water at 25°C. (From Ref. 84.)

some sort of dispersion process in the 100 kHz to 1 MHz region. This dispersion is highlighted as a peak (at 100 kHz) in the uncorrected dielectric loss spectrum of Fig. 13b. This dispersion essentially completely vanishes after the correction for electrode polarization has been made. The corrected permittivity in Fig. 13a is essentially independent of frequency at about 78. The dielectric loss, after correction for electrode polarization, becomes very small in the 100 kHz-100 MHz range, but shows a steady increase with increasing frequency. This increase is consistent with the well-known dielectric loss maximum of water in the region of 3 to 6 GHz, and compares well with the experimental dielectric loss values for water reported at 20°C (83) and at 25°C (84), and illustrated in Fig. 13b for comparison.

The data derived after the electrode polarization correction are in good agreement with previously published data on water. These data show unequivocally the need for electrode polarization correction at frequencies in excess of 100 MHz, and that such correction can be effected by explicitly considering the fractality of electrode polarization.

D. External Fields

The dielectric properties of a sample may be strongly influenced by its environment, and measurements of the dielectric behavior as a function of, for instance, temperature or pressure (2) are performed on a routine basis. In addition to the temperature and pressure effects, the TDS method also allows for subjecting the samples to externally applied electric or magnetic fields.

1. Electric (High-voltage Measurements)

High electric fields have been used in order to study the effect on W/O emulsions (52). In investigations on liquid crystals, external electric fields are applied in order to ensure the desired orientation of the crystals (85).

The TDS sampling heads are very vulnerable towards high voltages and electric currents. Thus, the signal applied to a sample and consequently recorded by the TDS equipment normally cannot exceed 0.2 V. In order to attain sufficiently high voltages between the electrodes to induce any changes in the sample and, at the same time and through the same line, transmit the low-voltage step pulse used in the characterization of the sample, special equipment has to be used. Thus, a broadband coaxial bias-tee is inserted into the transmission line. The bias-tee is designed so that it will let the fast rise-time pulses pass through with negligible distortion of the waveform, while the high-voltage d.c. is effectively blocked from reaching the part of the transmission line that is connected to the sampling head.

The modifications of the standard experimental setup needed to include this method are schematically depicted in Fig. 14. A d.c. voltage supply is connected to the coaxial line via a bias-tee (Picosecond Pulse Labs, 5530A), as described above. In this way a potential difference can be applied between the cell electrodes. Owing to the short distance between the electrodes (controlled by the spacer, see Fig. 15) strong electric field result, even from moderate voltages. With a spacer thickness of 120 μm and a potential difference of 60 V, the electric field applied to the sample will be 5 kV/cm. This field strength is sufficiently strong to lead to a marked distortion of the shape of water droplets in an emulsion, and in many cases the electric field induces the coalescence of emulsion droplets. A d.c. block inserted in the line between the bias-tee and the sampling head may be applied as an additional protection of the sampling head from the high voltage; only the step pulse is allowed to travel through. The blocking of a.c. fields is more difficult to accomplish; thus, at present, this method is limited to external d.c. fields.

2. Magnetic Fields

The orientation of a sample (on a molecular or aggregate level) by the action of a magnetic field may be achieved, using a set-up as illustrated in Fig. 16 (86). The dielectric cell shown in Fig. 16a is of the open-ended coaxial sensor type, and the electrical length is found to be 0.027 mm. The magnetic field is created using rod magnets with the magnetic poles placed on either side of the dielectric cell. An alternative set-up used for measuring the sedimentation profile of suspensions containing magnetic particles is shown in Fig. 16b. In this case a magnetic field up to approximately 0.4 T is created by an electromagnet. Also, the dielectric cell is modified in order to increase the functionality of the experimental set-up (Fig. 16b).

IV. DIELECTRIC PROPERTIES OF MICROEMULSIONS

Microemulsions are thermodynamically stable, clear fluids, composed of oil, water, surfactant, and sometimes cosurfactant, that have been widely investigated during recent years because of their numerous practical applications. The chemical structure of surfactants may be of low molecular weight as well as being polymeric, with nonionic or ionic components (87-90). In the case of an oil-continuous (W/O)

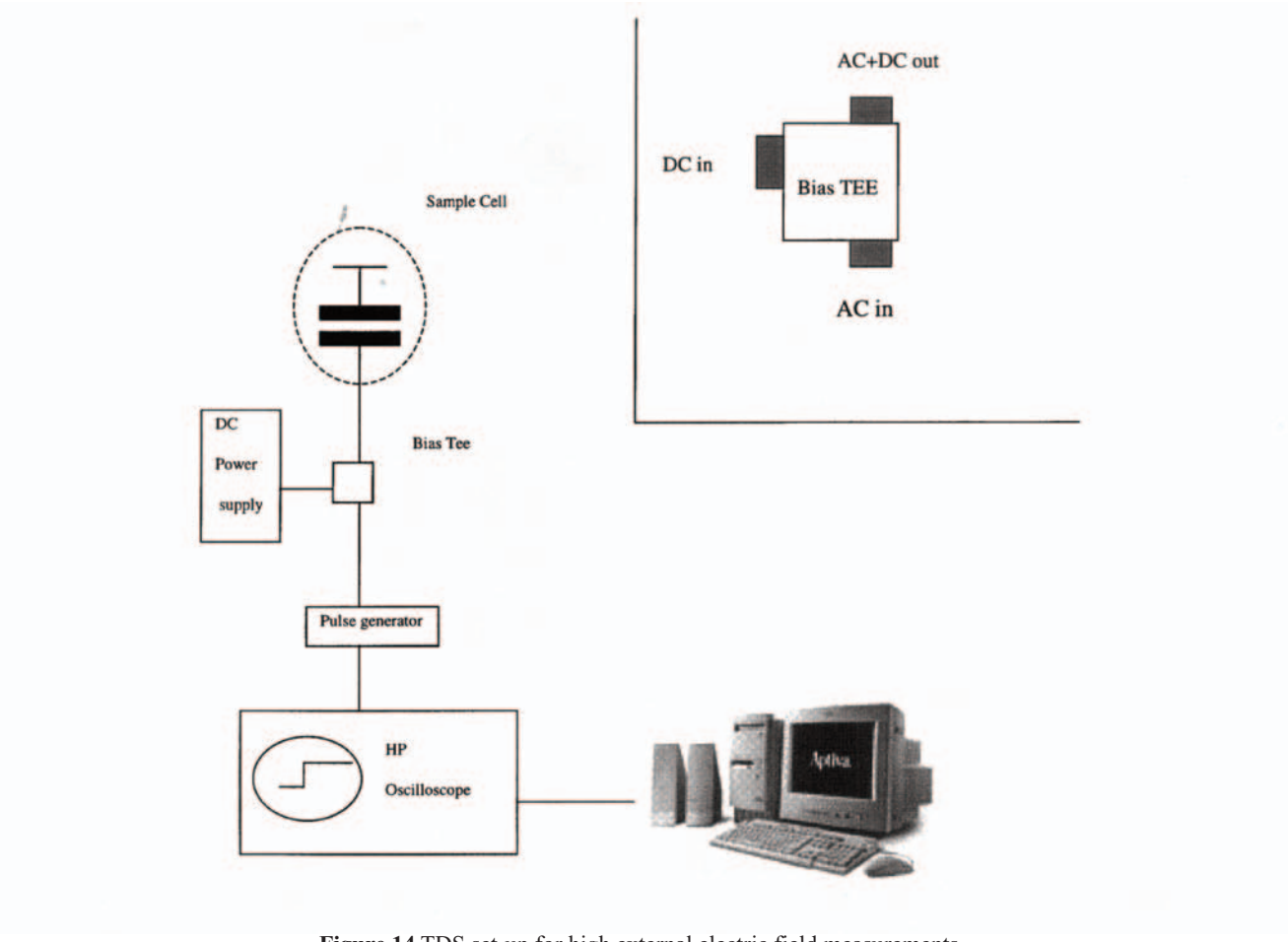

Figure 14 TDS set-up for high external electric field measurements.

microemulsion, at low concentration of the dispersed phase, the structure is that of spherical water droplets surrounded by a monomolecular layer of surfactant molecules whose hydrophobic tails are oriented towards the continuous oil-phase. When the volume fractions of oil and water are both high and comparable, random, bicontinuous structures are expected to form. There are also micro-emulsions in which the minor component forms disks, sheets, or rods, as well as mixtures, which are micro-lamellar (89-92). It was found that alcohol added as cosurfactant could affect the solubilization of water in microemulsions (93, 94). The alcohol molecules can reside in both the aqueous and oil phases, and/or in the amphiphilic monolayer at the interface. A clear understanding of the role that the alcohol plays in the organization of the morphology of microemulsions has not yet been obtained and the problem of estimating the amount of alcohol participating at the interface of the microemulsion and in the bulk is not yet completely resolved.

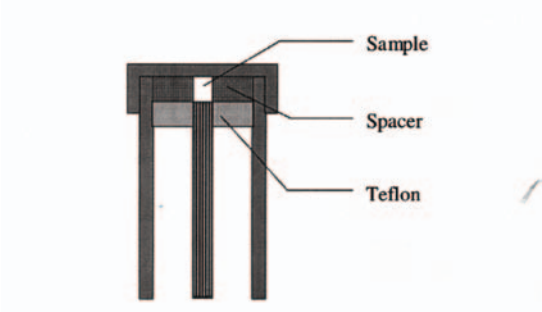

Figure 15 TDS sample cell for high-frequency for high external electric field measurements.

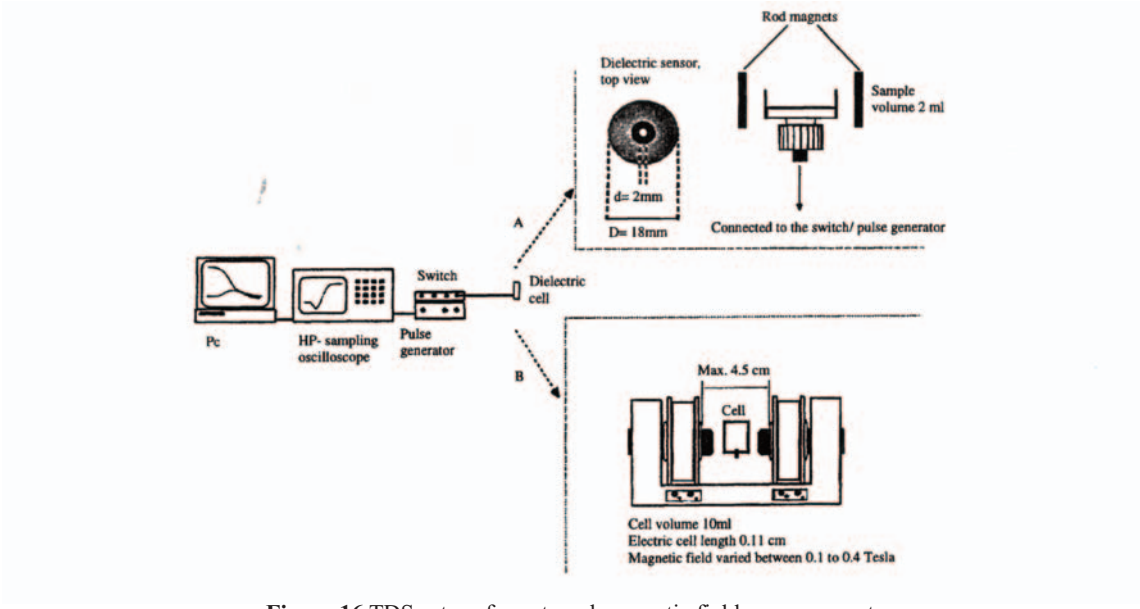

Figure 16 TDS set-up for external magnetic field measurements.

The structure of the microemulsion depends on the interaction between droplets. In the case of repulsive interaction, the collisions of the droplets are short and no overlapping occurs between their interfaces. However, if the interactions are attractive, transient droplet clusters are formed. The number of such clusters increases, when the water fraction, the temperature, the pressure, or the ratio of water to surfactant is increased, leading to a percolation in the system (95-101).

The majority of the different chemical and physical properties, as well as the morphology of microemulsions, is determined mostly by the microBrownian motions of its components. Such motions cover a very wide spectrum of relaxation times ranging from a few picoseconds to tens of seconds. Given the complexity of the chemical make up of the microemulsions, there are many various kinetic units in the system. Depending on their nature, the dynamic processes in the microemulsions can be classified into three types.

The first type of relaxation process reflects characteristics inherent to the dynamics of single droplet components. The collective motions of the surfactant molecule head groups at the interface with the water phase can also contribute to relaxation of this type. This type can also be related to various components of the system containing active dipole groups, such as cosurfactant, and bound and free water. The bound water is located near the interface, while "free" water, located more than a few molecule diameters away from the interface, is hardly influenced by the polar or ionic groups. In the case of ionic microemulsions, the relaxation contributions of this type are expected to be related to the various processes associated with the movement of ions and/or surfactant counterions relative to the droplets and their organized clusters and interfaces.

For percolating microemulsions, the second and the third types of relaxation processes are pertinent, characterizing the collective dynamics in the system and having a cooperative nature. The dynamics of the second type may be associated with the transfer of an excitation caused by the transport of electrical charges within the clusters in the percolation region. The relaxation processes of the third type are caused by rearrangements of the clusters and are associated with various types of droplet and cluster motions, such as translations, rotations, collisions, fusion, and fission.

MicroBrownian dynamics of microemulsions can be studied by various techniques including dynamic-mechanical, dielectric, ultrasonic and NMR relaxation, ESR, volume, enthalpy and specific heat relaxation, quasielastic light and neutron scattering, fluorescence-depolarization experiments, and many other methods (90, 102-107). The information thus acquired provides an opportunity to clarify

the organizational structure and the dynamic behavior of such systems.

Dielectric spectroscopy may be successful in providing unique information about the dynamics and structure of microemulsions on various spatial and temporal scales. Being sensitive to percolation, DS is expected to provide unambiguous conclusions concering the stochastic type, the long time scale cooperative dynamics, and the imposed geometric restrictions of molecular motions before, during, and after the percolation threshold in microemulsions. It also can give valuable information about fractal dimensions and sizes of the percolation clusters. On the other hand, an analysis of the dynamics on the short time scale can provide an understanding of the relaxation mechanisms in microemulsions on a geometrical scale of one microdroplet or the dynamics of surfactant or cosurfactant molecules in the interface. This is important, as it can give quantitative information about amounts of alcohol residing both in the interface and in the bulk and thus enables one to calculate the amount of bound water in the system.

The purpose of this chapter is to describe how DS can be applied to the investigation of microemulsions and how information about molecular mobility and structure can be extracted. We will show that an experimentally monitored temperature-dependent increase in ε can be explained by the temperature-dependent growth of the mean-square fluctuation dipole moment of a droplet. Analysis of the dynamic features of the known ionic and nonionic microemulsions on various time and geometrical scales will provide knowledge on both the components of the system and microdroplets as a whole. For instance, by choosing an ionic AOT/water/decane microemulsion near the percolation threshold, we can investigate the cooperative relaxation associated with charge transport in the system. By investigating a series of quaternary oil/ surfactant/cosurfactant/water microemulsions prepared with the nonionic surfactants $C_{18:1}(EO)_{10}$ or $C_{12}(EO)_8$, we can calculate the amount of alcohol residing in the interface and in the bulk phases as well as the amount of bound and free water in the system. The bound water is located near the interface and is hydrogen bonded to the hydrophilic head groups of surfactant and alcohol molecules.

A. Dielectric Spectroscopy of Ionic Microemulsions Far Below Percolation

The microemulsions formed with the surfactant, sodium bis(2-ethylhexyl) sulfosuccinate (AOT), water, and oil are widely investigated systems whose dynamics, phase behavior, and structure are well known (87-90). These microemulsions reside in the L_2 phase over a wide temperature range, i.e., the microemulsions consist of nanometer-sized spherical droplets with water in the central core surrounded by a layer of surfactant molecules. In this phase, the surfactant molecules have their hydrophilic head groups facing the water and their hydrophobic tails oriented towards the continuous oil phase. Molecules of AOT can dissociate into anions containing negatively charged head groups, SO_3^-, staying at the interface and positive counterions, Na^+, distribution in the droplet interior. There is a characteristic feature for these systems, such as a small droplet radius, comparable to the thickness of the electric double layer as measured by the Debye length. The thickness of the double layer and the distribution of mobile counter-ions within it can be calculated from the Poisson-Boltzmann equation (108, 109).

The electrical conductivity and dielectric permittivity of the ionic water-in-oil microemulsions show quite remarkable behavior when the temperature, the water fraction, pressures, or ratio of water to surfactant is varied (95-101). In our prior research (96, 97, 107), the dielectric relaxation, electrical conductivity, and diffusion properties of the ionic microemulsions were investigated in a broad temperature region. In particular, the investigation showed that ionic microemulsions start to exhibit percolation behavior that is manifested by a rapid increase in the static dielectric permittivity ε and electrical conductivity σ when the temperature reaches the percolation onset T_{on} (Fig. 17). The appearance of the percolation reveals that in the region $T > T_{on}$ the droplets from transient clusters. When the system approaches the percolation threshold T_p, the characteristic size of such clusters increases, leading to the observed increase in σ and ε. This increase in the percolation temperature region is governed by scaling laws:

$$\sigma \sim \begin{cases} (T_p - T)^{-s} & T < T_p \\ (T - T_p)^{t} & T > T_p \end{cases} \tag{44}$$

and

$$\varepsilon \sim (T_p - T)^{-s} \qquad T < T_p \tag{45}$$

characterized by critical exponents s and t. Experimentally, the critical exponents are found to have the values $s \approx 1.2$ and $t \approx 1.9$ (96). We define the percolation onset as the temperature at which the microemulsion starts to display a scal-

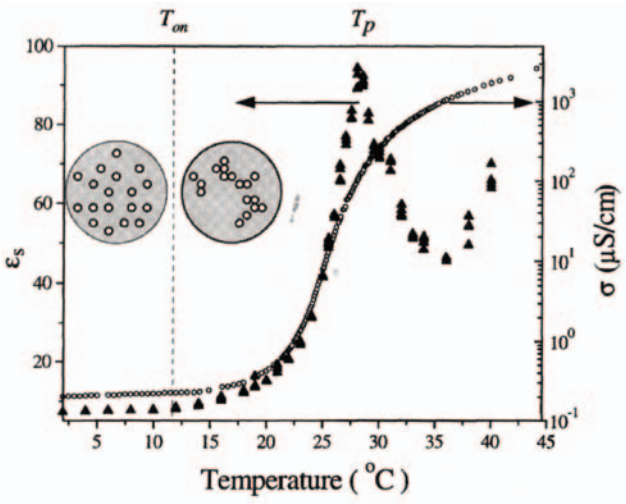

Figure 17 Schematic illustration of the structures and temperature dependence of static dielectric permittivity and conductivity for the AOT-water-decane microemulsion (17.5:21.3:61.2). (From Ref. 5. With permission from Elsevier Science B.V.)

ing behavior for conductivity [Eq. (44)] and for dielectric permittivity [Eq. (45)].

Below the percolation onset, both the conductivity σ and static dielectric permittivity ε of the microemulsions increase as a function of the volume fraction of droplets φ and/or temperature T(95-102). However, this increase is not significantly essential, as it is within the percolation region.

The increase of the conductivity versus temperature and volume fraction of droplets below the percolation onset can be described by the charge-fluctuation model (110, 111). In this model the conductivity is explained by the migration of charged aqueous noninteracting droplets in the electric field. The droplets acquire charges owing to the fluctuating exchange of charged surfactant heads at the droplet interface and the oppositely charged counterions in the droplet interior. The conductivity is then proportional to φ and T:

$$\sigma = \frac{\varepsilon_0 \varepsilon k_B}{2\pi\eta R_d^3} T\varphi \qquad (46)$$

where η is the solvent viscosity and R_d is the droplet radius.

Unlike the mechanism of increasing conductivity below the percolation onset as a function of temperature, the temperature behavior of static dielectric permittivity has been hitherto puzzling. The static dielectric permittivity of dipolar liquids ε is proportional to the macroscopic mean-square dipole moment ⟨M2⟩ of the system unit volume and inversely proportional to the temperature *T*, as ε ~&#;⟨M^2⟩ /*T*(1). However, the ionic microemulsions exhibit a growth of the dielectric permittivity as a function of temperature in the whole temperature interval.

Given the complexity of the chemical composition of the microemulsions, there are several sources of the dielectric polarization in the system. The contributions are expected to be related to the various processes connected with interfacial polarization, counterion polarization, and the motions of the anionic head groups of the surfactant molecules at the interface with the water phase (39, 96, 97, 112, 113). The contribution in polarization can also be related to various components of the system containing dipole groups, such as bound and free water (114).

The experimentally observed (95-101) increase in the dielectric polarization in the microemulsions in the nonpercolating region can qualitatively be imputed to two mechanisms. The first mechanism attributes the increase in ε below percolation to an aggregation of the spherical droplets with polarizability that is independent of temperature (115). However, an aggregation of droplets seems to be very unlikely at temperature far below the percolation region. An alternative mechanism is related to the temperature dependence of the fluctuation dipole moment of noninteracting and therefore nonaggregating droplets dispersed in oil. In order to provide the experimentally monitored temperature increase in the dielectric permittivity of a monodispersed system consisting of spherical droplets at a constant volume fraction, the value of the mean-square dipole moment τ^2) of the droplet must grow faster than the linear function of temperature.

It has been argued that the interaction of the droplets can be modulated by changing the length of the oil chain (116). In light of this, a direct approach to elucidation of the mechanism responsible for the increase in dielectric permittivity would be to investigate the temperature dependence of ε of the microemulsions built up with various oils. An understanding of the mechanisms leading to the temperature dependence of the fluctuation dipole moment, and the development of a model for the dielectric permittivity of ionic microemulsions, is also important since it will provide insight into dielectric polarization and relaxation mechanisms of such systems.

The purpose of this part is to show how the controversy was resolved concering the main mechanism that provides the temperature dependence of the dielectric permittivity in ionic water-in-oil microemul sions far below the percolation region. It was shown that dielectric permittivity does not depend on the length of the oil chains and, therefore,

aggregation of droplets cannot be responsible for the observed temperature dependence of ε (5, 117).

In order to explain the temperature behavior of ε far below the percolation onset a simple statistical model of polarization of nanometer-sized droplets containing negatively charged ions at the interface and positive counterions distributed in the droplet interior was developed (5, 117). In the framework of this model, when the values of the droplet size and the constant of dissociation of ionic surfactant are both small, an experimentally monitored temperature increase in ε can be explained by the temperature growth of the mean-square fluctuation dipole moment of a droplet.

1. Effect of Oil Chain Length on the Microemulsions

The dependence of static permittivity of the microemulsions as a function of temperature and volume fraction is shown in Fig. 18. This behavior over the measured temperature region can be analyzed in two separate intervals: below the onset of a percolation region T_{on} and above it. At the onset of percolation, the microemulsion starts to display a scaling behavior of conductivity and dieletric permittivity due to droplet aggregation. For the most concentrated microemulsion, φ = 0.38, a temperature of the percolation onset of T_{on} % 12°C was determined (98); this temperature has to be significantly higher for the more diluted microemulsions (φ = 0.26,0.13, and 0.043).

In the percolation region $(T > T_{on})$ the main origin of the steep increase in permittivity as a function of temperature (Fig. 17) is the clustering of droplets (29). We estimated (97) that at the onset of the percolation region $(T \approx T_{on})$ on the droplets have a tendency to form small dynamic, weakly bound aggregates consisting of 10 ± 5 droplets. However, far below the percolation onset the ionic microemulsion could be assumed to consist of separated nonin-teracting water droplets. Thus, the weak increase in ε far below the percolation onset might be explained either by the clustering of droplets or by another "unknown" mechanism. The mechanism should bring about the temperature increase in ε in the system in which the droplets are considered to be separated from one another and noninteracting. The hypothesis that the interaction between droplets increases with the oil chain length (116) can be examined by measuring the permittivity of two microemulsions of identical droplet size but made from different oils. According to the clustering mechanism, the effect of droplet aggregation should be more pronounced (at a given temperature) in a microemulsion containing decane rather than hexane, thus resulting in higher values of ε for the decane-containing microemulsion.

The dielectric measurements performed for the AOT/water/decane and AOT/water/hexane micro emulsions at the volume fraction of the dispersed phase of φ= 0.13 demonstrate the significant shift of the percolation region to the direction of high temperatures when the oil chain length decreased (Fig. 18) (118, 119). However, the values of ε for both the microemulsions are the same at low temperatures, i.e., below the percolation onset. Thus, those results do not support the hypothesis that the clustering can be responsible for the temperature behavior of the static dielectric permittivity at $T < T_{on}$, and it must be the internal processes within a droplet that determine the behavior of the dielectric polarization in the system.

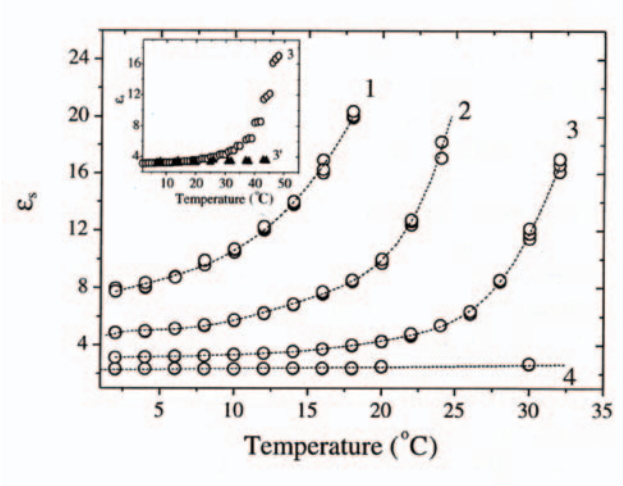

Figure 18 Static dielectric permittivity vs. temperature for the AOT-water-decane microemulsions for various volume fractions ϕ of the dispersed phase: 0.39 (1); 0.26 (2); 0.13 (3); 0.043 (4). In the inset a similar plot for the AOT-water-decane (3, ○) and AOT-water-hexane (3′, σ) microemulsions for $\phi = 0.13$. The value $W =$ [water]/[AOT] is kept constant at 26.3 for all the microemulsions. The lines are drawn as a guide for the eye. (From Ref. 5. With permission from Elsevier Science B.V.)

2. Analysis of the Dielectric Relaxation Behavior Far Below Percolation

In order to ascertain the origins and mechanisms responsible for the observed temperature behavior of the static dielectric permittivity, let us analyze the total dielectric relaxation behavior of ionic microemulsions. Dynamic aspects of the dielectric polarization can be taken into account

by considering the macroscopic dipole correlation function (DCF) $\psi(t)$ in the time domain, or the complex dielectric permittivity $\varepsilon^*(\omega)$ in the frequency domain (38). In the microemulsions, DCF is associated with the relaxation of the entire induced macroscopic fluctuation dipole moment $M(t)$, which is equal to the vector sum of all the dipole moments of the system (see Eq. 18).

It was shown (96) that ionic microemulsions exhibit a complex nonexponential behaviour that is strongly dependent on temperature. Far below the percolation onset ($T < T_{on}$) where the microemulsion has a structure of single spherical droplets, the main contribution in the relaxation mechanism comes from the fast relaxation processes with characteristic relaxation times distributed in the range from dozens of picoseconds to a few nanoseconds (96). These processes are inherent to the dynamics of the single droplet components and interfacial polarization. In the percolation region ($T > T_{on}$), transient clusters of droplets are formed as a result of attractive interactions between the droplets. The dielectric dispersion related to the clustering describes the collective dynamics in the system and has a *cooperative character*. The relaxation processes of this type are associated with the transfer of an excitation of a fluctuating dipole moment caused by the transport of electrical charges within the droplets and clusters as well as the rearrangement of the clusters. The characteristic time scale of these processes is within tens and hundreds of nanoseconds (96).

Let us consider the dynamics of microemulsions in the region $T < T_{on}$. The dependence of the macroscopic dipole correlation function $\psi(t)$ for the AOT/water decane microemulsion versus time at different temperatures is presented in Fig. 19. One can see that the dipole correlation function has a complex nonexponential behavior. In the first approximation it can be presented by the formal sum of N Debye relaxation processes as
where T, are the relaxation times and A_i are the amplitudes

$$\psi(t) = \sum_{i=1}^{N} A_i \exp(-t/\tau_c) \qquad (47)$$

of the processes. We note that $\Sigma^N_i A_i = 1$.

The interpolation of the experimental data was carried out by a least-squares fitting procedure of the DCF values. The most appropriate number of elementary Debye processes involved is determined by the minimum of the standard deviation χ^2. The dielectric response obtained reflects some properties inherent in single particle dynamics. The best-fit curves of the experimental data are reported in

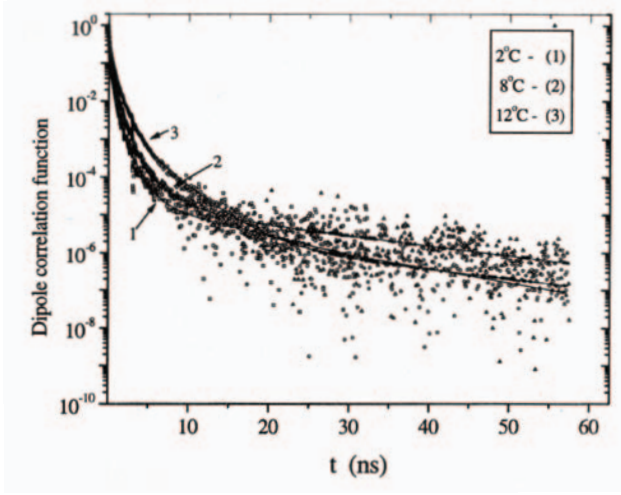

Figure 19 Time dependence of the macroscopic dipole correlation functions for AOT-water-decane microemulsion: φ = 0.38 at T= 2°C (1); T= 6°C (2); and T= 10°C (3). (From Ref. 5. With permission from Elsevier Science B.V.)

Fig. 19 (solid lines) together with the experimental data. In the temperature range 2°—12°C the best fitting gave the four elementary exponential relaxation processes (5).

The longest relaxation process with the characteristic time τ1 has a very small amplitude (~ 2%). An experimental value of τ_1 is near 10 ns. The experimental relaxation times τ2 and τ3 are within the ranges 1.2—1.6 and 0.2-0.3 ns, respectively. The amplitudes A_2 and A_3, of the second and third relaxation processes increase with the temperature. Since the amplitudes A_2 and A_3 have a similar temperature behavior, it is reasonable to associate them with the same relaxation mechanism. The fourth process seems to be distributed around 50 ps. Its experimental amplitude and relaxation time decrease with the temperature.

In order to understand this complex relaxation behavior of the microemulsions, it is necessary to analyze dielectric information obtained from the various sources of the polarization. For a system containing more than two different phases the interfacial polarization mechanism has to be taken into account. Since the microemulsion is ionic, the dielectric relaxation contributions are related to the movement of surfactant counterions relative to the negatively charged droplet interface. A reorientation of AOT molecules, and of free and bound water molecules, should also be mentioned in the list of polarization mechanisms. In order to ascertain which mechanism can provide the experimental increase in dielectric permittivity, let us discuss the different contributions.

The contribution from interfacial polarization can be es-

timated by using one of the shell models (14, 23, 27). On the basis of the Maxwell-Wagner approach, these models describe the dielectric propreties of monodispersed suspension of coated spherical particles dispersed in a continuous medium. In all cases, the assumption that the particle radius is much larger than the Debye screening length is also made. Thus, the Laplace equation is applied in order to describe the electric potential in all three phases (core, shell, and continuous medium). If the dielectric constants and electrical conductivities of the phases are known, the shell models enable us to calculate the interfacial polarization. In particular, when the electrical conductivity of the components is negligibly small, the shell models are reduced to the dielectric mixture models (14, 27, 114, 115). The numerical calculations of the contribution of interfacial polarization to the dielectric permittivity, performed on the basis of various shell models, give similar results for all the models (96, 117). For instance, in the case of the most concentrated microemulsion, the increment of the dielectric permittivity associated with interfacial polarization, determined with the help of various shell models, ranges between 3.4 and 3.7. Note that since the polarization of both water and surfactant is inversely proportional to T, the interfacial polarization will also provide a weak temperature behavior of permittivity which is inversely proportional to T, and thus does not explain the monitored increase in permittivity.

In AOT microemulsions, where the aqueous core of the droplets also contains counterions, a considerable part of the dielectric response to the applied fields originates from the redistribution of the counterions. As mentioned in Sec. II, the counterions near th charged surface can be distributed between the Stern layer and the Gouy-Chapman diffuse double layer (28-31). The distribution of counterions is essentially determined by their concentration and the geometry of the water core. Thus, for very large droplets the diffuse double layer peters out and the polarization can be described by the Schwarz model (32). However, as already mentioned, this approach is more relevant to the dielectric behavior of emulsions than to that of microemulsions.

In the opposite case of very small droplets, AOT-hydrated micelles can be considered. The high-frequency dielectric response of very small AOT reverse micelles has been analyzed (118, 119) at a molar ratio of water to surfactant of $W < 10$. The avrage radius R_W of the water core is related to W by the semiempirical relation $R_W = (1.25\ W + 2.7) +$ (13, 36). For almost dehydrated reverse micelles $R_W < 5$ A, one can expect that nearly all the counterions are bound in the surfactant layer structure and immobilized. The dynamics of such a dehydrated system with a characteristic relaxation time of a few nanoseconds has been described in terms of the rotational diffusion of the whole micelle, which represents a nearly rigid structure. On increasing R_W to 15 Å *(W* < 10), an increasing number of AOT ion pairs can achieve sufficient mobility to contribute separately to the dielectric relaxation with a characteristic relaxation time of hundreds of picoseconds. The authors restricted their consideration to the case of small droplets where most of the water and counterions are considered to be bound. They associated the dynamics in the range of hundreds of picoseconds with the rotation of completely hydrated surfactant ion pairs and neglected all bulk diffusion effects of "free" counterions in the double layer. The high-frequency dynamics detected in Refs 35 and 36, with a characteristic relaxation time significantly shorter than 100 ps, were attributed to water relaxation. We note here that the dynamics associated with reorientation of water and surfactant molecules were independent of the droplet size. Therefore, we can assume that the distributed process, found from the fitting, with a characteristic relaxation time τ_4, can be associated with the described mobility of bound water and AOT.

In the intermediate case *(W* > 10), the radius of the droplet is large enough to cause the water molecules to form a pool of free water (120). The rotational diffusion of whole droplets of our microemulsions is expected to be in the range 250-300 ns (96). We did not observe any relaxation with these characteristic times, perhaps because of the very small amplitude (<1%) of this process. One can expect that in the case of systems with intermediate droplet sizes there can be two contributions to polarization caused by counterions, one stemming from bound counterions in the Ster layer and another one from concentration polarization in the diffuse part of the double layer. It was found from counterion ^{23}Na spin-relaxation measurements that, in the intermediate region of $10 < W < 70$, the diffusion motion of counterions was in fact three dimensional rather than two dimensional (121). In particular, in the case of $W = 26.3$ the magnitude of the relative Na^+ diffusion $D_S/D_0 \approx 0.2$, where D_S is the diffusion coefficient in the surface layer of the microemulsion and D_o is the Na^+ bulk diffusion coefficient. The orientation of the fluctuating dipole moment of the droplets caused by the applied electric field is determined by the diffusion of the counterions both along the inner surface of the droplets and along the radial direction of the double layer. The characteristic relaxation time corresponding to the surface diffusion is $TS = R^2w/2D_S$. By the same token, the characteristic relaxation time for the radical diffusion of counterions can be estimated as $\tau 0 = l^2/6D_0$, where *I*Q is the Debye length. For our microemulsions we can setl_D to be of the order of the radius of a water core

R_w = 37 Å. Taking D_o as in the bulk water ($2 \times 10^5 cm^2/s$) and $D_s \approx 0.2D_0 = 0.4 \times 10^{-5}$ cm^2/s gives characteristic diffusion times of 12 and 1 ns for the surface and radial diffusion, respectively. These characteristic times agree with the observed relaxation times τ_1 and $\tau 2$, respectively. Since the amplitude of the longest relaxation process *A1* is very small (<2%) the process associated with the diffusion along the surface is not essential in the polarization. On the other hand, the amplitudes A_2 and A_3, both increase with the temperature. Thus, we assume that the three-dimensional counterion movement in the diffuse layer is responsible for the temperature rise of static permittivity at $T < T_{on}$. Hence, this diffusion movement yields the experimentally observed second and third relaxation processes.

3. Model of Dielectric Polarization of Ionic Microemulsions

a. Static Permittivity of Ionic Microemulsions

The dielectric permittivity of an ionic microemulsion can be calculated in a general way by treating it as a monodispersed system consisting of spherical water droplets dispersed in the oil medium. In this way the system is considered as a homogeneous specimen consisting of a number of charges and/or dipoles, each of which is described in terms of its displacement from the position of its lowest energy level. The permittivity ε of the system can be derived (1, 5, 117) in terms of the dielectric polarization *P* and/or the total electric dipole moment *M* of some macroscopic volume *V* in the presence of the macroscopic electric field *E* as

For ionic microemulsions the total electric dipole moment *M* can be represented as a sum of the two contributions. One is associated with the moment, M_E, due to displacements of mobile ions in the diffuse double layer, which follow the laws of statistical mechanics, and another with the moment, M_{mix}, resulting from all other displacements in the mixture (5, 117). As was discussed above, M_{mix} is related to the contributions from various processes of polarization in the microemulsion, which is treated as a heterogeneous sytem of various components.

$$\varepsilon - 1 = \frac{4\pi P}{E} = \frac{4\pi M}{VE} \tag{48}$$

It was shown (5, 117) that the permittivity ε can be described by the relationship:
where (μ) is the mean-square dipole moment of a droplet,

$$\frac{(\varepsilon - \varepsilon_{mix})(2\varepsilon + \varepsilon_{mix})(2\varepsilon + \varepsilon_w)}{\varepsilon^2} = \frac{9\varphi\langle\mu^2\rangle}{R_d^3 k_B T} \tag{49}$$

φ is the volume fraction of the droplets, R_d is the radius of the surfactant-coated water droplet, *T* is the temperature, k_B is the Boltzmann constant, and ε_{mix} is the permittivity due to polarization of the heterogeneous system. Since each droplet consists of a water core surrounded by a surfactant layer in a continuous phase prepared from oil, the effect of the interfacial polarization can be accurately regarded by using a Maxwell-Wagner mixture formula [one-shell model (14)].

Equation (49) establishes a dependence of the permittivity of a microemulsion on the temperature *T,* volume fraction of droplets φ, and apparent dipole moment of a droplet $\mu_a = (\langle\mu^2\rangle)^{\frac{1}{2}}$.

b. Fluctuating Dipole Moment of a Droplet

For calculation of the mean-square dipole moment of a droplet,$\langle\mu^2\rangle$, the theoretical development is carried out within the framework of the following assumptions (5, 117):

1. The droplets are considered identical and the interaction between them is neglected.
2. A nanodroplet contains N_a *surfactant* molecules, N_s of which are dissociated. Due to electroneutrality the numbers of the negatively charged surfactant molecules, N^-, and the number of positively charged counterions, N^+, are equal, i.e., $N^+ = N^- = N_s$.
3. The ions are treated as point charges.
4. The average spatial distribution of counterions inside the droplets is continuous and governed by the Boltzmann distribution law.
5. All the negatively charged surfactant molecules are assumed to be located in the interface at the spherical plane of radius R_w, corresponding to the radius of the droplet water pool.

In the model a single droplet is described by the spherical

coordinate system shown in Fig. 20. The dipole moment of a single droplet is given by

$$\mu = e\sum_{i=1}^{N_s}(\mathbf{r}_i^+ - \mathbf{r}_i^-) \tag{50}$$

where r_i^+ and r_i^- are the radius vectors of the positively charged counterion and negatively charged surfactant head, respectively; e is the magnitude of the ion charge.

The quantity of interest is the mean-square dipole moment $\langle\mu^2\rangle$ of a droplet. It can be expressed in terms of the mean-squared fluctuations of the dipole moment μ by

$$\langle\mu^2\rangle = \langle(\Delta\mu)^2\rangle + \langle\mu\rangle^2 \tag{51}$$

where $\langle(\Delta\mu^2)\rangle = \langle(\mu - \langle\mu\rangle)^2\rangle$. As mentioned above, the mean-square dipole moment of a droplet $\langle\mu^2\rangle$ is calculated in the equilibrium state in the absence of an electric field. In this case the calculation of the electric polarization is retained in the framework of the linear theory of the electric field one can assume a spherical symmetry of the distribution of charges within a droplet. That means $\langle\mu\rangle = 0$. Hence, the apparent dipole moment in the system has a fluctuation ntaure (5), i.e.,

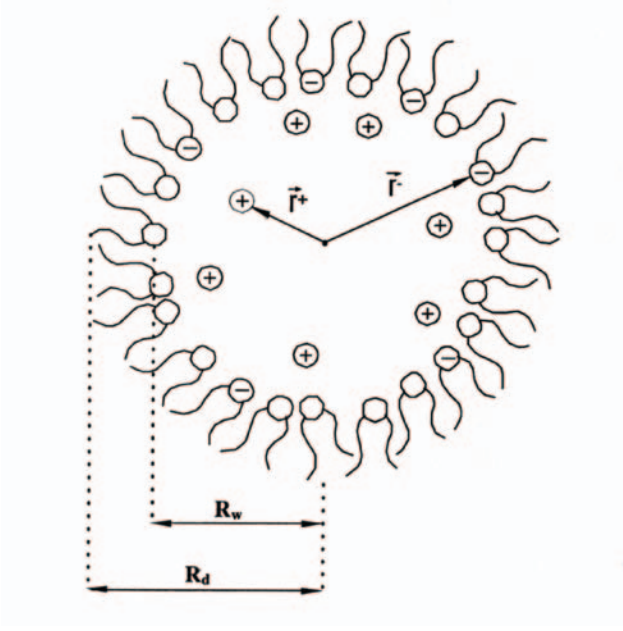

Figure 20 Schematic picture of the spherical water-surfactant droplet. The reference point is chosen at the center of the droplet. The rth ion-counterion pair is represented by radius vectors of ion and counterion, r_i^+ and r_i^-. (From Ref. 5. With permission from Elsevier Science B.V.)

$$\langle\mu^2\rangle \approx \langle(\Delta\mu)^2\rangle \tag{52}$$

In order to calculate the value of $\langle\mu^2\rangle$, we square the left- and right-hand sides of Eq. (50) and average the result by the ensemble of the realizations of random positions of ions. Retaining the main terms in the quadratic form, we then obtain:

$$\langle(\Delta\mu)^2 \approx e^2\sum_{i=1}^{N_s}\left[\langle(\mathbf{r}_i^+)^2\rangle + \langle(\mathbf{r}_i^-)^2\rangle\right] \tag{53}$$

A calculation of the terms $\langle(r_i^+)^2\rangle$ and $\langle(r_i^-)^2\rangle$ entering Eq. (53) can be performed by using the one-particle distribution functions $W_1^+(r^+)$ and $W_1^-(r)$ that are proportional to the ion density:

$$W_1^+(\mathbf{r}^+) = W_1^+(|\mathbf{r}^+|) = \frac{1}{N_S}c(r) \tag{54}$$

$$W_1^-(\mathbf{r}^-) = \frac{1}{4\pi R_W^2}\delta(|\mathbf{r}^-| - R_W) \tag{55}$$

where R_W is the radius of the water core, $c(r)$ is the density of the counterions at the distance $r=|r^+|$ from the center of the droplet, and N_S is the total number of the counterions in the droplet interior:

$$N_s = 4\pi\int_0^{R_W} r^2 c(r)dr \tag{56}$$

By taking into account Eqs (54) and (55), Eq. (53) reads

$$\langle(\Delta\mu)^2\rangle = e^2\left\{4\pi\int_0^{R_W} r^4 c(r)dr + N_S R_W^2\right\} \tag{57}$$

According to Eq. (52), relation (57) allows us to calculate the apparent dipole moment $\mu_a = (\langle(\Delta\mu)^2\rangle)^{\frac{1}{2}}$ of a droplet.

The distribution of the counterions in the droplet interior is assumed (27, 122, 123) to be governed by the Poisson-Boltzmann equation:

$$\Delta\Psi = -\frac{4\pi ec(r)}{\varepsilon_w} = -\frac{4\pi ec_0}{\varepsilon_w}e - \frac{e(\Psi(r) - \Psi(0))}{k} \tag{58}$$

Where ψ is the electrostatic potential, and ε_W is the dielectric permittivity of the water core. Here, the reference point is chosen at the center ($r = 0$) of the spherical droplet, where the counterion density is c_0 and the electric potential is $\psi(0)$.

Equation (58) reads in the dimensionless form as

$$\psi'' + \frac{2}{x}\psi' = -e^{-\psi} \tag{59}$$

with the boundary conditions:

$$\psi(0) = 0 \tag{60}$$

and

$$\psi'(0) = 0 \tag{61}$$

where ψ and x are the dimensionless potential $\psi = e[\psi - \psi(0)]/k_B T$ with respect to the center and the dimensionless distance $x = r/l_D$, respectively. Here, the characteristic thickness of the counterion layer near the surface of the water core:

$$l_D = \left(\frac{\varepsilon_w k_B T}{4\pi e^2 c_0}\right)^{1/2} \tag{62}$$

is the Debye screening length.

The Poisson-Boltzmann equation [Eq. (58)] can be solved by numerical integration (5, 123) or by expansion of the potential ψ in the radical coordinate x (117, 122). The theoretical details of the calculations were published elsewhere (117).

It was shown (5, 117) that the total number of the counterions in the droplet interior N_S can be presented in the following way:

$$N_s = 4\pi l_D^3 c_0 \sum_{j=0}^{\infty} \frac{a_j}{2j+3} x_R^{2j+3} \tag{63}$$

where $x_R = R_w/l_D$ and aj are coefficients of the logarithm of the power series in the Poisson-Boltzmann equation solution. Furthermore, using Eq. (62) and a result for the charge density $c(x)$, the relationship for the mean-square dipole moment (μ^2) of a droplet can be written as follows (117):

$$\langle \mu^2 \rangle = 4\varepsilon_w k_B T R_w^3 \sum_{j=0}^{\infty} \frac{a_j(j+2)}{(2j+3)(2j+5)} x_R^{2(j+1)} \tag{64}$$

In order to find the counterion density at the center of a droplet c_0 and entering Eq. (62) for the Debye length l_D, the counterion concentration $c(r)$ must be related to the dissociation of the surfactant molecules in the water core of the droplet. The dissociation of the surfactant molecules is described by the equilibrium relation (122, 123):

$$K_s(T) = c_0 e^{-\psi\left(\frac{R_0}{D}\right)} \frac{N_s}{N_a - N_s} \tag{65}$$

where N_a is the micelle aggregation number, K_S is the equilibrium dissociation constant of the surfactant, and $\psi(x_R)$ is the dimensionless electrical potential near the surface of the water core (i.e., at $r = R_w$). Substituting $\psi(x_R)$ in Eq. (65) with the logarithm of a power series (124) $\psi(x) = -\ln$ $\psi(x) = -\ln \sum_{j=0}^{\infty} a_j x^{2j}$ it is possible to obtain:

$$K_S(T) = \frac{c_0 N_S}{N_a - N_S} \sum_{j=0}^{\infty} a_j x_R^{2j} \tag{66}$$

The system of coupled equations [Eqs (63), (64), and (66)], along with the recurrence formula for aj (119) and Eq. (62) for l_D, constitute the model describing the temperature and geometry dependence of the mean-square dipole moment of the droplet $\langle \mu^2 \rangle$. Furthermore, by inserting the calculated values of the mean square dipole moment into Eq. (49), we can obtain the equation:

$$\frac{(\varepsilon - \varepsilon_{mix})(2\varepsilon + \varepsilon_{mix})(2\varepsilon + \varepsilon_w)}{\varepsilon^2} = 36\varphi\varepsilon_w \left(\frac{R_w}{R_d}\right)^3 \sum_{j=0}^{\infty} \frac{a_j(j+2)}{(2j+3)(2j+5)} x_R^{2(j+1)} \tag{67}$$

This enables us to calculate the values of the dielectric permittivity e of the system.

c. Approximate Relationships for the Fluctuation Dipole Moment of a Droplet and the Permittivity of Ionic Micro emulsions

An adequate approximate relationship for the calculation of the mean-square dipole moment $\langle \mu^2 \rangle$ in the case of a small droplet and/or the small dissociation of surfactant $(R_W \leq l_D)$ can be obtained as a first approximation, by taking into account the first term $(j = 0)$ only, in the series of expressions, Eqs (64)-(66). In this approximation, by using the relationship $x_R = R_W/lD$, and taking into account Eq. (62), we obtain for the mean-square dipole moment:

$$\langle \mu^2 \rangle \approx \frac{8\varepsilon_w k_B T R_w^5}{15 l_D} = \frac{32}{15} \pi e^2 c_0 R_w^5 \tag{68}$$

An approximate relationship for the counterion density at the droplet center c_0 can be obtained by using Eqs (63) and (65) in the first approximation, which reads:

$$c_0 \approx \left(\frac{3K_s}{R_w A_s}\right)^{1/2} \tag{69}$$

where $A_S = 4\pi R^2 Na$ is the average area (cm /molecule) on the surface of a water core associated with one surfactant molecule. After combining Eqs (68) and (69), the mean-square fluctuation dipole moment of a droplet becomes:

$$\langle \mu^2 \rangle \approx \frac{32\sqrt{3}}{15}\pi e^2 \left(\frac{R_w^9 K_s}{A_s}\right)^{1/2} \quad (70)$$

In order to obtain a tractable relationship for the dielectric permittivity ε, we can further simplify Eq. (49) by taking into account the relative magnitudes of ε, ε_{mix}, and ε_w. For $\varepsilon_w \approx 78$ and $\varepsilon \sim \varepsilon_{mix} \ll \varepsilon_w$, we approximate in Eq. (49) the term $(2\varepsilon + \varepsilon_w)$ by ε_w and $(2\varepsilon + \varepsilon_{mix})$ by 3ε; then, by substituting Eq. (70) into Eq. (49), we obtain:

$$\varepsilon \approx \frac{\varepsilon_{mix}}{1 - X} \quad (71)$$

where

$$X = \frac{32\sqrt{3}\pi\varphi e^2}{5R_d^3 k_B T \varepsilon_w}\left(\frac{R_w^9 K_s}{A_s}\right)^{1/2} \quad (72)$$

It is easy to show that, for small droplet concentrations, $X \ll 1$; 1; thus, an approximate relationship for e is

$$\varepsilon \approx \varepsilon_{mix}(1 + X) \quad (73)$$

In order to explain the experimental temperature behavior of the dielectric permittivity of the system we have to consider the temperature behavior of the dissociation constant of the surfactant K_S, which has an Arrhenius behavior (108):

$$K_s(T) = K_0 \exp\left(-\frac{\Delta H}{k_B T}\right) \quad (74)$$

where ΔH is the apparent activation energy of dissociation of the surfactant in the water pool of a droplet, and K_o is the pre-exponential factor. It is easy to show that the permittivity of microemulsions obtained from Eq. (71) or (73) for the Arrhenius behavior of the dissociation constant is the growing function of temperature in the temperature range $T < \frac{\Delta H}{2k_B}$. This is always fulfilled in the measured temperature interval for any reasonable value of the activation energy.

For numerical evaluations of the model we have to set the values of the parameters matching the studied systems. The value of the dielectric permittivity of water was assumed to be equal to that of bulk water at the corresponding temperature throughout all the calculations, i.e., $\varepsilon_w = 87.74 - 0.40008t + 9.39\ 8 \times 10^{-4}\ t^2 - 1.41 \times 10^{-6}\ t^3$(83), where t is the temperature in degrees Celsius. The value of 2 for the dielectric permittivity of decane was adopted in the present calculations. The effective value of 8.5 was used (125) for the dielectric permittivity of AOT. The value of ε_{mix} was calculated by using the one-shell model (14). The aggregation number N_a was estimated to be 244 molecules per droplet. The value of $A_S = 65$ Å^2 was adopted for the average area on the surface of the water core associated with one AOT molecule (115).

Note that the developed model can only be applied within the special ranges of the droplet radius and ionic dissociation of the surfactant. From one side, the droplets cannot be too small. The radius of the water core must be larger than 15 A (water-to-surfactant ratio $W > 10$) to ensure that a core of "free" water exists (118). On the other hand, the droplets cannot be too large, since the applicability range of the solution Eq. (68) is restricted by the condition $R_w < 3.27/LD$. This condition may also be expressed in terms of the strength of the electrolyte in the droplet interior $pK_S (pK_S = -\log K_S)$ and/or by the degree of dissociation of surfactant $\alpha = NsNa$ (5, 119). Regarding K_S of the surfactant AOT, little is known and we did not find any reliable experimental data for it in the literature. Thus, K_S can be considered as an adjustable parameter of the theory which can be calculated from the inverse problem, i.e., we can determine K_S from a knowledge of the experimentally measured permittivity of the studied microemulsions. The equilibrium dissociation constant *Ks* can be calculated by using Eqs (62), (66), and (67) or, in the case of small droplets and/or a low degree of surfactant dissociation, by the approximate equation (71).

Figure 21 compares the values of the experimental apparent dipole moment μ_a of the studied microemulsions, obtained from Eq. (49), together with the theoretical values obtained on the basis of Eq. (67). One can see that the apparent dipole moment $\mu_a = (\langle \mu^2 \rangle)^{1/2}$of the microemulsions increases versus temperature. For all the microemulsions studied the magnitude of the dipole moments for various volume fractions φ of the dispersed phase does not depend on φ within a degree of accuracy better than 10%, which confirms the assumption of the model that droplets in the system can be considered as noninteracting for such concentrations of droplets.

As a final comment, let us briefly discuss the permittivity of the studied microemulsions. Figure 22 shows the temperature dependencies of the experimental permittivity and the results of the calculations on the basis of the developed model performed by using Eqs (67) and (71). The difference between the values of e obtained from these formulas can only be observed at high ε. The calculated values of *s* agree well with the experimental data in the region far below the onset of percolation ($T < T_{on}$), where the assumptions of the model are fulfilled. At temperatures close

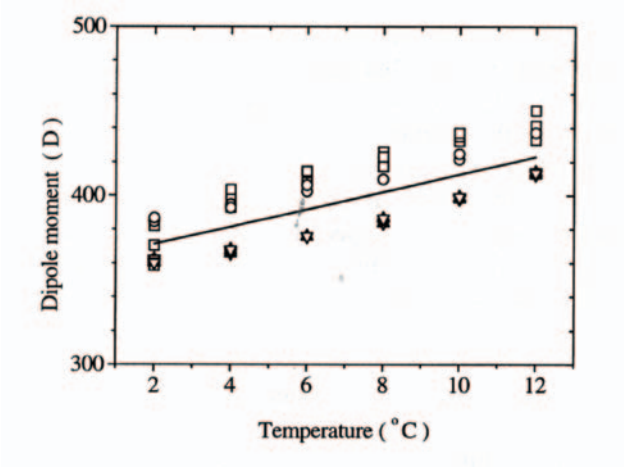

Figure 21 Temperature dependence of experimental [and calculated on the basis of Eq. (64)] macroscopic apparent dipole moments of a droplet of the AOT/water/decane microemulsions. Experimental values for the dipole moment are shown for various volume fractions ϕ of the dispersed phase: 0.043 (□ ; 0.13 (○); 0.26 (Δ); and 0.39 (∇). Calculated values are shown by the solid line. (From Ref. 5. With permission from Elsevier Science B.V.)

to the percolation onset T_{on} and beyond it, deviations in the theoretical values from experimental data are observed. These deviations indicate the structural changes in the system that appear at percolation.

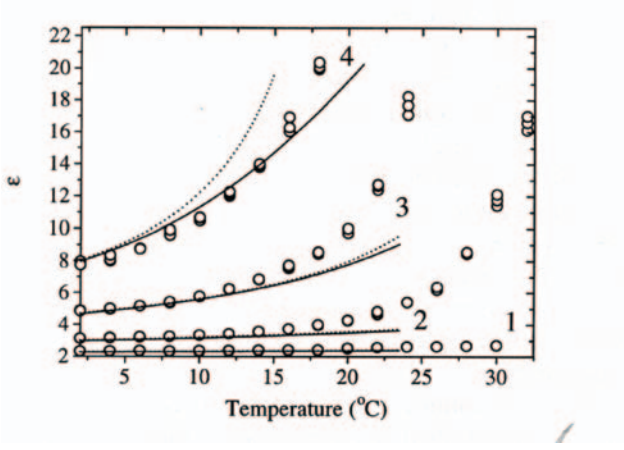

Figure 22 Experimental (○) and calculated static dielectric permittivity vs. temperature for the AOT-water-decane microemulsions for various volume fractions ϕ of the dispersed phase: 0.39 (curve 1); 0.26 (curve 2); 0.13 (curve 3); 0.043 (curve 4). The calculations were performed by using the formulas: Eqs. (67) and (71) (dashed line). (From Ref. 117. With permission from American Physical Society.)

B. Dielectric Properties of Ionic Microemulsions at Percolation

A percolation phenomenon was found in ionic micro-emulsion droplets when the water fraction, the temperature, the pressure, the strength of the electric field, or the ratio of water to the surfactant was varied (95-98, 101). Basically, the percolation behavior is manifested by the rapid increase in electrical conductivity σ and static dielectric permittivity e as the system approaches the percolation threshold (Fig. 17).

The dielectric-relaxation properties in sodium bis(2-ethylhexyl) sulfosuccinate (AOT)/water/decane micro-emulsion near the percolation temperature threshold have been investigated in a broad temperature region (96, 97, 107). It was found that the system exhibits a complex nonexponential relaxation behavior that is strongly temperature dependent. The time-decay behavior of the dipole correlation function of the system Ψ (t) was deconvoluted into normal modes and represented as a sum of a few Kohlrausch-Williams-Watts (KWW) terms, $\exp[-(t/\tau_M)^{\nu}]$, each with characteristic macroscopic relaxation times, τ_M, and stretched exponents, v, respectively (96). It was shown that, in the percolation region, transient clusters of a fractal nature are formed because of attractive interactions between droplets. An interpretation of the results was carried out in the framework of the dynamic percolation model (126). According to this model, near the percolation threshold, in addition *to the fast relaxation* related to the dynamics of droplet components, there are at least two much longer characteristic time scales. The *longest process* has characteristic relaxation times greater than a few microseconds and should be associated with the rearrangements of the typical percolation cluster. The temporal window of the intermediate process is a function of temperature. This *intermediate process* reflects the *cooperative relaxation phenomenon* associated with the transport of charge carriers along the percolation cluster (126-128).

For a description of the mechanism of cooperative relaxation, Klafter, Blumen, and Shlesinger (KBS) (129, 130) considered a transfer of the excitation of donor molecule to the acceptor molecule through many parallel channels in various condensed media. The KBS theory might be modified for describing the process of the charge transfer in colliding droplets forming a cluster and giving rise to the relaxation of the entire fluctuation dipole moment. The normalized decay function α(t) in the microemulsions is associated with the relaxation of the entire induced macroscopic fluctuation dipole moment $\overline{M}(t)$ of the sample of unit volume, which is equal to the vector sum of all the fluctuation

dipole moments of droplets.

The relaxation of the fluctuational dipole moment of a droplet is related to the transfer of the excessive charge (excitation) within two colliding droplets from a charged droplet (donor in the KBS model) to a neutral droplet (acceptor). The theoretical details of the model has been published elsewhere (97). This model of cooperative relaxation can be applied to fractal media such as the ionic microemulsion represented in the percolation region.

In the framework of the theory of cooperative relaxation in fractal media it is shown (97) that the macroscopic dipole correlation function $\psi(t)$ of the system is given by

$$\Psi(t) = \exp\left\{\Gamma\left[g\left(\frac{t}{\tau}\right)N, k, v\right]\left(\frac{t}{\tau}\right)^{v} + B(v)\left(\frac{t}{\tau}\right)\right\} \qquad (75)$$

where the coefficient $\Gamma[g(t/\tau), N, k, v]$ depends on the microscopic relaxation function $g(t/\tau)$ describing the elementary act of a charge transfer along the percolation cluster on the scaling parameters k, characterizing the type of the fractal similarity, and on the number of stages of self-similarity of the clusters N (Fig. 23). The r is the microscale relaxation time describing the charge transfer between two neighboring droplets. The coefficient $B(\upsilon)$ is a correction for the KWW function at large times. The parameter υ in Eq. (75) characterizes the cooperative dynamics and structure of the fractal clusters. The relationship between the exponent υ and the fractal dimension D_f is given by $D_f = 3\upsilon$ (97).

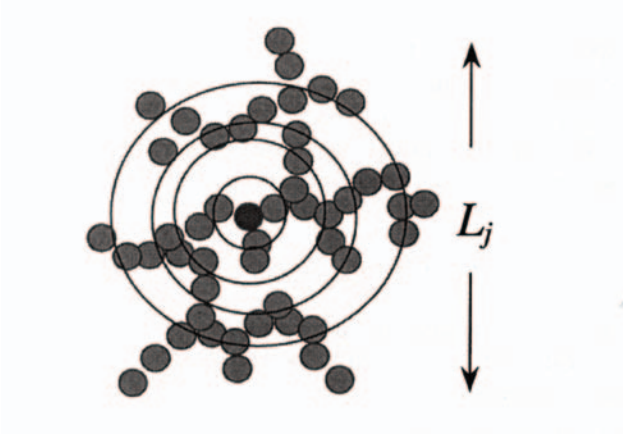

Figure 23 Schematic picture of the excitation transfer via parallel relaxation channels in the fractal cluster of droplets in the percolating microemulsions.

As noted above, the dynamical processes in micro-emulsions can be classified into three types. The first type of relaxation process reflects characteristics inherent to the dynamics of the single-droplet components. The second and third types of relaxation processes characterize the collective dynamics in the system and have a cooperative nature.

A detailed analysis and estimations of the relaxation-time values show (5, 96) the following hierarchy of processes on the time scale: the relaxation processes of the first type τ_1 are the fastest, with an order of hundreds of picoseconds, when compared with the time τ_c, needed to explore the cluster and with the rearrangement time, τ_R. The rearrangements occur on timescales of microseconds (128) and are considered the slowest process. The intermediate process ($\tau_1 < \tau_c < \tau_R$), relating to the cooperative transport of charge carriers along the clusters, has a temporal window depending on temperature. The minimal time boundary is of the order of hundreds of picoseconds, whereas the maximal time boundary has a value of tens of nanoseconds at the beginning of the percolation region and reaches 700 ns at T_p. All these contribute to a complex behavior of the dielectric correlation function. We can suppose, therefore, that near the percolation threshold the main contribution to the dynamics results from the cooperative effect related to the transfer of charge carriers along the percolation clusters, as given by Eq. (75).

The typical decay behavior of the dipole correlation function of the microemulsion in the percolation region is presented at Fig. 24. Figure 25 shows the temperature dependence of the effective relaxation time, τ_{eff}, defined within the fractal parameters, and corresponding to the macroscopic relaxation time τ_m of the KWW model. In the percolation threshold T_p, the τ_{eff} exhibits a maximum and reflects the well-known critical slowing down effect (131).

The stretched exponent υ depends essentially on the temperature (Fig. 26). At 14°C, υ has a value of 0.5. However, when the temperature approaches the percolation threshold $T_p = 27$°C, υ reaches its maximum value of 0.8, with an error margin of less than 0.1. Such rapid decay of the KWW function at the percolation threshold reflects the increase of the cooperative effect of the relaxation in the system. At temperatures above the T_p, the value of the stretched exponent v decreases, and indicates that the relaxation slows down in the interval 28°-34°C. At temperatures above 34°C, the increase in υ with the rise in temperature suggests that the system undergoes a structural modification. Such a change implies a transformation from an L_2 phase to lamellar or bicontinuous phases (132, 133). On the other hand, the temperature behavior of the fractal dimension D_f (Fig. 26) shows that below the percolation

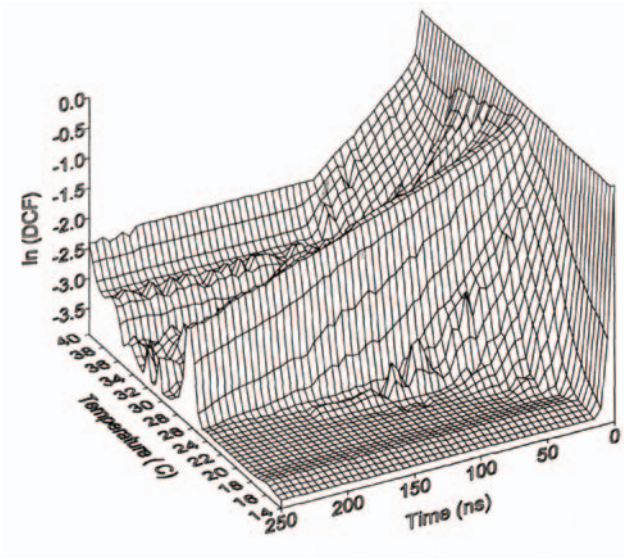

Figure 24 Three-dimensional plots of time and temperature dependence of the macroscopic dipole correlation function for the AOT-water-decane microemulsion. (From Ref. 97. With permission from American Physical Society.)

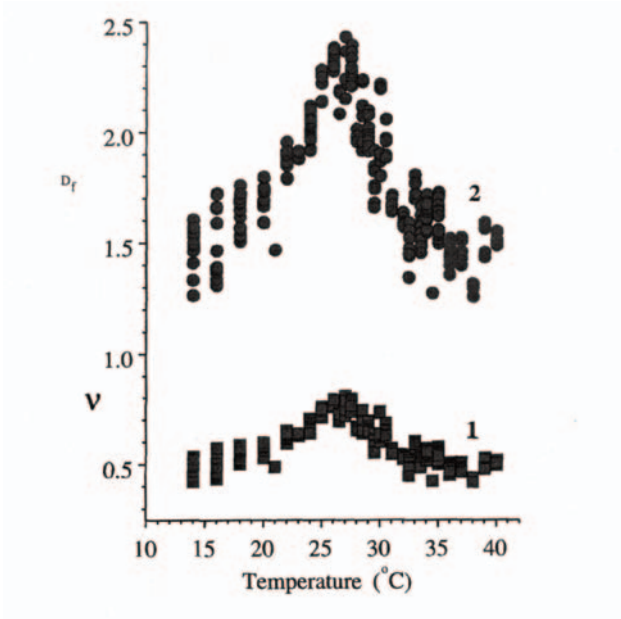

Figure 26 Temperature dependence of the stretching parameter υ (□) and fractal dimension D_f (○). (From Ref. 97. With permission from American Physical Society.)

threshold $D_f < 2$. This corresponds to a system of small clusters dispersed in space and can be described by the model of unbounded fractal sets with a D_f of less than 2 (134, 135).

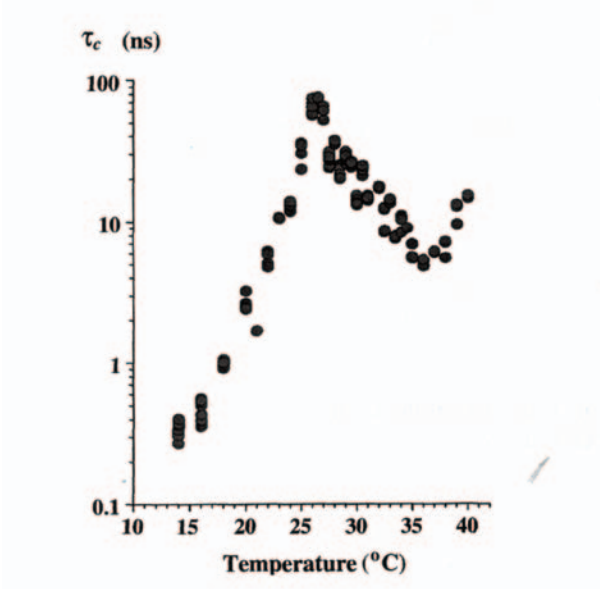

Figure 25 Temperature dependence of the macroscopic effective relaxation time τ_{eff}. (From Ref. 97. With permission from American Physical Society.)

At the percolation threshold $D_f = 2.4 \pm 0.2$, satisfactorily concurring with the literature value of 2.5 (136). Above the percolation threshold D_f decreases, which can be explained by reorganizations of the system with corresponding structural changes. A structural modification of the system at temperatures above 34°C and the appearance of more prolonged and/or ordered regions in the microemulsion leads to a new observable increase in D_f.

It was shown that the effective length of the clusters increases sharply (97, 136) and diverges in the percolation threshold in accordance with the percolation scaling law $L_N \sim (T - T_p)^{-\upsilon_g}$ where υ_g is the geometrical exponent (131). However, dispersion of the data obtained from the fitting does not enable one to estimate precisely a critical exponent υ_g of this growth.

The typical number of droplets S in the aggregates may be estimated according to the relationship given by

$$S \sim (L_N/d_{drop})^{1/D_f} \tag{76}$$

where d_{drop} is the diameter of the surfactant-coated water droplet, estimated to be 100 Å. The temperature dependence of the number of droplets in the typical fractal cluster *S* is presented in Fig. 27.

Analysis of the temperature behavior of the calculated parameters shows that at the onset of the percolation region the droplets have a tendency to form small dynamic aggre-

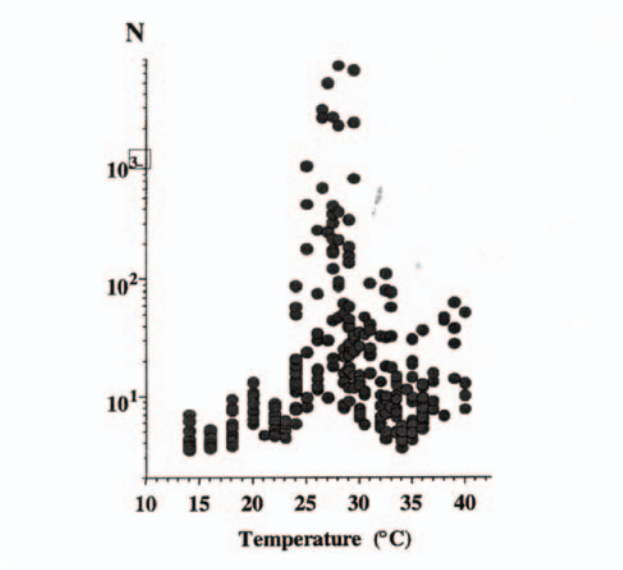

Figure 27 Temperature dependence of the number of droplets in a typical percolation cluster. (From Ref. 97. With permission from American Physical Society.)

gates consisting of 10 ± 5 droplets that are weakly bound. The characteristic length of such aggregates changes in the interval L_N~600—1000 Å. The fractal dimension at these temperatures has a value of less than 2, indicating that the aggregates are surrounded by empty spaces, i.e., separated from another. We note that each of these aggregates participates in the relaxation as independent objects with no correlation between them. At the percolation threshold, the aggregates tend to form a large percolation cluster, which participates in the cooperative relaxation as a whole object.

The fractal model described above enables us to relate the characteristics of a total cooperative macroscopic relaxation function with the parameters of the fractal medium (fractal dimension D_f and the degree of the development of fractality which is expressed by the number of self-similarity stages N). Herewith, the fractal medium has been represented by the single effective self-similar geometric structure. The recursive model neither describes the cluster polydispersity (cluster size distribution), nor the relaxation of the individual cluster. Therefore, it is expedient to use the complementary model in order to estimate cluster statistics and dynamics in more detail. Such a model might be developed in the framework of the general statistical description. In this description, the DCF of a complex system is represented as a result of averaging of the dynamic relaxation functions corresponding to the different random states of the system (99, 137):

$$\Psi(t, s_m) = \int G(t, s) W(s, s_m) \mathrm{d}s \qquad (77)$$

where $W(s, s_m)$ is the state probability density distribution function for the state variable s, depending on the effective maximal scale s_m, and $G(t, s)$ is the dynamic relaxation function in state s. The integration in Eq. (77) is performed over all possible states of the system.

For the percolation case, the function $W(s, s_m)$ was taken in the form of the generalized exponential distribution or main statistical distribution as follows (138—140):

$$W(s) \sim s^{\gamma} \exp[(s/s_m)]^{\eta} \qquad (78)$$

where γ is the polydispersity index, $s_m \gg 1$ is the cutoff cluster size, and $\eta > 0$ is the cut-off rate index. The numerical values of these parameters depend on the distance from the percolation threshold. Above the percolation threshold, i.e., at $u > 0$, the function $W(s)$ describes the size distribution of all clusters except for the infinite cluster. In the continuum limit, the function $W(s)$ is the cluster size probability density distribution function. Herewith, the state variable s is just the cluster size (number of monomers in the cluster). The form of $G(t, s)$ was chosen with the help of the hypothesis of dynamical scaling as $G(t, s) = \exp[-t/\tau(s)]$, where $\tau(s) = \tau_1 . s^{\alpha}$, τ_1 is the minimal time associated with the monomer relaxation, and the parameter α is the scaling index establishing a correspondence between the size of a cluster and its relaxation time. The tentative application (140) of the statistical fractal model validated the usefulness of the statistical approach. The treatment performed on the experimental data suggested that the polydispersity index, the dynamic scaling exponent, and the σ exponent are not universal quantities and that they might depend on the specific interactions in the system. Further development of that approach will give an effective tool for investigation of the polydispersity index, the dynamic scaling exponent, and other structural and dynamical parameters of microemulsions in percolation.

C. Dielectric Properties of Nonionic Microemulsions

Analysis of the dynamics on short time scales can unravel the nature of the relaxation processes and provide information about the partition of the water and alcohol between bulk and interface. It was shown

(141-143) that nonionic microemulsions usually have a very complicated dielectric behavior. From the Cole-Cole plot, for example, Fig. 28, it can be seen that the complete dielectric spectrum cannot be described by a single relaxation process. The wide nonuniform time window used (38) allows one to deconvolute the relaxation spectrum to distinguish three or four relaxation processes (dependent on water content and temperature) distributed in the interval between 10^{-11} and 10^{-9}s. Given the complexity of the chemistry of micro-emulsions, a precise interpretation of the dielectric relaxation mode is difficult. Dielectric relaxation contributions in such systems are expected to be related to bound and free water, alcohol molecules, and active dipole groups belonging to the surfactant molecules and associates.

1. Evaluation of the Amount of Alcohol at the Interface

Two main dielectric relaxation processes can be considered in nonionic microemulsions. The longest one, with characteristic time changes between 1 and 2 ns down to hundreds of picoseconds with increasing water content in the system, and the shorter relaxation rpocess that is characterized by time changes from 100 ps down to dozens of picoseconds. The long-term behavior has been correlated with the self-associated state of the alcohol and associated with the break-up of linear alcohol complexes. The relaxation time is related to relaxation of the alcohol in microemulsions at various water contents and can be juxtaposed with that of oil-alcohol mixtures for various concentrations of alcohol in the system.

The two relaxation processes were evaluated both for the alcohol/dodecane mixtures (Fig. 29) and for the microemulsions (Fig. 30). In order to understand the way to calculate the amount of alcohol at the interface and in the oil phase, let us first analyze the alcohol/ dodecane binary mixture.

a. The Alcohol/Dodecane Binary Mixture

In such mixtures the long relaxation time τ_1 increases with increasing concentration of butanol in dodecane (Fig. 29a). In other words, diluting butanol with oil leads to a long relaxation-time reduction. The decrease in τ_1 with the oil concentration is in good agreement with the literature (144-146). On the other hand, the short relaxation time τ_2 is hardly affected by the presence of dodecane. The same behavior between the alcohol concentration and the relaxation times was detected in a pentanol/dodecane mixture (Fig. 29b).

Aliphatic alcohols are known to be strongly associated polar liquids. Alcohol molecules in the liquid phase are linked into oligomer chains by intermolecu-lar hydrogen

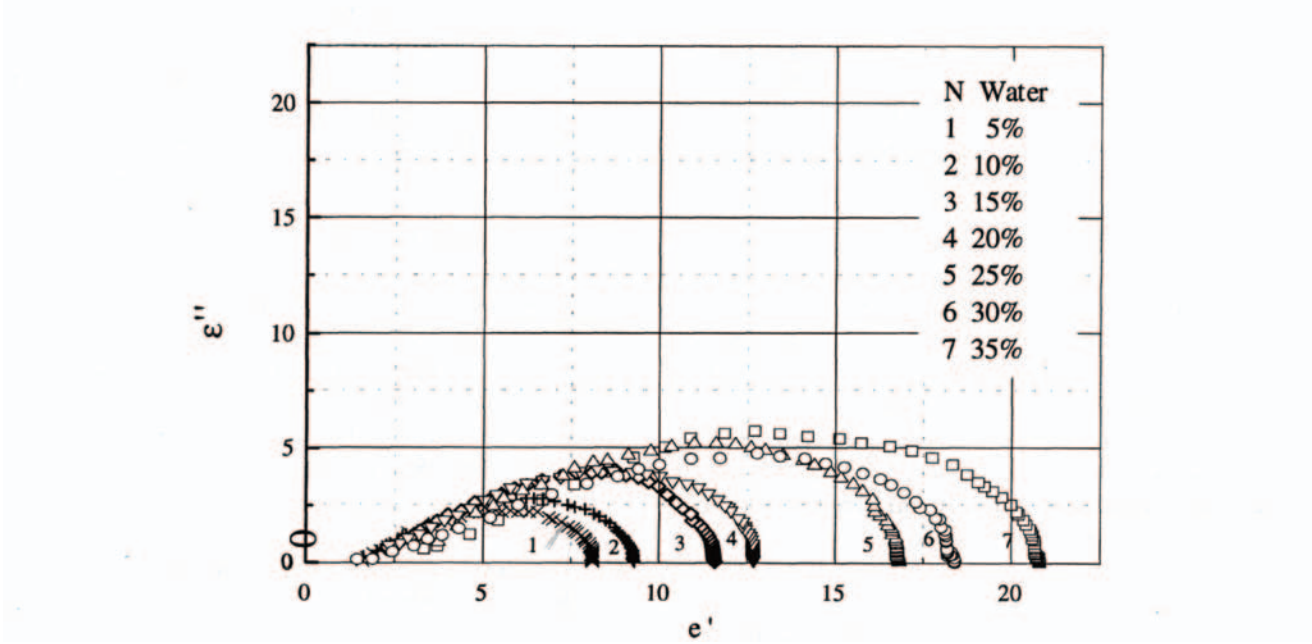

Figure 28 Cole-Cole diagram for seven mixtures of W/O dodecane/butanol/Brij 97/water microemulsions at 20°C for various water contents: 5% (1); 10% (2); 15% (3); 20% (4); 25% (5); 30% (6); 35% (7). (From Ref. 143. With permission from Elsevier Science.)

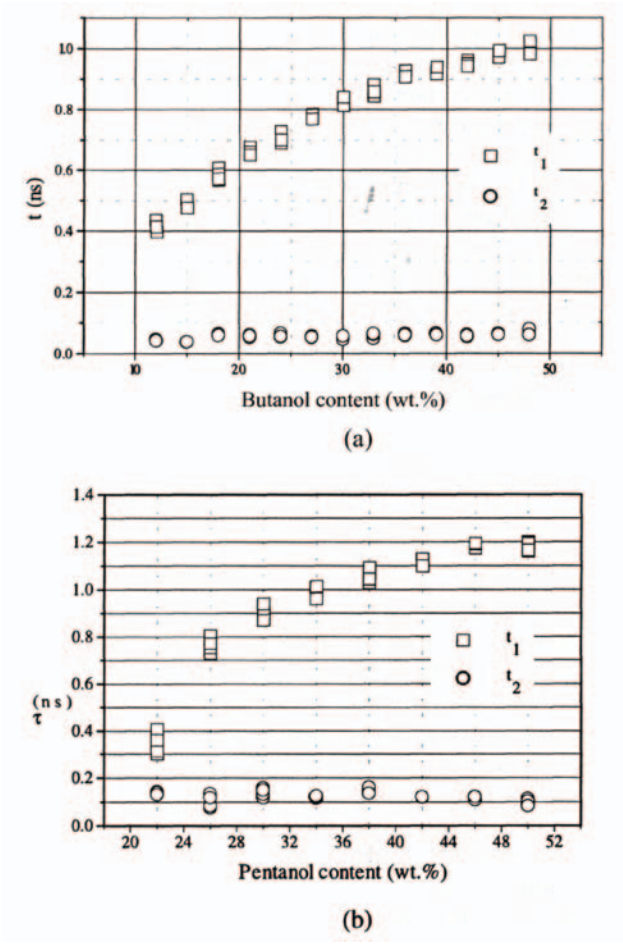

Figure 29 Dielectric relaxation times of dodecane/alcohol mixtures at 10°C for different alcohol contents (a) dode-cane/butanol; (b) dodecane/pentanol. (From Ref. 141. With permission from Elsevier Science.)

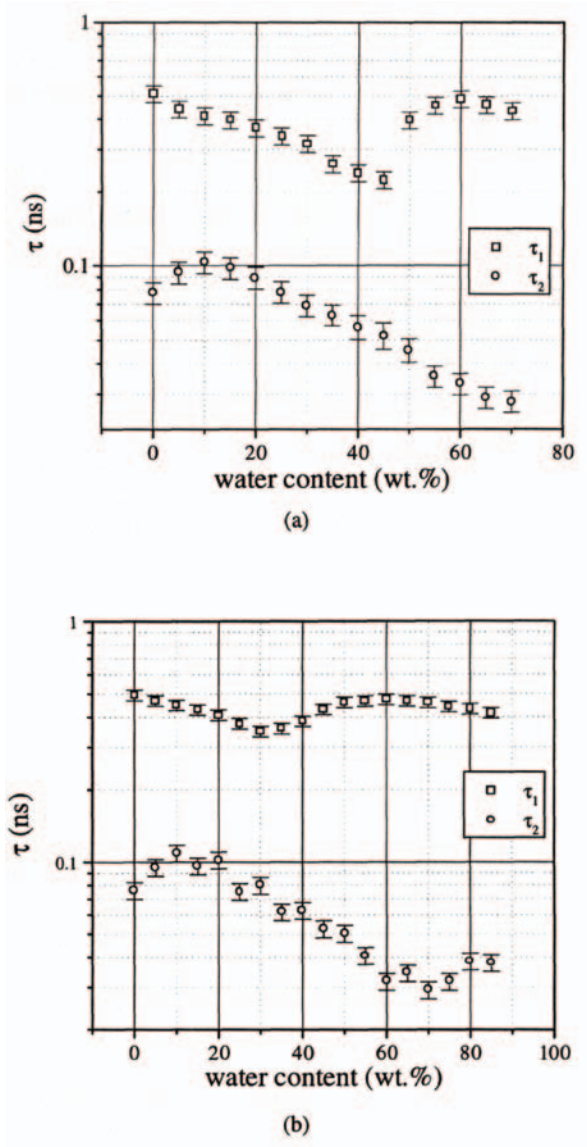

Figure 30 Dielectric relaxation times at 10°C of (a) dode-cane/butanol/Brij 97/water microemulsion (system 1) and (b) dodecane/pentanol/$C_{12}(EO)_8$/water microemulsions (system 2), for different water contents. (From Ref. 141. With permission from Elsevier Science.)

bonds (H-bonds) (147-149). The alcohol molecules are able to rotate around the H-bonds, resulting in the associated species existing mainly in the convoluted form. In the general case, rotation around the H-bonds is partially hindered, and the longer the hydrocarbon radical, the stronger is the hindering.

As the nonpolar dodecane is dispersed in the alcohol medium, the alcohol chains are disrupted and broken into smaller clusters. As more dodecane is introduced into the mixture, alcohol complexes become smaller until the alcohol appears as monomers, i.e., nonclustered alcohol (144-146).

The long dielectric relaxation process (presented here by τ_1) has been correlated with the self-associated state of the alcohols. It is caused by a cooperative relaxation of the average dipole moment of the whole alcohol aggregate in the pure alcohol or in the alcohol/ dodecane mixture (148). Therefore, the long relaxation process will exist only in the presence of alcohol aggregates. It was shown (149) that the long relaxation time of the alcohol is related to the average

number of monomers in the alcohol cluster n, and to the relaxation time of the alcohol monomers' isotropic rotation τ' by the relation:

$$\tau = 6n\tau' \qquad (79)$$

As a result of adding the hydrocarbon, smaller units of alcohol aggregate are created, and according to Eq. (79) this will lead to a decrease of the long relaxation time τ_1.

The short dielectric relaxation process (presented here by τ_2) is associated with the anisotropic motion of the monomer alcohol species in a chain cluster (149). In microemulsions, the short process is the superposition of several dielectric relaxation processes, which have similar relaxation times such as movement or rotation of the alcohol monomers, hydrate water, and surfactant polar head groups. The short relaxation time is barely affected by the alcohol concentration in the mixture since it is less sensitive to the aggregation process.

b. The Microemulsion Systems

As previously discussed, the alcohol in the studied microemulsion is located in the oil phase or in the water aggregate's interfacial film. Thus, the continuous phase of the microemulsion is actually an alco-hol/dodecane binary mixture (neglecting a very small amount of water). Since the alcohol located at the interface exists as monomers, the long relaxation time observed in the microemulsion is associated with an alcohol aggregate that is only present in the continuous phase with the dodecane. In Fig. 30 it can be seen, both for Brij 97 and the C_{12} $(EO)_8$ systems, that in the range of the L_2 phase (0-50% of water), as water is added to the microemulsion, the long relaxation time τ_1 decreases. This phenomenon can be explained as follows: as more water is introduced into the system some of the alcohol (butanol or pentanol) migrates from the continuous oil phase to the interface. As mentioned above, when the alcohol concentration in the dodecane phase decreases, the alcohol clusters became smaller, reflected by a reduction of the long relaxation time. The same phenomenon of decreasing the long relaxation time with increasing water content was observed in systems containing Brij 97 with butanol as cosurfactant (Fig. 30a) and C_{12} $(EO)_8$ with pentanol as cosurfactant (Fig. 30b).

The average association number *n* of the alcohol molecules is determined by the alcohol concentration in the oil. The dependence of the association number *n* of butanol and pentanol as a function of the alcohol concentration in binary mixtures is presented in Fig. 31. The association number was calculated from the long dielectric relaxation time of the binary mixture using Eq. (77) and taking τ' as 7.1 ps for butanol and 10.4 ps for pentanol (146).

The oil phase of the microemulsion can be considered as a binary mixture of dodecane and alcohol. In this case, by using Eq. (79), it is possible to calculate the association number of the alcohol molecules in the oil phase from the long relaxation time of the microemulsion (Fig. 32). For the $C_{12}(EO)_8$/water/dodecane/ pentanol microemulsions the association number varies in the range from 4 to 6 (Fig. 32a). From Fig. 31 it can be seen that these *n* values are in the range of 21 to 24% of pentanol in dodecane. Thus, we estimate that the pentanol concentration in the oil phase of $C_{12}(EO)_8$/water/dodecane/pentanol microemulsion decreases just slightly in the range (21-24%) when water is added. Since the total amount of each component in the microemulsion is known, it is easy to calculate the partition of the alcohol between the oil phase and the interface. From such calculations we can evaluate that, for the microemulsions with high water content (60%), 70% of the pentanol is located at the interface and 30% is dissolved in the oil. As mentioned before, this ratio changes slightly when the water content in the microemulsion is changed.

Adding water to the microemulsion can in some cases cause an inversion from the L_2 to the L_1 phase.

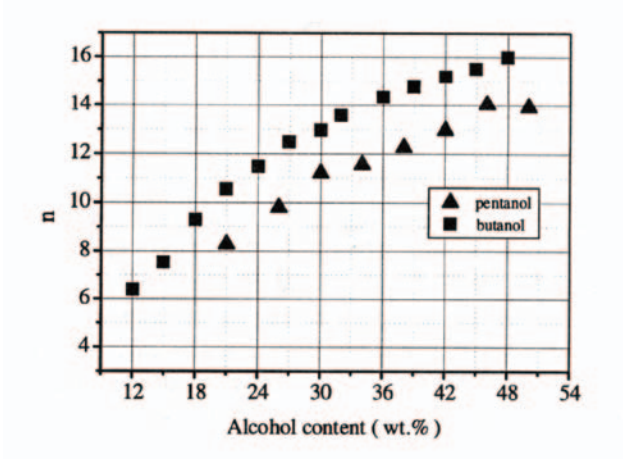

Figure 31 Association number *n* at 10°C, of alcohol molecules vs. its concentration in alcohol/dodecane mixtures. The association number was calculated from the long dielectric relaxation time of the binary mixture using Eq. (77). (■) Butanol/dodecane; (▲) pentanol/dodecane. (From Ref. 141. With permission from Elsevier Science.)

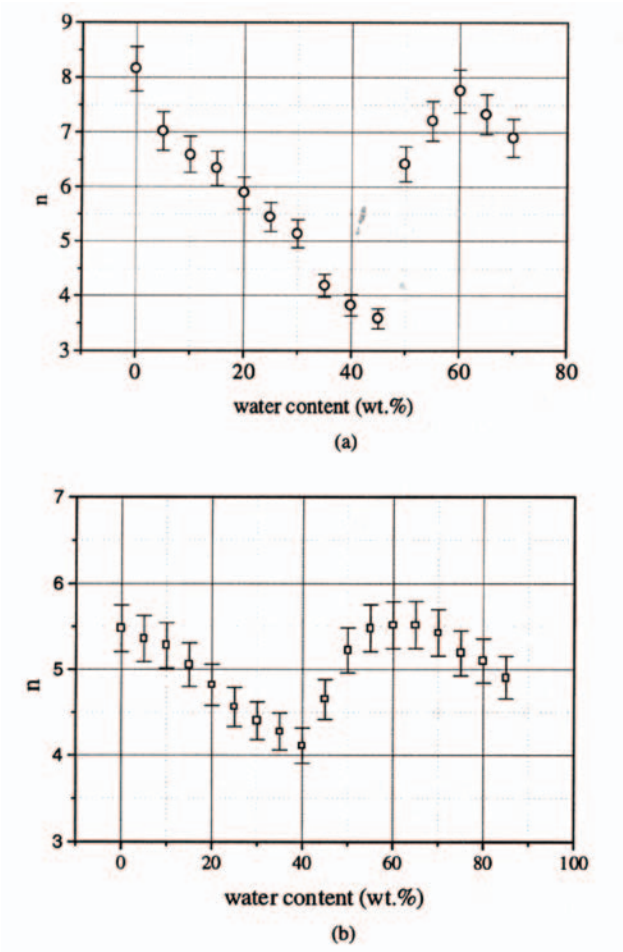

Figure 32 Association number *n* at 10°C, of alcohol molecules in the oil phase of the microemulsions with different water contents. The association number was calculated from the long dielectric relaxation time of microemulsions. (a) (System l)dodecane/butanol/Brij 97/water microemulsions; (b) (system 2) dodecane/pentanol/$C_{12}(EO)_8$/water microemulsions. (From Ref. 141. With permission from Elsevier Science.)

In our system the inversion was found to be in the range 45-60 wt % water. In Fig. 32 it can be seen that the dielectric long relaxation process τ_1 and the association number *n* increase abruptly at 50% water concentration. This kink is more evident in the Brij 97-butanol system. It is reasonable to believe that this kink, which occurs in the inversion area, is due to expulsion of part of the alcohol from the interface to the oil phase. As it happens, the concentration of the alcohol in the oil phase increases and the long relaxation time increases. Hence, the inversion can be detected by the TDS method.

2. Evaluation of the Amount of Bound Water in Microemulsions

Information about the bound water fraction in some colloid systems, silica gels, and biological systems is usually inferred on the basis of the frequency- and time-domain DS measurements from the analysis of the dielectric decrements or the relaxation times (64, 150-152). However, the nonionic microemulsions are characterized by a broad relaxation spectrum as can be seen from the Cole-Cole plot (Fig. 33). Thus, these dielectric methods fail because of the difficulties of deconvoluting the relaxation processes associated with the relaxations of bound water and surfactant occurring in the same frequency window.

In microwave dielectric measurements (> 30 GHz) the dielectric permittivity and dielectric losses for bound and free water show significantly different magnitudes. Thus, in measurements at high microwave frequencies the contribution from bound water in the dielectric losses will be negligibly small, and the contribution from the free water fraction can be found. In contrast to the above-mentioned procedures used for calculation of bound water from the relaxation spectrum analysis, this approach will not involve analyses of overlapping relaxation processes and can thus easily be applied to microemulsions having a complex relaxation spectrum.

It is necessary to choose a model that will adequately describe the dielectric properties of the micro-emulsion. Most of the existing theories (106, 153) operate with a system consisting of well-defined geometrical structures such as spherical or ellipsoidal

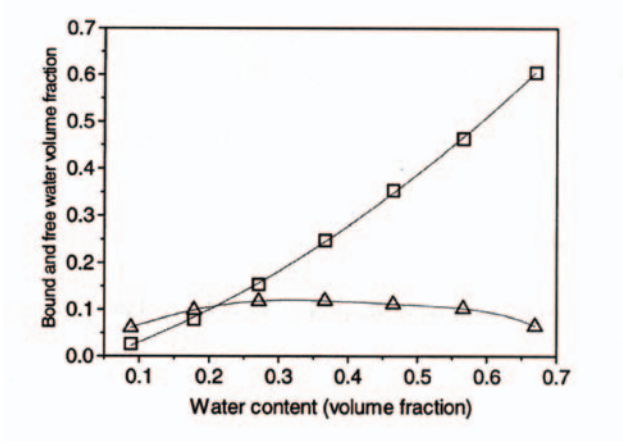

Figure 33 Relative amounts of free (□) and bound (△) water contents of the investigated microemulsion vs. total water content. (From Ref. 141. With permission from Elsevier Science.)

droplets, cylindrical or flat lamellars, etc. Since it was not known how the morphology of the microemulsion system changes with the addition of water, an approach suggested by Kraszewski and coworkers (154, 155) for the prediction of the permittivity mixture was applied. In this case, the relationship relating complex permittivity of the microemulsion with those of its components and their volume fractions may be written:

$$\sqrt{\varepsilon^*} = \varphi_m\sqrt{\varepsilon_m^*} + \varphi_f\sqrt{\varepsilon_f^*} + \varphi_b\sqrt{\varepsilon_b^*} \tag{80}$$

where φ_m denotes the volume fraction of the system occupied by the microemulsion without added water (i.e., dry microemulsion consisting of dodecane, butanol, and Brij 97), and φ_f and φ_b are the volume fractions of free and bound water, respectively. The volume fractions are calculated per unit volume of microemulsion. The complex permittivities of the entire system, the microemulsion with no added water, and free and bound water, are represented by ε^*, ε^*_m, ε^*_f, and e^*_b, respectively.

Since the volume fractions of free, φ_f, and bound, φ_b, water are both unknown, it is convenient to measure the dielectric permittivity in a frequency range where the dielectric loss of bound water may be safely neglected. The relaxation spectrum of free and bound water for our systems will safely satisfy this requirement at the measurement frequency of 75 GHz. In this case, the complex permittivity of the bound water is equal to its real part, i.e., $\varepsilon^*_b = \varepsilon'_b + i0$. For the sake of simplicity, calculations of the complex dielectric constant can be written in polar coordinates, $\varepsilon^* = \mathbf{R}\exp(i\theta)$, where $\mathbf{R} = (\varepsilon'^2+\varepsilon''^2)^{1/2}$ and $\tan\theta = \varepsilon''/\varepsilon'$ Now $\exp(i\varepsilon) = \cos\theta + i\sin\theta$; therefore, substituting the corresponding terms in polar coordinates in Eq. (80) for the dry microemulsion, free and bound water, respectively, then rearranging and separating the imaginary parts, one can obtain the following relationship for the calculation of the bound-water fraction (156):

$$\varphi_b = \frac{\sin\left(\frac{\theta_m}{2}\right)\sqrt{R_m} - \sin\left(\frac{\theta_e}{2}\right)\sqrt{R_e} - \sin\left(\frac{\theta_w}{2}\right)\sqrt{R_w} - \varphi_m\left[\sin\left(\frac{\theta_m}{2}\right)\sqrt{R_m} - \sin\left(\frac{\theta_f}{2}\right)\sqrt{R_f}\right]}{\sin\left(\frac{\theta_f}{2}\right)\sqrt{R_f}} \tag{81}$$

Figure 33 shows the volume fraction of free, φ_f, and bound water, φ_b, in the microemulsion, calculated from Eq. (81), as a function of the total water content, φ_w. As long as there are unoccupied binding sites at the interface on the surfactant head groups and on the cosurfactant molecules, the increase in φ_w leads to an increase in φ_b. The bound-water fraction shows a maximum between 0.30 and 0.40 of the total water volume fraction, corresponding to 0.12 of bound-water volume fraction. Further addition of water dilutes the alcohol and surfactant, decreasing the number of active centers, which are able to absorb water molecules. Thus, the bound water fraction φ_b decreases after reaching the maximum.

Figure 34 plots the volume ratio between bound water and the total water amount versus water contents. The fraction of bound water decreases with increasing total water content in the system. As more water is introduced into the system, the interface approaches saturation and it is less favorable for additional water to be bound. The dilution effect described above also leads to this decrease.

Water molecules can be bound to both ethylene oxide (EO) groups of Brij 97 and to the hydroxyl (OH) groups of butanol. Unfortunately, it is not known for this system how many molecules are bound to either alcohol or surfactant. Therefore, two curves are presented in Fig. 35. The curves demonstrate the number of bound water molecules calculated per EO group and per EO + OH group versus the total water content, respectively. As the water content increases, the number of water molecules bound to EO or EO + OH groups increases and reaaches a maximum at ~ 2.5 molecules for one curve and ~ 1.5 for the other. This increase means that the water-binding centers do not become saturated until ~ 0.6 of the total water volume fraction is ob-

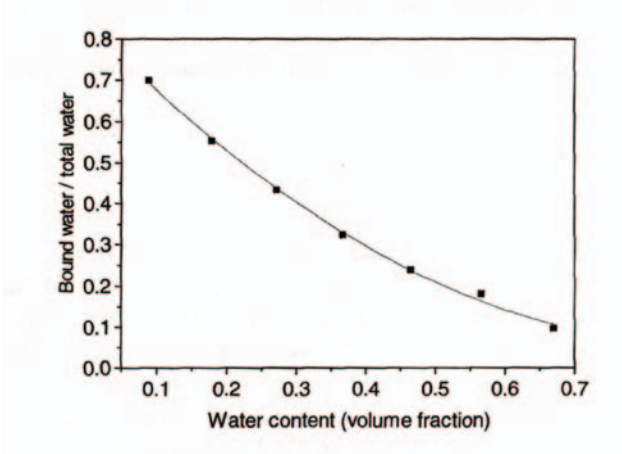

Figure 34 Ratio of bound water-to-total water content (volume of bound water divided by volume of total water) vs. water content. (From Ref. 141. With permission from Elsevier Science.)

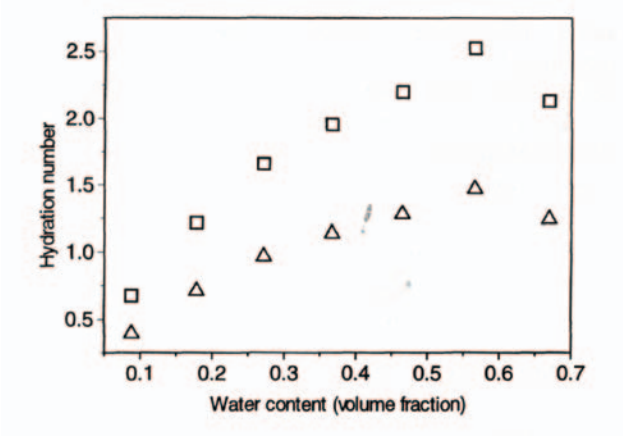

Figure 35 Number of bound water molecules for the investigated microemulsion calculated per ethylene oxide (EO) group (□) and per EO + OH group (△) vs. the total water content. (From Ref. 141. With permission from Elsevier Science.)

tained. The decrease in the number of bound water molecules per EO or EO + OH group can be due to changes in the morphology of the system above 0.6 of the water volume fraction content. The number of bound water molecules per EO group at saturation obtained from the analysis of the dielectric properties, 2.5, is in good agreement with that obtained by differential scanning calorimetry (DSC) (157), 2.8, for a similar system. However, DSC measurements may be performed only after the samples have been cooled to a very low temperature, while the microwave dielectric method can be applied at any desired temperature.

In this section we have demonstrated the potential of time-domain dielectric spectroscopy in obtaining information about both the structure and dynamics of ionic and nonionic microemulsions on different temporal scales.

V. NONEQUILIBRIUM COLLOIDAL SYSTEMS

Emulsions and suspensions of solid particles are common examples of colloidal systems that are not in the equilibrium state. As the systems destabilize and approach the equilibrium state, several processes will be involved. Typically, flocculation, sedimentation, and coalescence, etc., take place simultaneously at more or less well-defined rates, continuously changing the properties of the system.

Flocculation leads to strongly reduced interparticle distances. Also, the sedimentation process alters the particle distribution throughout the system, leading to a particle density gradient. The size distribution will change as a result of coalescence or coagulation.

There is a constant challenge for improved techniques in order to make accurate predictions on the colloidal stability of various sytems. In this section we demonstrate how dielectric spectroscopy can be applied as a technique to follow the breakdown of water-in-oil emulsions and to monitor the sedimentation of particle suspensions. Dielectric spectroscopy, combined with statistical test design and evaluation, seems to be an appropriate technique for the study of these problems. However, one should continue to seek satisfactory theoretical models for the dielectric properties of inhomogeneous systems.

A. Dielectric Properties of Emulsions

We have restricted this presentation to involve only oil-continuous emulsions. The reason for excluding water-continuous systems is that the O/W emulsions are usually stabilized by means of ionic surfactants (or surfactant mixtures) and consequently the electric double-layer effects can be very large. The electrode polarization will normally also be very strong in many O/W systems. For the TDS technique water-in-oil emulsions stabilized by means of nonionic surfactants are very good model systems.

1. Effect of Flocculation

Theoretical models for the dielectric properties of heterogeneous mixtures [for instance, Eq. (20), or extensions of this model] are commonly applied in order to explain or predict the dielectric behavior also of emulsions (106, 158). However, in the present theories a homogeneous distribution of the dispersed phase is required. This requirement is rarely fulfilled in a real emulsion system where the inherent instability makes the emulsions go through different stages on the way towards complete phase separation. Processes like sedimentation, flocculation, and coalescence continuously alter the state of the system (Fig. 36). These processes also influence the dielectric properties (159—162). Thus, the dielectric properties of one given sample may vary considerably over a period of time (160), depending on the emulsion rate.

The effect of flocculation on the dielectric properties of disperse systems is well documented, both when it comes to suspensions of solid particles and emulsions.

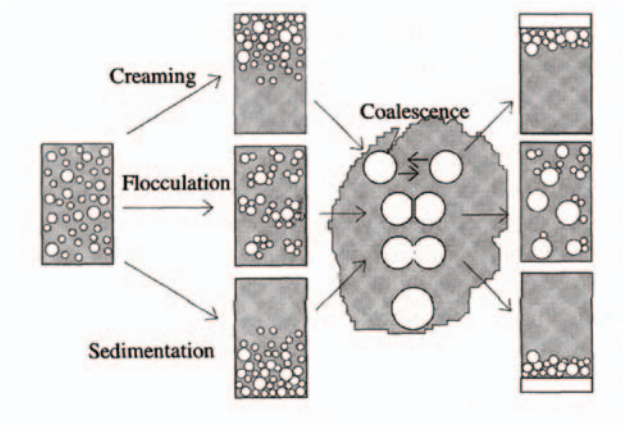

Figure 36 Schematic view of some of destabilizing processes that may take place in an emulsion, eventually leading to complete phase separation. Similar processes also take place in other types of disperse systems.

Genz *et al*. (163) found that the conductive and dielectric properties of suspensions of carbon black in mineral oil was highly dependent on shear. When a shear force was applied to the suspensions, flocculated aggregates were torn apart and a reduction in the permittivity levels was observed. When the shear stopped, the permittivity rose to previous levels. Thus, the reversibility of the shear-induced floc disintegration could be followed by means of dielectric spectroscopy.

Also, Hanai (11) exposed his systems to shear. In order to verify his theory on the dielectric properties of concentrated emulsions (161, 62), dielectric measurement on W/O emulsions were performed at rest and under influence of shear forces. At rest the static permittivities by far exceeded the values predicted from Eq. (20). However, when modestly high shear forces were applied, Hanai found good agreement between measured and predicted values. Also, in this case the reduction in permittivity upon shear was ascribed to a disintegration of floes.

Table 1 Dielectric Parameters for a W/O Emulsion Containing 50 vol % water, Stabilized by 1 % Berol 26. The Aqueous Phase Contains 5 wt% NaCl. Measurements Have Been Performed Both during Emulsification (Using Different Methods) and at Rest (Immediately after Emulsification).

Device	Rotation speed (r.p.m.)	ε_s During mixing	ε_s At rest	ε_∞ During mixing	ε_∞ At rest
Laboratory mixer	≈ 2500	15.6	24.2	9.4	11.0
	(≈ 500)	16.9	20.9	10.4	11.3
Vortex mixer		15.4	23.9	11.0	12.9

Source: Ref. 164.

Table 1 gives the results from a simple experiment visualizing the effect of stirring on the dielectric properties of emulsified systems (164). It is seen that the difference in the static permittivity between the emulsions during stirring and at rest can be as high as 50%. In this case the volume fraction of water is constant, so the only difference between the measurements is in the state of the emulsions. Visually, no phase separation could be detected, so the difference must be due to flocculation or sedimentation, leading to a reduced droplet-droplet distance. However, the variations cannot be so large that they promote coalescence, since this was not visually observed. In a study of model W/O emulsions containing different amounts of water (Table 2) (165) it was found that dielectric models based upon spherical, noninteracting droplets could not predict the permittivities found. In order to obtain agreement between measured values and predicted ones the traditional models on heteroge-

Table 2 Dielectric Parameters Obtained Experimentally for Different Water-in-Crude Oil Emulsions, Together with Corresponding Shape Factors Found from Comparison with Theoretical Parameters (Eq. 19)

Experimental values				Oblate spheroids ($0 < A < 1/3$)			Prolate spheroids ($1/3 < A < 1/2$)		
ϕ	ε_s	ε_∞	τ (ns)	$A^{\varepsilon s}$	$A^{\varepsilon\infty}$	A^{τ}	$A^{\varepsilon s}$	$A^{\varepsilon\infty}$	A^{τ}
0.17	17.5	6.5	0.8	0.06	0.06	0.06	0.48	0.49	0.48
0.23	22.4	7.4	1.0	0.08	0.09	0.07	0.48	0.48	0.48
0.28	28.2	9.6	1.0	0.09	0.09	0.08	0.47	0.48	0.47
0.38	35.7	13.2	1.3	0.12	0.12	0.10	0.46	0.47	0.47
0.44	46.0	13.5	1.2	0.14	0.14	0.14	0.46	0.45	0.46
0.50	60.0	14.0	1.3	0.15	0.16	0.13	0.45	0.43	0.46

Source: Ref. 165.

neous mixtures were modified, taking a flocculated state of the emulsions into account.

a. Linear floes

In a first approach, it is assumed that the flocculated aggregates can be considered as spheroids, as depicted in Fig. 37. By further assuming that the volume of the floc equals the volume of the droplets, and neglecting any interactions over the thin films separating the droplets, the overall permittivity can be predicted by use of Eq. (21) or (22). The floes are in this case characterized by one single variable, namely a shape factor, A. The easiest way to interpret A is to consider a linear floc-culation (see Fig. 37) and to define an axial ratio between the major and minor axes. When doing so, corresponding axial ratios were found to be in the range from 1:3 to 1:10 (165). However, a small linear flocculation is not entirely consistent with the complex structures a flocculated system can build up. Other more complex flocculation models have also been developed.

b. Floes as Subsystems

An alternative approach is where the aggregates, formed as a result of flocculation, are treated as subsystems of the emulsions (166). The dielectric properties of the subsystems will be decisive for the dielectric properties of the overall system.

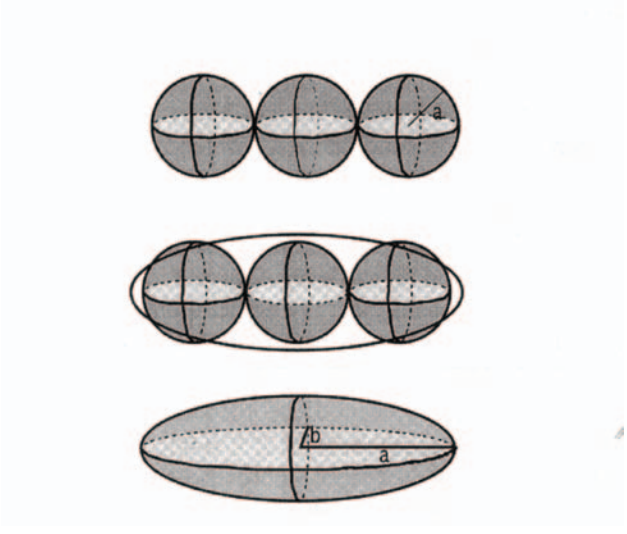

Figure 37 Linear floes: if the droplets form small linear aggregates, the floc aggregates can be treated as spheroids and can as such be characterised by the axial ratio a/b (or consequently by the shape factor A) as introduced in Eq. (20).

In floe aggregates some of the continuous phase is entrapped between the emulsion droplets. Thus, the volume occupied by a floc will exceed the volume of the individual droplets building up the floc (Fig. 38). The volume fraction occupied by floes, ϕ_f, can be expressed as

$$\phi_f = \frac{V_f}{V} = \frac{V_f V_d}{V_d} \Big/ V = \phi \frac{V_f}{V_d} = \frac{\phi}{\phi_{d,f}}, \quad (\phi < \phi_{d,f} < 1) \tag{82}$$

where V_f and V_d are the volumes of the flocs and droplets, respectively, V is the total volume of the system; ϕ is the volume fraction of disperse phase with regard to the total volume, whereas $\phi_{d,f}$ is the volume fraction of disperse phase with regard to the floc volume. The factor $\phi_{d,f}$ is a measure on the packing of the droplets in the floes, i.e., a small value of $\phi_{d,f}$ means a loose structure, and a large value represents a densely packed floc.

Assuming that the droplets retain a spherical shape, the permittivity for the floes, ε^*_f, can be calculated by using Eq. (20):

$$1 - \phi_{d,f} = \left(\frac{\varepsilon_f^* - \varepsilon_1^*}{\varepsilon_2^* - \varepsilon_1^*}\right)\left(\frac{\varepsilon_2^*}{\varepsilon_f^*}\right)^{1/3} \tag{83}$$

We can then proceed to calculate the total permittivity ε^* for the system, now treating the floes as the disperse phase, at a concentration that equals ϕ_f:

$$1 - \phi_f = \left(\frac{\varepsilon^* - \varepsilon_f^*}{\varepsilon_2^* - \varepsilon_f^*}\right)\left(\frac{\varepsilon_2^*}{\varepsilon^*}\right)^{3d,f} \times \left(\frac{\varepsilon_2^*(1+3A_f) + \varepsilon_f^*(2-3A_f)}{\varepsilon^*(1+3A_f) + \varepsilon_f^*(2-3A_f)}\right)^{3K,f} \tag{84}$$

By use of Eq. (84) we allow for a spheroidal shape of the floes, as expressed through the parameters A_f, 3d, f and 3K, f. In this model the flocculated aggregates are characterized by the packing density of the droplets in the floc and a shape factor.

c. Two-component Model with a Partial Flocculation

In the approaches above (i.e., Sec. V.A.I.a and V.A.I.b) a complete flocculation, i.e., that all droplets are part of a floc, is taken for granted. This is seldom the case, and the situation sketched in Fig. 39 is more likely to occur. The system properties are then dependent both on the permittivity and volume fraction of the free droplets as well as on the floc permittivity and $\phi_{p,f}$.

The following expression, derived by Hanai and Sekine (167) gives the permittivity of a system where two different

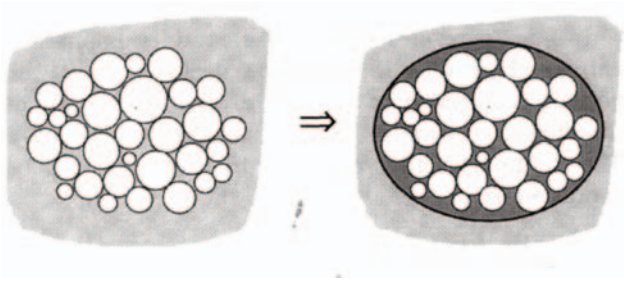

Figure 38 Floes treated as subunits: the floes are treated as subunits, with a volume fraction of droplets in floe (or the floe density), ϕ_{df}, that is higher than the overall volume fraction ϕ. Some of the continuous phase will be entrapped between the droplets in the floe. Thus, the volume of a floe exceeds the total volume of the droplets in it. The floe shapes are assumed to be spheroidal.

types of spherical particles are dispersed in the same system:

$$\ln(1-\phi) = \frac{1}{3}[\log \varepsilon_2^* - \log \varepsilon^*] + A[\log(\varepsilon^* - \alpha) - \log(\varepsilon_2^* - \alpha)] + B[\log(\varepsilon^* - \beta) - \log(\varepsilon_2^* - \beta)] \quad (85)$$

where A, B, α, and β are functions of the permittivities $\varepsilon_{1,j}$ and $\varepsilon_{1,k}$ and of the ratio ϕ_{df}/ϕ_j, where the subscripts j and k represent the two different kinds of particles; ε_2 is the dielectric permittivity of the continuous phase. In Eq. (85) "In" denotes the natural logarithm of a real number whereas "log" is the principal value of the complex logarithm; 0 is the total volume fraction particles in the system, i.e., $\phi=\phi_j + \phi_k$ [Similar expressions for multicomponent systems with randomly oriented spheroids have been derived by Boned and Peyrelasse (24).]

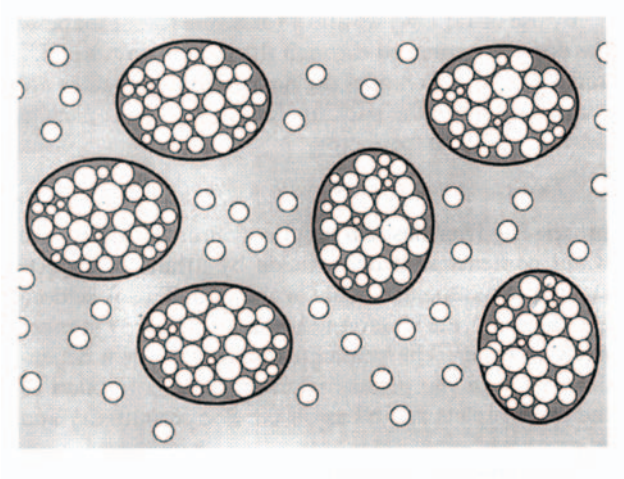

Figure 39 Model for partial flocculation.

If we treat the free water droplets as one type of particle and the floes as the other type, Eq. (85) may be used to find the dielectric properties of a partially flocculated emulsion.

The dispersed water, present at a concentration 0, is distributed between two states, either as free droplets, or bound in the floes. We can write

$$\phi = \phi_w^{\text{Free}} + \phi_w^{\text{Bound}}$$

The volume fraction of floes in the system (ϕ_f) is related to ϕ_w^{Bound}through

$$\phi_f = \phi_w^{\text{Bound}} \phi_{d,f}$$

where $\phi_{d,f}$ is the volume fraction droplets in the floes, as in the previous section. To apply Eq. (85) the total volume fraction occupied by the two "components" is needed and

$$\phi_{\text{Total}} = \phi_w^{\text{Free}} + \phi_f = (\phi - \phi_w^{\text{Bound}}) + \frac{\phi_w^{\text{Bound}}}{\phi_{d,f}}$$

Thus, for a given ϕ we can have a wide range of different systems, as we can freely vary ϕ_w^{Free} and $\phi_{d,f}$ within the limits $\{0 < (\phi - \phi_w^{\text{Bound}}) < \phi$ and $\theta < \theta_{d,f} < 1\}$.

Common tor all models presented is that, by the right choice of parameters, one can theoretically predict static permittivities that match experimental values for W/O emulsions, and that are higher than those predicted from the models presuming a homogeneous distribution of spherical emulsion droplets. However, there are more features to the dielectric spectrum than just the static permittivity, and for the models to be deemed useful in characterizing emulsion properties they should be able to reproduce also the frequency dependence of permittivity. In other words, the complete relaxation process must be satisfactorily accounted for. When the models above have been fitted to experimental data we have experienced only a limited success in finding sets of floe parameters that yield theoretical spectra in accordance with the experimental ones (164, 165, 168, 169). Taking into account the multitude of possible configurations of the systems after flocculation, this is not unexpected, and an effort still has to be made before the dielectric properties of flocculated systems can readily be predicted.

2. Electrocoalescence

In a strong electric field the aqueous droplets in a W/O emulsion become polarized due to ion separation in the

droplets. This polarization will create an opposite field inside the water droplets. As a consequence we will have a flocculation of aqueous droplets, a so-called bridging, between the electrodes. The potential difference between droplets may be written as:

$$V_{pot} \propto Er\cos\theta \qquad (86)$$

where E is the applied field, r is the droplet dimension, and θ is the angle to the applied field. With a droplet radius of 10 μm, an applied field of 0.5 kV/cm, and droplets parallel with the external field, the potential will be of the order of 0.5 to 1.0 V. Under these conditions the field over the surfactant membrane ($\approx 2l_{surfactant}$) separating two aqueous droplets is of the order of 10_6 V/cm. This is a very high local field that can create an ion transport over the surfactant film. When the ions start to cross the film a coalescence of adjacent droplets will take place. However, this transport requires a certain level, V_{crit}, before it will take place; V_{crit} can hence be taken as a measure on the emulsion stability (52). Below V_{crit} different kinds of phenomena can take place. For a single-droplet assembly one can predict a substantially increased level of flocculation, i.e., the static permittivity should increase under these conditions. If the emulsion is already in a flocculated state the applied voltage may first of all alter the droplet size distribution towards larger droplets and hence also the size of the floes. As a consequence a drop in ε_S can be predicted. However, when the applied field is switched off the original floe size and structure will be slowly obtained and a relaxation process towards the original ε_S can be observed. The level of irreversible distortions in the droplet sizes can determine a difference in the initial ε_S and the $\varepsilon_S$after relaxation.

a. Percolation Phenomena in W/O Emulsions in High Electric Fields

Figure 40 shows the static permittivity of an asphal-tene-stabilized model W/O emulsion versus the applied external electric field (170). The static permittivity increases with the applied electric field. This is an indication of a low degree of attraction between the aqueous droplets and, initially, a low level of flocculation. The applied electric field will induce a flocculation that consequently leads to an increase in ε_S First to a small extent only, later more pronounced as the critical voltage is approached. However, when the critical electric field is exceeded, a steep decline in the static permittivity to a value of 5-7, is observed. This can be viewed as a percolation phenomenon according to a static model (171, 172).

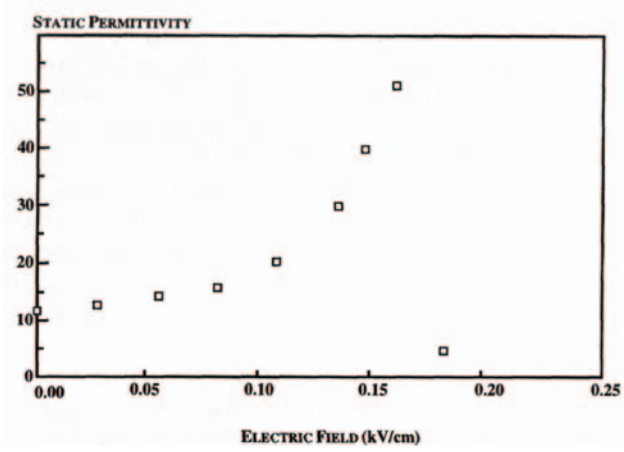

Figure 40 Static permittivity of an asphaltene-stabilized model emulsion vs. the applied external electric field. The percolation behavior is clearly seen. (From Ref. 170.)

From studies of the percolation phenomena in W/O microemulsions it has been proposed that permittivity follows a scaling law with regard to temperature (96). However, when we induce the percolation by applying a high electric

$$\varepsilon_S \sim (E_{cr-E})^{-S} \qquad (87)$$

field, the following scaling law may apply:
where $E < E_{cr}$. From linear regression analysis, the critical exponent s can be estimated from the slope. The data from Fig. 40 will give a slope of 0.52, which is close to the theoretical value expected from a static percolation model (s = 0.6) containing bicontinuous oil and water structures (172).

3. Dielectric Spectroscopy on Technical Emulsions (Gas Hydrate Formation)

Literature reports on a variety of applications of dielectric measurements in different types of technical processes. The classical application is to determine water contents in process fluids by means of capacitance measurements. This technique has also been extended to higher frequencies by Wasan and coworkers (173, 174). In the following we present a technically very important problem that combines a controlled reaction inside a W/O emulsion and dielec tric Spectroscopy as a process on-line instrumentation. This problem concerns the formation and transport of gas hydrates in pipelines.

Gas hydrates (clathrates) may technically be considered as an alternative form of ice that has the ability to entrap relatively large volumes of gas within cavities in the hydrate crystal matrix. The entrapped guest molecules (gas) stabilize the structure by means of van der Waals interactions, and combinations of the different unit cells give rise to structures I, II (175-177), and H (178). The most common gas to form gas hydrates is methane, but ethane, propane, butane, carbon dioxide, nitrogen, and many other types of gases may also give rise to gas hydrates.

When gas hydrates are formed in a W/O emulsion, the emulsified water is converted into clathrate structures and thus the volume fraction of free water in the emulsion droplets decreases. The formation of these new structures will alter the overall dielectric properties of the emulsion, and dielectric measurements can thus be used to follow the gas hydrate formation. In Fig. 41 this is illustrated with CCl_3F as the gas hydrate forming species in a nonionic W/O emulsion (179, 180). The decrease in the overall permittivity of the system is due to the transition of water from the liquid to the solid state (i.e., from free water to water bound in the hydrates). From the dielectric measurements we can extract information on the onset temperature for hydrate formation, induction time for the process, and so on. The permittivity level after the hydrate formation is completed is indicative of the ratio between liquid water and hydrate water, i.e., the amount of water converted into hydrate water can be readily found (179, 180).

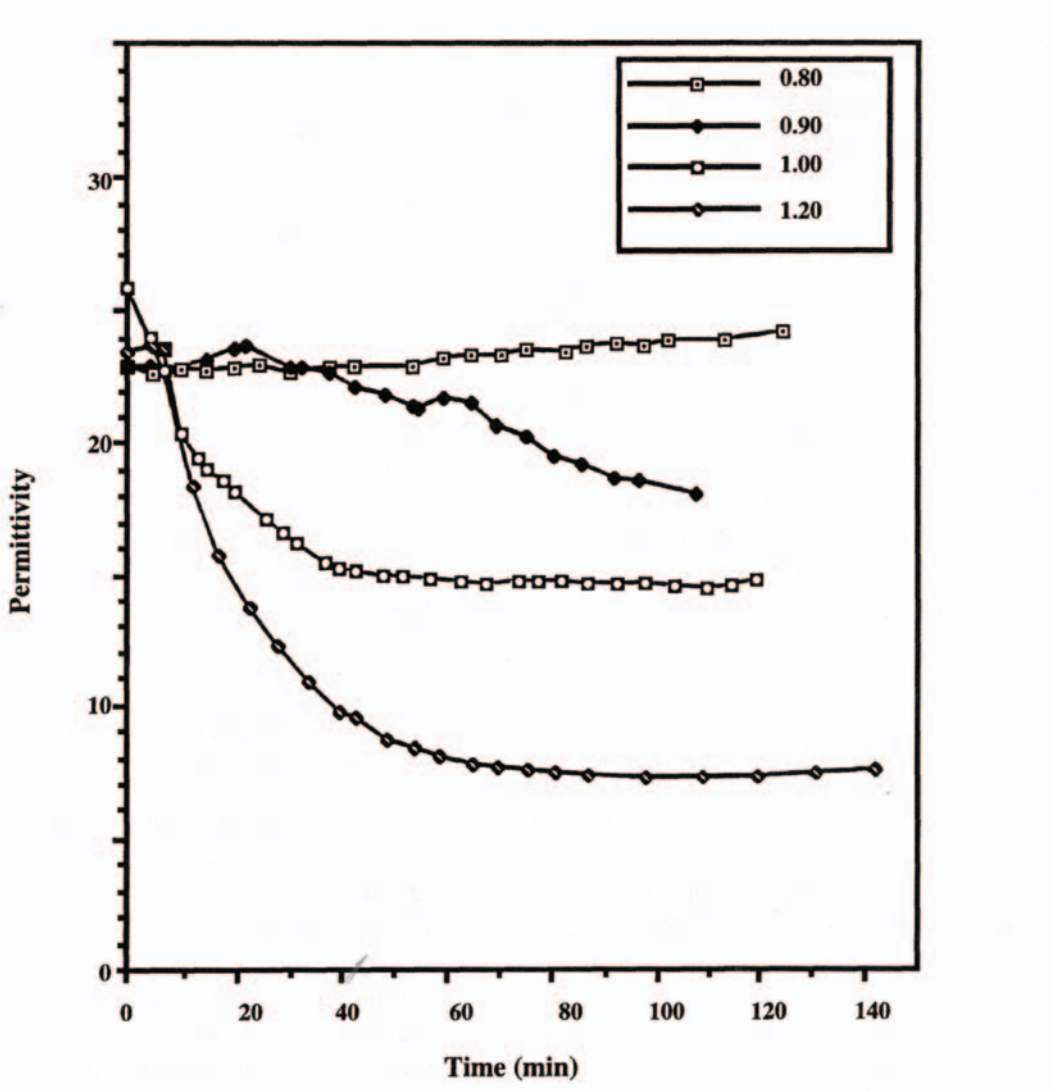

Figure 41 Static permittivity vs. time for clathrate hydrate formation in model W/O emulsions. The concentrations of $CC1_3F$ in H_2O were 0.80, 0.90, 1.00, and 1.20, respectively, times the theoretical molar fraction 1:17 expected to be found in the hydrates. (From Ref. 179.)

If the aqueous phase contains electrolytes, a relaxation due to the Maxwell-Wagner-Sillars effect will be observed. Since the electrolyte is not incorporated in the clathrate structures, an increased electrolyte concentration in the remaining free water will result, thus changing the dielectric relaxation mode. In Fig. 42 we note that the relaxation time r decreases from the initial 1000±100 ps to a final level of 200±20 ps during hydrate formation. The experimental value of 200 ps corresponds roughly to a 3% (w/v) NaCl solution, as compared with the initial salt concentration of 1% (w/v).

B. Suspensions

1. Sedimentation in Particle Suspensions

During sedimentation the volume fraction of suspended particles will increase near the bottom of the sample while the concentration of particles in the top layer will be correspondingly smaller. Information on the sedimentation rate and structure of the sediment layer can thus be extracted from dielectric measurements carried out at different levels of the sample.

The application of the TDS method for sedimentation studies may be illustrated with the studies carried out on two model systems, i.e., aqueous suspensions of SiO_2 and $A1_2O_3$ respectively. Figure 43 shows the permittivity spectra of $A1_2O_3$ in water as a function of the volume fraction of particulate matter. The most notable changes are in the static permittivity, which is also focused on in the following figures. Figure 44a shows the variation in static permittivity as a function of the volume fraction of SiO_2. The Hanai equation, Eq. (20), gives good estimates of the observed behavior. Figure 44b presents the corresponding data for $A1_2O_3$ and also in this case the Hanai model assuming spherical particles seems to describe the experimental data fairly well (181, 182).

In order to alter the sedimentation rate the surfaces of the SiO_2 and $A1_2O_3$ particles were modified through the adsorption of surfactants or polymers. The nonionic surfactant CgPhEOg and the nonionic polymer ethyl hydroxyethyl cellulose (EHEC) were used. Figure 45 gives the influence of pH on the sedimentation of Al_2O_3 in water for pure particles (Fig. 45a) and EHEC-coated particles (Fig. 45b). At pH 8.5 (i.e., close to the isoelectric point (IEP) for alumina) the sedimentation is fast and gives rise to a porous sediment (leading to a high final level of s). In contrast to this one can follow the slow sedimentation at pH 3.5 where we end up with a denser sediment and consequently a lower s. For the coated particles the effect of pH is rather small (182).

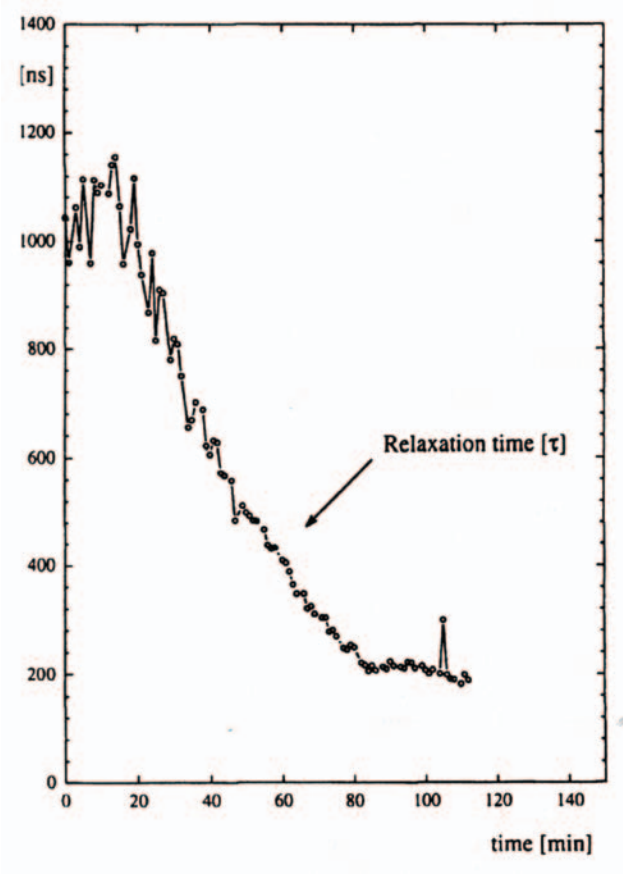

Figure 42 Relaxation time vs. time during clathrate hydrate formation. (From Ref. 179.)

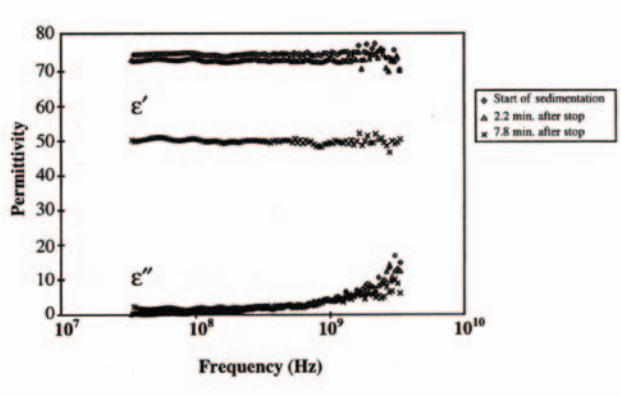

Figure 43 Dielectric spectra from an aqueous alumina particle suspension, recorded during sedimentation. (From Ref. 181.)

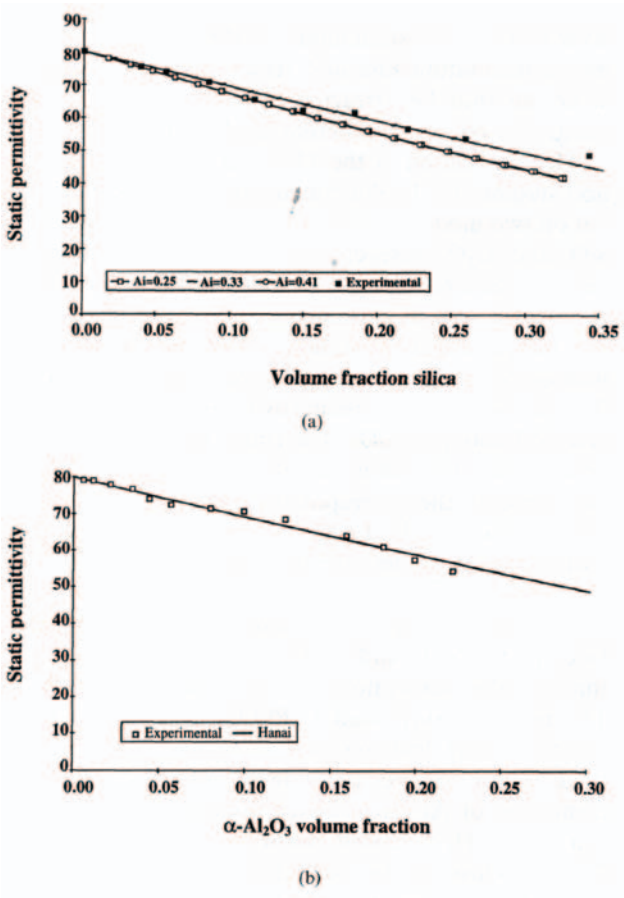

Figure 44 Static permittivity vs. volume fraction particles in aqueous suspensions: (a) silica particles, (b) alumina particles. (From Ref. 181.)

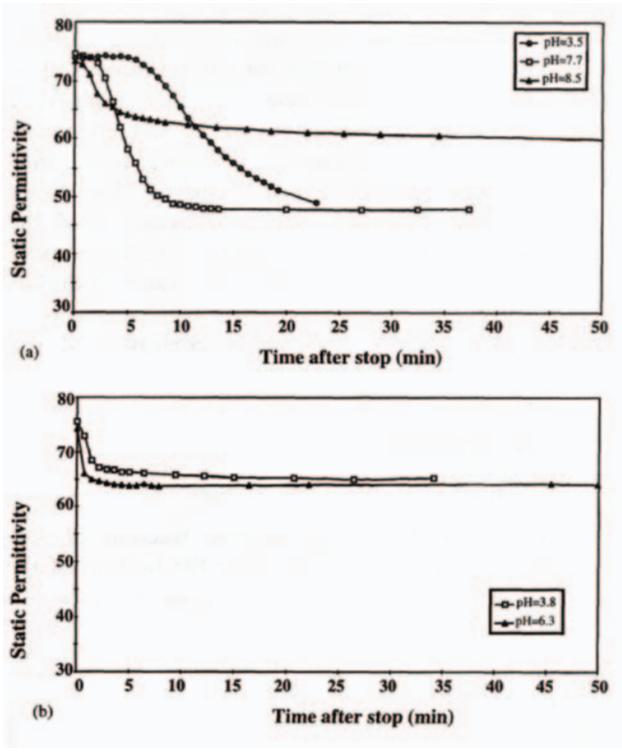

Figure 45 Static permittivity of particle suspensions vs. time, recorded during sedimentation. Measurements are performed in the bottom of the sedimentation cell, and at different pH conditions, (a) Alumina particles; (b) alumina particles coated with EHEC. (From Ref. 182.)

2. Magnetic Particles

Magnetically active monodisperse organic particles have found many technical applications especially within the separation and isolation of live cells and microorganisms. The magnetic particles are also almost perfect for sedimentation tests in applied magnetic fields, in as much as the degree of fiocculation may be controlled quite accurately. In Fig. 16 an experimental design for the dielectric study of aqueous suspensions of magnetic particles is displayed (86). In this survey, monodisperse polystyrene particles (2.8—4.5 |xm) containing 25% magnetic oxides have been used. When the particles are subjected to a magnetic field an induced flocculation takes place (Fig. 46). The next figure (Fig. 47) shows how the static permittivity changes with time (due to sedimentation) and with the strength of the applied magnetic field. The strength of the magnetic field will dictate the degree of flocculation. For single-particle sedimentation with a linear decrease in the static permittivity as a function of concentration, one would expect proportionality between the derivatives of volume fraction and permittivity versus time. From Fig. 47 we can observe that this is more or less always the case when the sedimentation occurs without the presence of a strong magnetic field, at least up to a period between 0 and maximally 5 min. In the presence of an external field this period is substantially shorter for low-volume fractions and substantially extended for high-volume fractions.

Two major effects will dictate the suspension behavior, i.e., the gravity-induced sedimentation and the bridging induced by the magnetic field. At lower volume fractions the distance between the particles is rather large, and the hindrance of settling is low. When a magnetic field is applied across the suspension there will be an instantaneous sedi-

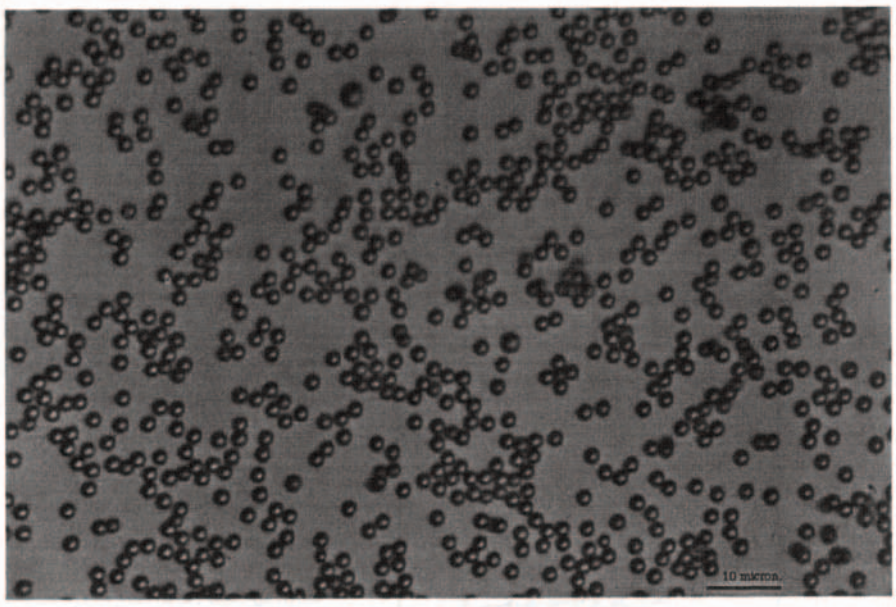

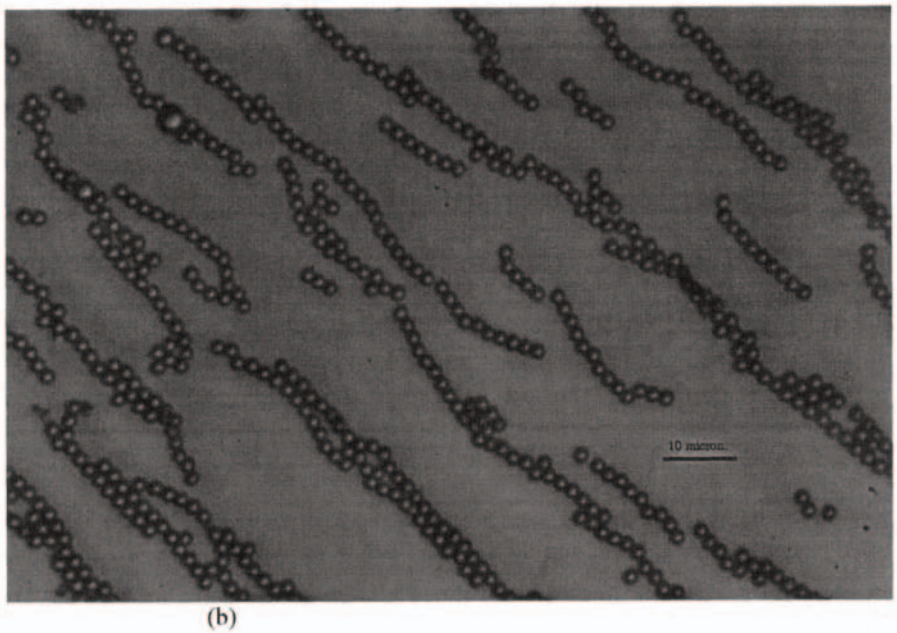

Figure 46 (a) Micrograph of polystyrene-based magnetic monodisperse particles; the particle diameter is 2.8 urn. (b) The particles are subjected to an external magnetic field. (From Ref. 86.)

mentation of small floes (as seen from Fig 47 with $\phi = 0.02$ and 0.05). At higher ϕ values the initial distance between the particles is much smaller and the bridging induced by the magnetic field may lead to a network formation resulting in a hindered sedimentation. This can be observed for $\phi = 0.20$ and 0.25. For a field of 0.4 T it takes about 5 min before the sedimentation sets in while a weaker field (0.1 T) can delay the sedimentation for 3.5 min. For the highest volume fraction ($\phi = 0.25$) no significant sedimentation is observed when the magnetic field is applied.

When the external magnetic field is applied the particles will, to a greater degree, flocculate and settle as flocs, giv-

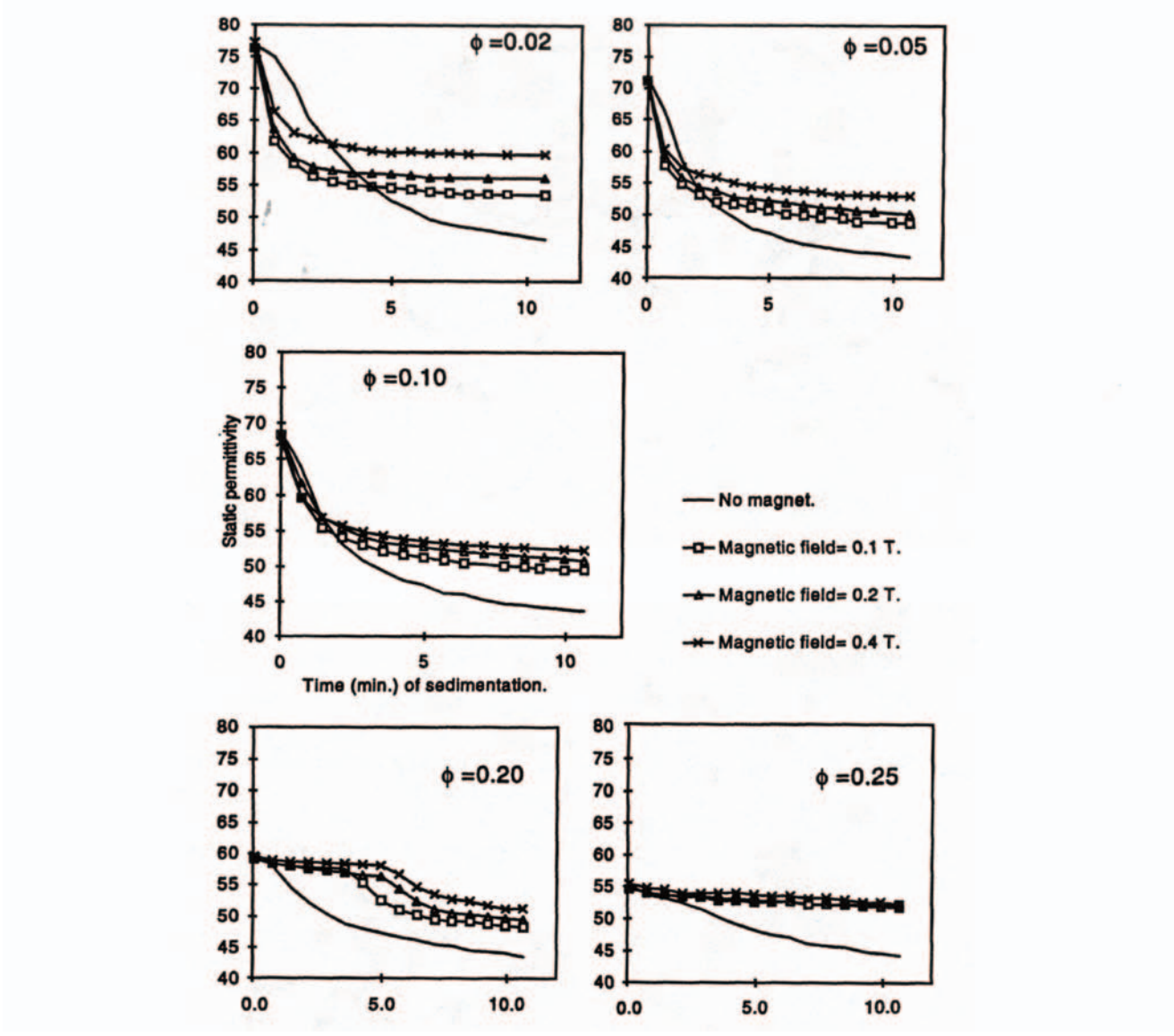

Figure 47 Static permittivity vs. time for suspensions containing the particles from Fig. (46) recorded during sedimentation. Different magnetic field strengths were applied, and the volume fraction particles were varied according to the legends. (From Ref. 86.)

ing a more porous bottom layer, as illustrated in Fig. 48. When the particles sediment individually the result is a more dense sediment. The porosity of the sediment is reflected in the level of the permittivity, a low permittivity in the sediment layer indicating a close packing of the particles.

By monitoring the dielectric properties of nonequilibrium systems a wide range of parameters describing the system may be deduced. However, more work of both a theoretical and experimental nature needs to be performed before we have a complete understanding of how the nonideal situations influence the dielectric parameters.

VI. DIELECTRIC STUDY OF HUMAN BLOOD CELLS

One of the important subjects in biophysics is the investigation of the dielectric properties of cells and the structural parts of the cells (i.e., membrane, cytoplasm, etc.). These can provide valuable knowledge about different cell struc-

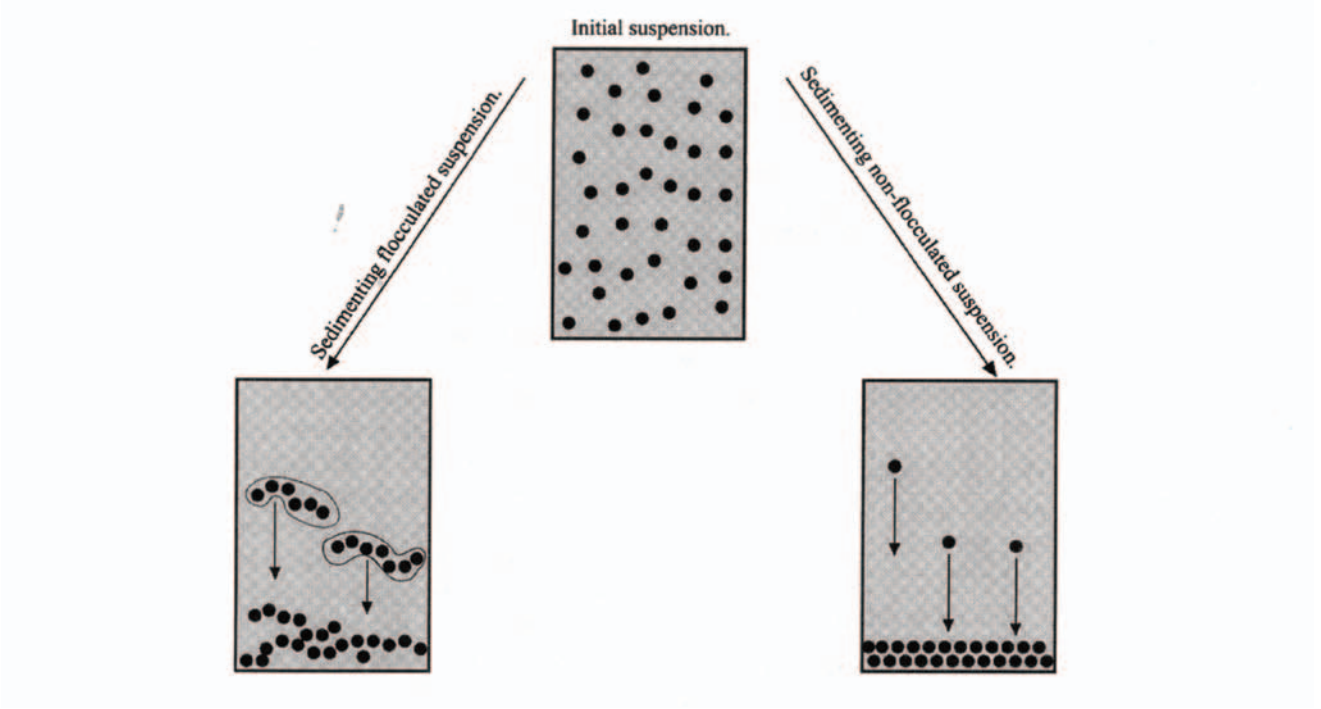

Figure 48 Schematic view on how flocculation may influence the nature of the sediments.

tures, their functions, and metabolic mechanisms.

The cell-suspension spectra are known to show a so-called β-dispersion (183), which is observed in the frequency range 100 kHz-10 MHz and can be interpreted as the interface polarization. This dispersion is usually described in the framework of different mixture formulas and shelled models of particles (14, 70, 72, 183, 184). In the example of biological cells, the interface polarization is connected to the dielectric permittivity and conductivity of the cell structural parts.

Before time-domain spectroscopy (TDS) methods were developed, investigations by frequency-domain methods were restricted by lack of techniques which allowed quick determination of the dielectric spectrum within the frequency range 10^5 10^{10} Hz (14, 64). It was quite difficult to ensure the stability of biological materials because of the long duration of the experiment. TDS allows one to obtain information on dielectric properties in a wide frequency range during a single measurement and hence to study unstable biological systems properly. This is also a much less time-consuming method, which requires very few devices to work with. Moreover, the sensitivity of the system allows one to study dilute solutions or suspensions of cells (volume fraction < 10%).

A. Cell and Cell-suspension Dielectric Models

For analysis of the dielectric properties of blood-cell suspensions, several classical models are usually used (11, 14, 185-201). For small volume fractions of cells the Maxwell-Wagner model is used, while for larger ones (see Sec. II) the Hanai formula would be preferable (14, 186). It was shown (70, 72) that for dilute suspensions of human blood cells the dielectric spectra of a single cell can be successfully calculated from the Maxwell model of suspension, according to the mixture formula [Eq. (19)]:

$$\varepsilon^*_{\text{mix}} = \varepsilon^*_{\text{sup}} \frac{(2\varepsilon^*_{\text{sup}} + \varepsilon^*_{\text{c}}) - 2p(\varepsilon^*_{\text{sup}} - \varepsilon^*_{\text{c}})}{(2\varepsilon^*_{\text{sup}} + \varepsilon^*_{\text{c}}) + p(\varepsilon^*_{\text{sup}} - \varepsilon^*_{\text{c}})} \tag{88}$$

where p is the cell volume fraction, $\varepsilon^*_{\text{mix}}$ is the effective complex dielectric permittivity of the whole mixture (suspension), $\varepsilon^*_{\text{sup}}$ is the complex dielectric permittivity of the supernatant, $s^*_{\text{sup}}(\varepsilon) = \varepsilon_{s,\text{sup}} - \sigma$, σ_{sup} is its conductivity, and ε^*_{c} is the effective complex dielectric permittivity of the average cell.

1. Single-shell Model of the Erythrocytes

The dielectric properties of the spherical erythrocyte can be described by the single-shell model (14, 70, 186). In this

model the cell is considered as a conducting homogeneous sphere (or ellipsoid) covered with a thin shell, much less conductive than the sphere itself (14, 186—189).

The expression for the complex dielectric permittivity [$\varepsilon_c^*(\omega)$] in the single-shell model contains five parameters: dielectric permittivity and conductivity of the cell membrane (ε_m and σ_m); dielectric permittivity and conductivity of the cell interior (cytoplasm) (ε_{cp} and σ_{cp}); and a geometrical parameter $v = (1 - d/R)^3$ where d is the thickness of the cell membrane and R is the radius of the cell. This expression is as follows (188):

$$\varepsilon_c^*(\omega) - \varepsilon_m^*(\omega)\frac{2(1-v)+(1+2v)E(\omega)}{2+v+(1-v)E(\omega)} \tag{89}$$

where $E(\omega) = \dfrac{\varepsilon_{cp}^*(\omega)}{\varepsilon_m^*(\omega)}$, $\varepsilon_{cp}^*(\omega) = \varepsilon_{cp} - i\dfrac{\sigma_{cp}}{\varepsilon_0\omega}$, $\varepsilon_m^*(\omega) = \varepsilon_m - i\dfrac{\sigma_m}{\varepsilon_0\omega}$, and ε_0 is the vacuum permittivity.

It is possible to show that the single-shell model equation can be presented as the sum of a single Debye process and a conductivity term:

$$\varepsilon_c^* = \varepsilon_\infty + \frac{\Delta\varepsilon}{1+i\omega\tau} + \frac{\sigma}{i\omega\varepsilon_0} \tag{90}$$

The last equation depends only on four parameters (△ - dielectric strength, τ - relaxation time, ε -dielectric permittivity at high frequency, and σ - the conductivity), which are functions of the dielectric and geometrical parameters of the single-shell models. This connection between the experimental presentation [Eq. (90)] and the single-shell model [Eq. (88)] formulas allows one to conclude that only four independent parameters are required to describe the spectrum of a single cell. The fifth parameter can be expressed in terms of ra these four parameters. Using the high- and low-frequency limits one can derive the following relations:

$$\varepsilon_{c_0}^* \cong \varepsilon_m\left(\frac{1+2v}{1-v}\right) - j\frac{\sigma_m}{\omega\varepsilon_0}\left(\frac{1+2v}{1-v}\right)\omega \to 0 \tag{91}$$

$$\varepsilon_{c\infty}^* \cong \varepsilon_{cp} - j\frac{\sigma_{cp}}{\omega\varepsilon_0}\omega \to \infty \tag{92}$$

By fitting the single-shell model to the experimental spectrum the following four parameter combinations can be obtained:

$$\varepsilon_m\left(\frac{1+2v}{1-v}\right);\ \sigma_m\left(\frac{1+2v}{1-v}\right);\ \varepsilon_{cp} \text{ and } \sigma_{cp} \tag{93}$$

The first two terms indicate that one of the three parameters (ε_m, σ_m, or υ) has to be obtained by an independent method and to be kept fixed during the fitting procedure, whereas the other two parameters can be fitted. Usually, the geometrical parameter v is fixed, since it can be calculated by using the values of the cell radius (R) and the cell membrane thickness (d), which are evaluated independently. The parameters ε_{cp} and σ_{cp} in set (93) can be calcualted directly from the fitting procedure.

It can be shown analytically that the expression for the model spectrum of a cell suspension represented by the combination of the Maxwell-Wagner formula and the single-shell model of cells can be rewritten as the sum of two Debye proceesses and a conductivity term. This is in contrast to the conclusions (190) that every interface of a shelled particle gives a single Debye-type dispersion. In the case of a one-shell particle suspension there are two interfaces. One of them is the interface between the cytoplasm and the cell membrane and the other one is the interface between the cell membrane and the suspending medium. However, Pauly and Schwan (202) have proven that for biological cells these two dispersions degenerate to only one relaxation process. Indeed, the numerical model experiment (203) has shown that the dielectric strength of the high-frequency process is about 2-3 orders of magnitude smaller than the dielectric strength of the low-frequency process and can therefore be neglected.

2. Double Shell Model of the Lymphocytes

It is well known that lymphocytes are spherical, and have a thin cell membrane and a spherical nucleus (surrounded by a thin nuclear envelope) that occupies about 60% of the cell volume (188). Therefore, the dielectric properties of lymphocytes can be described by the double-shell model (188, 190, 191) (see Fig. 49). In this model the cell is considered to be a conducting sphere covered with a thin shell, much less conductive than the sphere itself, in which a smaller sphere with a shell (i.e., the nucleus) is incorporated. In addition, one assumes that every phase has no dielectric losses and the complex dielectric permittivity can thus be written as:

$$\varepsilon_i^*(\omega) = \varepsilon_i - j\frac{\sigma_i}{\varepsilon_0\omega} \tag{94}$$

where ε_i, is the static permittivity and σ_t is the conductivity of every cell phase. The subscript i can denote "m" for membrane, "cp" for cytoplasm, "ne" for nuclear envelope, or "np" for nucleoplasm.

The effective complex dielectric permittivity of the whole cell (ε^*_c) is represented as a function of the phase

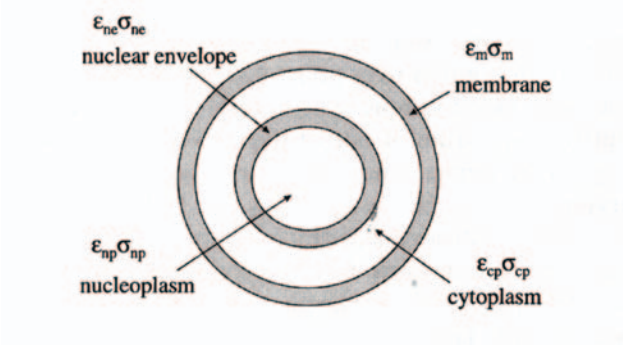

Figure 49 Schematic picture of the double-shell dielectric model of the cell. Every phase of the cell is described by the corresponding dielectric permittivity (ε) and conductivity (σ). (From Ref. 72. With permission from Elsevier B.V.)

parameters, i.e., the complex permittivities of cell membrane (ε^*_m), cytoplasm (ε^*_{cp}), nuclear envelope (ε^*_{ne}), and nucleoplasm (ε^*_{np}):

$$\varepsilon_c^* = \varepsilon_m^* \frac{1(1-v_1)+(1+2v_1)E_1}{(2+v_1)+(1-v_1)E_1} \tag{95}$$

where the geometrical parameter υ_1 is given by $v_1 = (1 - d/R)^3$, where d is the thickness of plasma membrane and R is the outer cell radius. The intermediate parameter, E_1, is given by

$$E_1 = \frac{\varepsilon_{cp}^*}{\varepsilon_m^*} \frac{2(1-v_2)+(1+2v_2)E_2}{(2+v_2)+(1-v_2)E_2} \tag{96}$$

where $\upsilon_2 = [Rn/(R - d)]^3$, R_n being the outer radius of the nucleus. Finally, E_2 is given by

$$E_2 = \frac{\varepsilon_{ne}^*}{\varepsilon_{cp}^*} \frac{2(1-v_3)+(1+2v_3)E_3}{(2+v_3)+(1-v_3)E_3} \tag{97}$$

where $\upsilon_3 = (1 - d_n/R_n)^3$, $E_3 = \varepsilon^*_{np}/\varepsilon^*_{ne}$, d_n being the thickness of the nuclear envelope.

In the double-shell model every structural part of the cell (cell membrane, cytoplasm, nuclear envelope, and nucleoplasm) can be described by two parameters - permittivity and conductivity. Therefore, a cell is described by eight dielectric phase parameters, and there are three geometrical parameters that are a combination of thickness of outer and internal membranes with radii of nucleus and cell. Thus, as it seems, we could obtain all 11 parameters from the fitting of a one-cell spectrum by the double-shell equation. However, it can be demonstrated that some of the parameters are not independent in this model.

In the multishell model every shell gives rise to an additional Debye process with two extra parameters (190). Thus, in the case of the double-shell model, which contains eleven parameters, the spectrum of a suspension can be written as a sum of two Debye processes with conductivity, which includes only six parameters. This means that only six parameters from the total 11 in the double-shell model are arguments that can be fitted. The other five parameters have to be measured by independent methods and have to be fixed in the fitting process. In the fitting procedure, described elsewhere (72, 203), the radius of a cell, the thickness of both membranes, and the permittivity of cytoplasm and nucleoplasm were all fixed.

The specific capacitance of the cell membrane can be calculated directly from the cell suspension spectrum by using the following formula, derived from the Hanai-Asami-Koisumi model (192):

$$C_m = \frac{2}{3}\frac{\varepsilon_0}{R}\frac{\varepsilon_{mix(low)}}{(1-(1-p)^{3/2})} \tag{98}$$

where $\varepsilon_{mix(iow)}$ is the low-frequency limiting value of the dielectric permittivity (static permittivity) of the suspension.

B. Protocol of Experiment, Fitting Details, and Statistical Analysis

The whole procedure of the human blood-cell suspension study is presented schematically in Fig. 50. The TDS measurements on the cell suspension, the volume-fraction measurement of this suspension, and measurements of cell radius are excecuted during each experiment on the sample. The electrode-polarization correction (see Sec. II) is performed at the stage of data treatment (in the time domain) and then the suspension spectrum is obtained. The single-cell spectrum is calculated by the Maxwell-Wagner mixture formula [Eq. (88)], using the measured cell radius and volume fraction. This spectrum is then fitted to the single-shell model [Eq. (89)] in the case of erythrocytes or to the double-shell model [Eqs (94)-(98)] to obtain the cell-phase parameters of lymphocytes.

In the fitting procedure for lymphocytes, the following parameters were fixed: the radius of the measured cell; the cell membrane thickness (d = 7 nm) (188); the nuclear envelope thickness (d_n = 40 nm) (188, 191); and the ratio of the nucleus radius to the cell radius ($R_nR = (0.6)^{1/3}$). These four values represent only three geometrical parameters of the double-shell model (188, 190, 191). Two other fixed parameters were the dielectric permittivity of the cytoplasm (ε_{cp} = 60) (188) and the dielectric permittivity of the nucleoplasm (enp = 120); enp was chosen as the middle value from the range presented in other papers (188, 191). More-

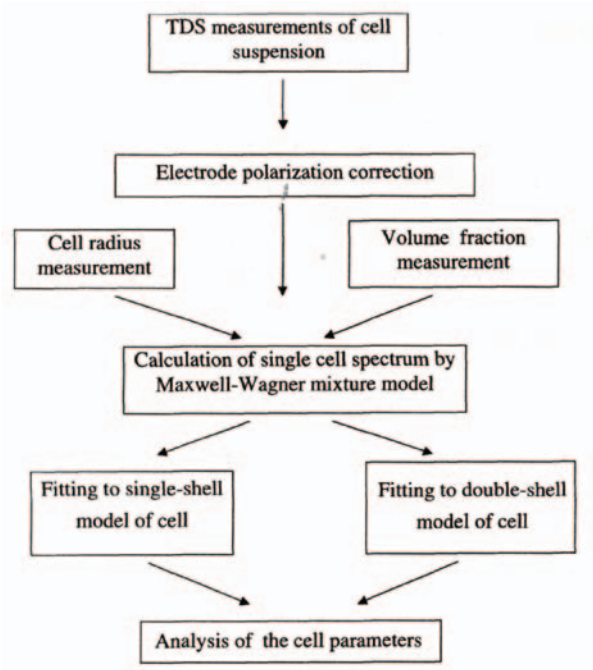

Figure 50 Flow chart of the whole protocol of human blood-cell suspension study.

over, numerical evaluations and evidence in Refs 188 and 191 have shown that the suspension spectrum is almost insensitive to changes in the ε_{cp} and ε_{np} parameters from 30 up to 300. Students' *t*-test (201) was usually applied to analyze the results of the fittings.

C. Erythrocytes and Ghosts

The erythrocyte and erythrocyte ghost suspensions are very similar systems. They differ in their inner solution (in the case of erythrocytes it is an ionic hemoglobin solution; in the case of ghosts it is almost like the surrounding solution they were in while they were sealed). The cell sizes in a prepared suspension depend both on the ion concentration in the supernatant and in the cell interior (70). Thus, the dielectric spectra of erythrocytes and erythrocyte ghost suspensions have the same shape, which means that there are no additional (except Maxwell-Wagner) relaxation processes in the erythrocyte cytoplasm; thus, the single-shell model (Eq. 89) can be applied.

The frequency dependence of the effective dielectric permittivity of a single "average" erythrocyte was calculated for both samples, according to Eq. (88). The spectra obtained were almost identical, as was expected since both samples were prepared from erythrocytes of the same blood sample. The normalized dielectric permittivity spectrum of one of them (No. 1) is shown in Fig. 51 by points. The relaxation process for a single erythrocyte can be described by the Debye equation. The effective dielectric permittivity spectra of an "average" erythrocyte were fitted to the single-shell model equation [Eq. (89)] and the phase parameters of the cell were found. The fitted normalized dielectric spectrum is given in Fig. 51 by a solid line.

The membrane dielectric permittivity em was evaluated from fitting with an accuracy of ±0.05 (70). The membrane conductivity could not be estimated from the fitting as far as it was less than the accuracy limits, so it was set to zero. Insufficient accuracy of the inner phase dielectric permittivity es allows only estimates of the lower and upper limits of its value. The inner phase conductivity at was found with an accuracy of ±0.01 S/ m. The dimensionless parameter v was found with an accuracy of ±1 × 10~4.

As regards the ghosts, their membrane dielectric permittivity em is that of the erythrocytes they were prepared from. The inner phase conductivity at of ghosts varied in

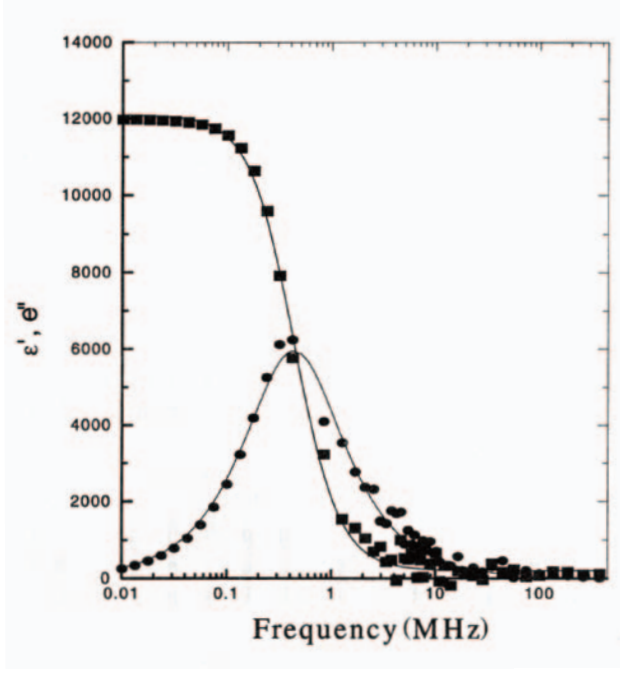

Figure 51 Dielectric permittivity spectrum of the "average" erythrocyte fitted to the single-shell model. Experimental results are figured by points, and the fitting results by a solid line. (From Ref. 70. With permission from Elsevier Science B.V.)

correspondence with the conductivity of the supernatant they were placed in. The parameter υ depends both on the supernatant conductivity and on the ghost preparation method.

The limits of the phase parameter variation of different erythrocytes and ghosts at room temperature are given in Table 3. The dielectric permittivities of the erythrocyte membranes are found to be distributed near 5 (Fig. 52). The erythrocyte membrane thickness was found to be 3.1 nm, assuming an average radius of 2.7 μm. This result is in good agreement with that obtained by Fricke (193, 194).

Thus, it was shown that one could apply the mixture equation [Eq. (88)] and the single-shell model [Eq. (89)] to dilute solutions of ghosts and erythrocytes. The membrane dielectric permittivity, cytoplasm conductivity, and geometric parameter υ for each kind of cell were calculated. The next step was to use this approach for the dielectric property study of normal and pathological blood cells.

Table 3 Limits of Phase Parameters' Variation for Different Erythrocytes and Ghosts at Room Temperature

	ε_m	$v\left(1-\frac{d}{R}\right)^3$	d (nm) Independent measurement ($R = 2.7$ μm)
Erythrocytes	~ 5	~ 0.9967	~ 3.1
Ghosts	~ 4.8	~ 0.9967	~ 3.1

Source: Ref. 70 (with permission from Elsevier Science B.V.).

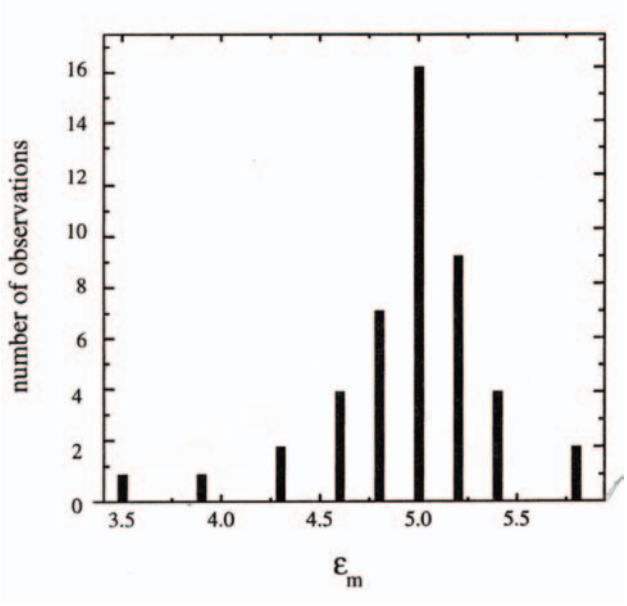

Figure 52 Distribution of the observed values of the erythrocyte membrane dielectric permittivity. (From Ref. 70. With permission from Elsevier Science B.V.)

D. Lymphocytes

1. Description of Measured Cell Samples

Nine cell populations were investigated (72): normal peripheral blood T cells, normal tonsillar B cells, peripheral blood B cells, which were transformed by infection with Epstein-Barr Virus (EBV) (Magala line), malignant B cell lines (Farage, Raji, Bjab, and Daudi) and malignant T cell lines (Peer and HDMAR). The sizes of the cells were determined by using a light microscope. The typical size distribution is shown in Fig. 53. The volume fractions were measured with a micro-centrifuge (Haematocrit) and corrected for the intercellular space, which was determined with Dextran Blue, and found to be 20.2 ± 3.2% of the volume of the pellet (204, 205). The cell populations with corresponding names of diseases, the mean value of cell radii and the volume fractions are presented in Table 4.

2. Dielectric Properties of Measured White Blood Cells

Typical examples of single cell spectra obtained for studied cell lines by the procedure described above are presented in Fig. 54. One can see that the spectra of the various cell lines are different. It should be mentioned that the transition from the suspension spectrum to a spectrum of a single average cell leads to a noise increase that is especially noticeable at high frequencies. This phenomenon is the result of the nonlinearity of Eq. (88), which was used for this calculation. In particular, the parameters for the nucleus envelope, cytoplasm, and nucleoplasm (presented in Table 5) are connected with the high frequency of the cell spectrum; therefore, these parameters were obtained with a relatively low accuracy.

The specific capacitance of a cell membrane was estimated from the value of the state permittivity of the suspension spectra by the relationship Eq. (94). This value is proportional to the ratio of the cell membrane permittivity to the membrane thickness ε_m/d, according to the formula of a plate capacitor, i.e., $Cm = \varepsilon_m\varepsilon_o/d$. Both the capacitance C_m and ratio, ε_m/d, are presented in Fig. 55. Note that in this study we are not able to evaluate the permittivity and

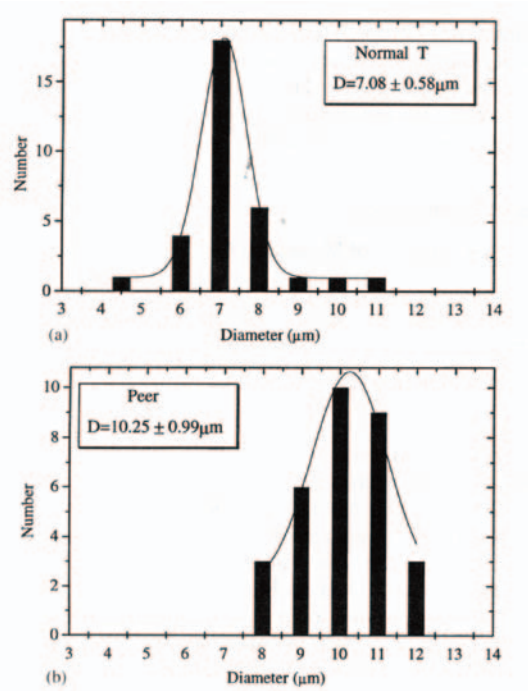

Figure 53 Typical size distributions for normal (a) and malignant (b) lymphocytes. The results of fitting by Gauss distribution function are shown by the solid line; D is the mean diameter of cells. (From Ref. 72. With permission from Elsevier Science B.V.)

the thickness of the cell membrane independently.

One can see (Table 5; Fig. 55) that the membrane capacitance (or the similar parameter ε_m/d) has different values for the different cell populations. These parameters for B-normal cells exceed by 11% the values for the T-normal ones. Even more dramatic is the difference between the value of the membrane capacitance of the normal cells and that for all the malignant cells.

For B lymphocytes the capacitance of the normal cells is higher than that of all the malignant cells. The same parameter for the EBV-transformed line (Magala) is intermediate between the values for normal and malignant cells. According to statistical analysis by the t-test, the difference between transformed (Magala) and malignant lines is statistically significant (t-test gives the probability $0.01 < Pr < 0.02$), whereas there is no statistically significant difference between the nondividing (B normal) and transformed (Magala) populations ($Pr > 0.2$).

As for the T-cell population, the membrane capacitance of the malignant cells (see Fig. 55) was smaller than that of the normal T cells. However, this difference was borderline statistically significant ($0.05 < Pr < 0.1$).

As can be seen in Fig. 56 and Table 5 the membrane conductivities of normal cells of both the B and T populations were significantly higher than for that of malignant and

Table 4 List of Cell Populations Studied

Cells	Radius (μm)	Number of experiments	Volume fraction of suspension (%)	Disease
B cells				
B-normal[a]	3.3	3	1.7–3.2	–
Magala	5.3	2	5.2–7	EBV immortalized
Farage	5.2	5	4.4–8.56	Non-hodgkin's lymphoma
Raji	6.4	4	4.4–6.96	Burkitt's lymphoma
Bjab	6.3	3	2–6.4	Burkitt's lymphoma
Daudi	6.8	4	2.8–6.2	Burkitt's lymphoma
T cells				
T normal[b]	3.4	2	4	–
Peer	5.1	4	2.8–6.96	Acute lymphocytic leukemia
HDMAR	5.9	2	2.8–5.2	Hodgkin's lymphoma

[a]Tonsillar B cells.
[b]Peripheral blood T cells.
Source: Ref. 72 (with permission from Elsevier Science B.V.).

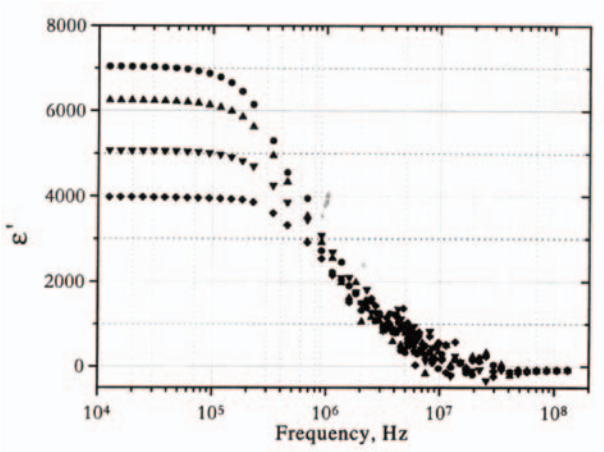

Figure 54 The real part of complex dielectric permittivity for differnt cell populations calculated from experimental suspension spectra by Maxwell-Wagner mixture model: (●) Magala; (▲) Raji; (▼) Bjab; (◆) HDMAR. (From Ref. 72. With permission from Elsevier Science B.V.)

transformed cells. In the B-cell group, the membrane conductivity of normal cells was about six times larger than that of the average value of the malignant cell lines and the transformed cells. This difference is statistically highly significant (Pr<0.01). No significant difference in the conductivity between the transformed and malignant cells in the B population were found (Pr>0.2). Concerning the conductivity of T cells, the difference between normal and malignant cells was not so large as for B cells, but it was statistically significant (0.01<Pr<0.02).

The ε_{ne} value of normal B cells is about 1.3 times larger than the average value of other lines of this group (Table 5). Statistically, the difference is borderline significant (0.05 < Pr < 0.1).

There is a difference in the B group between normal B cells and the malignant cell lines, which is statistically high significant (0.01 <Pr). The normal T cells value is more than twice the average of the malignant cell lines (Table 5) and the difference is statistically significant (0.01 < Pr < 0.02).

The conductivity of normal B cells is larger by a factor of 1.8 than that of the average of the malignant cell lines (Table 5). This difference is statistically highly significant (Pr<0.01). There is no difference in this parameter between the average of the malignant cell lines and that of the transformed cell lines. There is almost no difference between normal T cells and malignant T cells.

The normal B-cell value is larger by a factor of 1.6 or more than that of the average value of the malignant cells (Table 5), and it is statistically significant (0.01<Pr<0.02). There is a small difference between normal T cells and the average malignant cells, but this difference is statistically not significant (0.2 <Pr).

It is interesting to note that the conductivity of nucleoplasm is about twice that of the cytoplasm for almost all cell populations.

Table 5 Dielectric Parameters[a] of Cell Structural Parts for All Cell Populations Studied

	ε_m	σ_m ($\times 10^{-6}$S/m)	ε_{ne}	σ_{ne} ($\times 10^{-3}$S/m)	σ_{ep} (S/m)	σ_{np} (S/m)
B normal	12.8 ± 1.6	56 ± 29	106 ± 35	11.1 ± 72	1.31 ± 0.08	2.04 ± 0.29
Magala	11.4 ± 2.4	8.8 ± 0.7	72.5 ± 11.6	3.7 ± 0.9	0.55 ± 0.2	1.08 ± 0.03
Farage	9.8 ± 1.1	9.1 ± 1.4	60.3 ± 22.6	4.4 ± 2.5	0.48 ± 0.14	1.07 ± 0.43
Raji	8.8 ± 1.1	8.2 ± 0.6	79.9 ± 34.4	4.0 ± 1.6	0.58 ± 0.02	1.02 ± 0.25
Bjab	8.0 ± 0.7	11.0 ± 5.3	108 ± 35	2.1 ± 0.7	0.88 ± 0.11	1.39 ± 0.54
Daudi	7.2 ± 0.7	9.5 ± 1.4	66.1 ± 7.5	2.7 ± 0.3	0.85 ± 0.09	1.44 ± 0.35
T cells						
T normal	11.1 ± 1.4	27.4 ± 6.2	85.6 ± 16.7	8.8 ± 0.6	0.65 ± 0.13	1.26 ± 0.27
Peer	9.5 ± 0.7	12.9 ± 3.6	61.6 ± 17	2.1 ± 0.6	0.81 ± 0.09	1.42 ± 0.2
HDMAR	7.4 ± 1.2	14.5 ± 4	101.2 ± 55.3	3.0 ± 0.2	0.88 ± 0.25	1.58 ± 0.28

[a]Fitting procedure was performed by fixing the following parameters: ε_{ep}= 60; ε^{np}= 120; d = 7 nm; d_n= 40 nm, R_n= $R(0.6)^{1/3}$
Source: Ref. 72 (with permission from Elsevier Science B.V.).

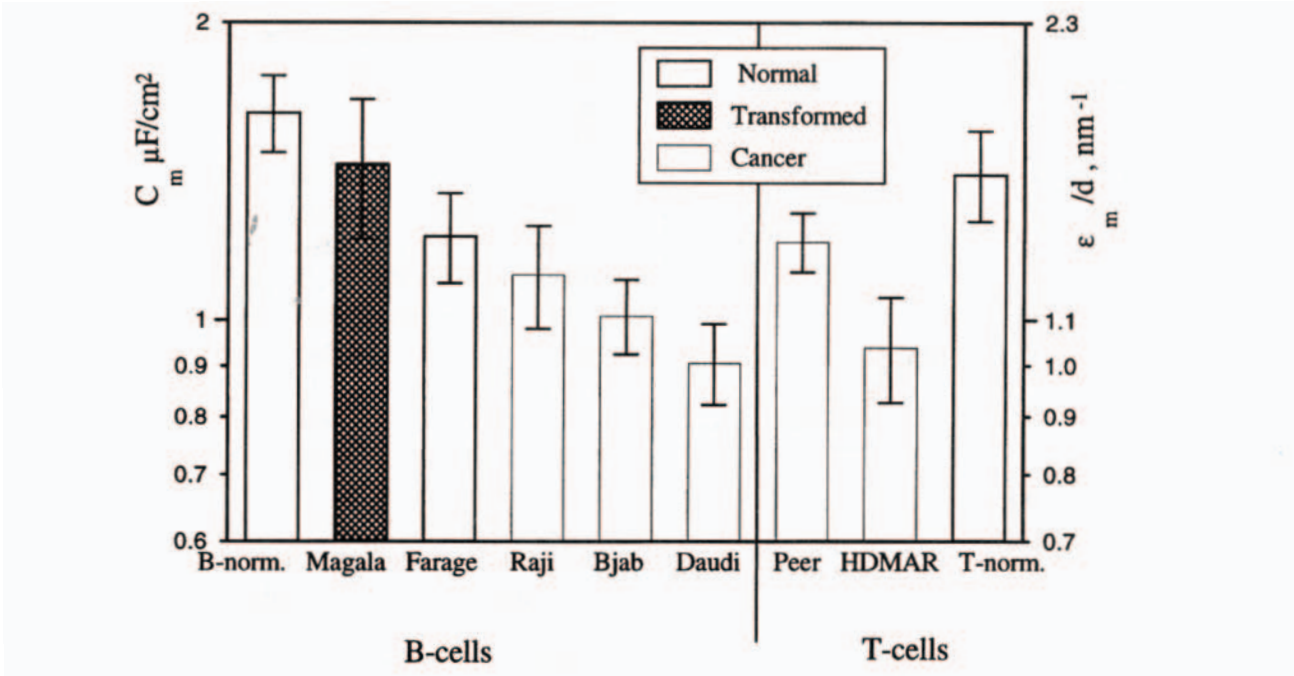

Figure 55 Capacitance of cell membrane and ratio of dielectric permittivity of the cell membrane thickness (ε_m/d) for all cell populations under investigation. Shown are the mean values of the results ± SD. (From Ref. 72. With permission from Elsevier Science B.V.)

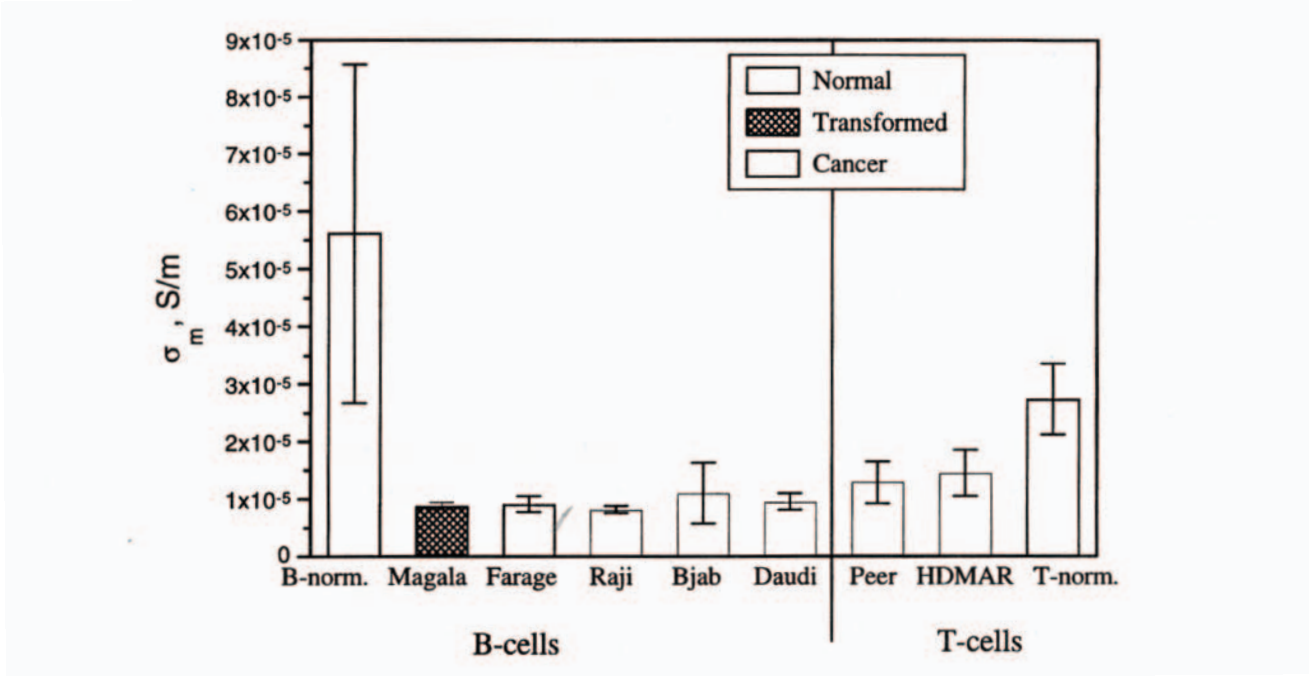

Figure 56 Conductivity of cell membrane for all populations under investigation. Shown are the mean values of the results ±SD. (From Ref. 72. With permission from Elsevier Science B.V.)

3. Main Features of Dielectric Response of Pathological Cells

The various dielectric parameters of the cell populations presented in Table 5 were obtained with cells suspended in a low-conductivity medium, in which the major components were sucrose and glucose rathr than salts. The reason for using this medium was to decrease the electrode polarization. A priori, this choice of medium raises questions about the state of the cells as compared to their native state, in which they are immersed in a solution containing salts and proteins. One can expect at least two kinds of changes when cells are transferred to a medium of low ionic strength. First, a direct change in the cell membrane integrity, and second, changes in the ionic environment within the cell due to disturbances in the cybernetic mechanism of ion regulation. Another question is whether different normal and malignant cell populations will react similarly to an alteration of the ionic strength of the environment. If changes do occur in the cells, it is important to determine their rate.

Glascoyne et al. (206) followed the change in conductivity of the medium and the leakage of K^+ after suspending various cells in low-conductivity medium. The half-time of the increase in conductivity (90% of the cation flux was of K^+ ions) was roughly 20 to 30 min, which corresponds to the value obtained by Hu et al. (200) with murine B and T lymphocytes.

In our experiments the complete measurement cycle (three repetitions) for each cell line took about 10 min and was made as soon as cells were suspended in the low-conductivity medium. Results of three successive measurements of the conductivity show very small change (noise level) of that parameter for both normal and malignant cell suspensions (72). This means that neither the ionic composition of the cells nor the cell membrane integrity changed considerably during the time required for the measurements (about 10 min) (72). This was consistent with the results of More et al. (207), Hu et al. (200), and Gascoyne et al. (206).

Furthermore, the size distribution of the cells and the microscopic morphology did not change in a noticeable way, even after an hour of suspension in the low ionic strength medium (72). It was the same as that of cells kept in their growth medium. This implies that no large changes in the intracellular ion composition occurred as a result of the suspension (208).

Our findings are consistent with the microscopic observations made by Hu et al. (200) on B and T murine lymphocytes. They also tested possible damage by the low ionic strength medium by determining the proportion of the cells that were permeable to propidium iodide. Their findings indicated that the resuspension of normal and malignant cells for not more than 10 min did not seem to effect in a considerable way the state of neither the normal nor the malignant cells.

Normal, EBV-transformed and malignant lymphocytes were recently investigated (72). Normal lymphocytes do not live for a prolonged time in culture and do not divide without addition of mitogenic stimuli. One of the methods used to immortalize lymphoid cells, so that they can live and divide under culture conditions, is to transform them with a virus such as the EBV virus. The Magala B cell line was developed in this way. Transformed cells and malignant cells share the capacity to divide in culture. Malignant cells differ from normal and transformed cells by numerous additional features. In our experiments both B- and T-cell populations could be characterized by two positive/ negative properties - malignant or nonmalignant nature of the cells (cancer/noncancer), and the capacity or lack of capacity to divide (dividing/nondividing). Thus, the EBV-transformed Magala cells are noncancerous but dividing, while Farage, Raji, Bjab, Daudi, Peer, and HDMAR lines are malignant and can divide in culture. Classifying the cells in this manner and by using the t-test, the analysis of cell parameters was carried out,

Analysis of cell membrane capacitance (see Fig. 55) has shown that this parameter is different for various cell populations. For the B lymphocytes the capacitance of membranes of normal cells is higher than that of all malignant cells. The same parameter for the EBV-transformed line (Magala) is intermediate between the values for normal and malignant cells. This probably reflects the fact that this transformed line possesses the same dividing feature as cancer cells, but it is really noncancerous. The difference between transformed (Magala) and malignant lines is statistically significant, whereas there is no statistically significant difference between the nondividing (normal) and transformed (Magala) populations. Thus, it is reasonable to assume that in the B-cell population the decrease in specific capacitance of the cell membrane is more strongly correlated with cancer than with the dividing feature. As for the T-cell population, the membrane capacitance of the malignant cells (see Fig. 55) was smaller than that of the normal T cells. This difference was of borderline statistical significance. However, the trend of decrease in cell membrane capacitance associated with malignancy is the same as within the B-cell group. Yet, at present, it is not possible to draw strong conclusions as in the case of the B-cell group; also, there is a lack of measurements on transformed T cells. This difficulty is true also for other parameters, even

if the difference between normal T cells and the malignant ones is statistically significant.

Now let us consider the conductivity of the cell membranes (72). One can see in Fig. 56 that the membrane conductivity of normal cells of both the B and T populations was significantly higher than for that of malignant and transformed cells. There was no notable difference in the conductivity between the transformed and malignant cells in the B-cell population. Thus, in the B-cell population the decrease in cell membrane conductivity seemed to result from the dividing properties of the cells rather than from acquisition of malignant properties. Concerning the conductivity of T cells, the difference between normal and malignant cells was not so large as for B cells, but was statistically significant. Note again that no measurements for T transformed cells were performed.

For normal B cells (see Table 5) σ^{ne}, σ^{cp}, and σ^{np} are higher than for the other cell populations. Concerning the parameters of transformed cells they are in the value range of cancer cells. Thus, the dividing feature which is imminent to cancer cells as well as to transformed cells seems to be responsible for the change in these parameters in B populations.

It would be important to understand in molecular terms the mechanisms underlying the difference in the various dielectric parameters that were measured. Parameters such as conductivity and permittivity reflect the distribution of free and bound charges, in membranes, respectively, and also the polarizability of various components.

The average ionic composition of T and B human lymphocytes in the quiescent state is K^+: 130—150 mM; Na^+: 15—30 mM; Cl^-: 70—90 mM; and $Ca^{2+} \sim 0.1$ μM. This composition has also been found in B-CLL lymphocytes (chronic lymphocytic leukemia) (209, 210). Averaging the conductivity of the cyto-plasmic σ_{cp} and the nucleoplasmic σ_{np} (Table 5) of the normal B lymphocytes it was shown to have a value of 130 mM for KC1 (72). Thus, as a first approximation, data on the conductivity of the inner cell solution are consistent with an assumption that the conductivities of the cytoplasm and the nucleoplasm are mainly as a result of the ionic species K^+, Cl^-, and Na^+ in aqueous media.

We want to note the fact that the conductivity of the cytoplasm is consistently lower by a factor of ~2 than that of the nucleoplasm. This was invariably found in all B- and T-cell lines, both normal and malignant (Table 5). If the conductivity of either the cytoplasm or nucleoplasm indeed expresses mainly the transport of small ions, such as K^+, Cl^-, and Na^+ in an aqueous environment, then there must be a selective barrier between the above two phases, which is very likely the nuclear envelope (NE).

The NE of eukaryotic cells is made up of two concentric membranes, the inner and the outer envelope membrane (211). They are separated by the perinuclear space, but fuse at specific points, where they form the nuclear pore complex. The nuclear pore is composed of up to 100 different proteins, arranged in two octagonal arrays. The nuclear pores are believed to regulate the bidirectional nucleocytoplasm transport of macromo-lecules, such as mRNA, transcription factors, proteins, etc., which is a process that requires metabolic energy. This means that they indeed act as diffusion barriers. The open inner diameter of the pore was shown to be approximately 90 A. The large diameter of nuclear pores has led to the conclusion that the nuclear pores are unable to regulate fluxes of ions (diameter of 3 to 4 A) or maintain a gradient of ions across the NE. Studies, using the "patch-clamp" technique, have detected ion-channels' activity at the NE (212, 213). These findings put into focus the regulation of nuclear ions by the NE. Several classes of K^+-selective ion channels were recorded by patch-clamp techniques, with conductances of 100 to 550 pS in nuclei of different cells. Also a large, cation-selective ion channel with a maximum conductance of 800 pS in 100 mM KC1 was detected. This channel is a possible candidate for the open nuclear pore, as its conductance is consistent with the geometrical dimension of the open pore. It is important to notice that this channel is open only for short times, and is mainly in the closed mode. These findings are consistent with older data (213) on micro-electrode studies with in-situ nuclei, which claimed to measure a potential difference across the NE and reported low electrical conductance of that membrane complex.

The findings that the NE acts as a diffusion barrier can explain the fact that the nucleoplasm and the cytoplasm can have a different steady-state conductivity and probably also different compositions.

As shown in Table 5, the electrical conductivity of the NE is larger by two orders of magnitude than that of the cell membrane. We would then expect that the numbers of ionic channels and their nature, including their gating mechanism, would then be very different in these two types of cellular membranes.

The ability of the noninvasive TDS technique to analyze in situ the properties of the intracellular structures is very important. If indeed the two-shell model represents also the NE and the nucleoplasm, then it describes the very regions of the cell where the putative control of cell division resides, and also the region where the gene expression takes place. Electrical methods are relatively easy to apply (72, 214) and can lead the molecular biologist to decipher more

rationally the control mechanism of cell growth in situ.

ACKNOWLEDGMENTS

The University of Bergen (Foundation for Senior Research Fellowship) is thanked for a grant to Professor Yuri Feldman, facilitating his contribution to this review during his stay in Bergen. The Flucha program, financed by the Norwegian Research Council (NFR) and the oil industry, is also acknowledged for financial support.

REFERENCES

1. H Frohlich. Theory of dielectrics. Dielectric constant and Dielectric Loss. 2nd ed. Oxford: Clarendon Press, 1958.
2. CJF Bottcher. Theory of Electric Polarization, Vol 1. 2nd ed. Amsterdam: Elsevier Science B.V., 1993.
3. CJF Bottcher, P Bordewijk. Theory of Electric Polarization, Vol 2. 2nd ed. Amsterdam: Elsevier Science B.V., 1992.
4. NE Hill, WE Yaughan, AH Price, M Davis. Dielectric Properties and Molecular Behavior. London: Van Nostrand, 1969.
5. N Kozlovich, Yu Alexanadrov, A Pusenko, Yu Feldman. Colloids Surfaces A 140: 229-312, 1998.
6. S Havriliak, SJ Havriliak. Polymer 37: 4107, 1996.
7. RR Nigmatullin, YE Ryabov. Phys Solid State. 39: 87, 1997.
8. L Nivanen, R Nigmatullin, A LeMehaute. Le Temps Irreversible a Geometry Fractale. Paris: Hermez, 1998.
9. RH Cole. Dielectric Polarization and Relaxation. NATO ASI Ser., Ser. C, Vol 135. Molecular Liquids, 1984, p 59—110.
10. Yu D Feldman, VV Levin. Chem Phys Lett 85: 528, 1982.
11. T Hanai. Kolloidn Zh. 177: 57, 1960.
12. SS Dukhin, VN Shilov. Dielectric Phenomena and the Double Layer in Disperse Systems and Polyelectrolytes. trans., D Lederman. New York: Halsted Press, 1974.
13. R Pethig. Dielectric and Electronic Properties of Biological Materials. Chichester: John Wiley, 1979.
14. S Takashima. Electric Properties of Biopolymers and Membranes. Bristol: Adam Hilger, 1989.
15. B Nettelblad, GA Niklasson. J Mater Sci 32: 3783, 1997.
16. EM Trukhan. Soviet Phys - Solid State. 4: 2560, 1963.
17. TS Sorensen. J Colloid Interface Sci 168: 437, 1994.
18. JC Maxwell. A Treatise of Electricity & Magnetism, articles 310-314. New York: Dover, 1954 (originally Clarendon Press, 1891).
19. KW Wagner. Arch Electrotech 2: 371, 1914.
20. H Fricke, HJ Curtis. J Phys Chem 41: 729, 1937.
21. RW Sillars. J Inst Electr Engrs 80: 378, 1937.
22. DAG Bruggemann. Ann Phys Lpz 24: 636, 1935.
23. T Hanai. In: P Sherman, ed. Emulsion Science. New York: Academic Press, 1968.
24. C Boned, J Peyrelasse. Colloid Polymer Sci 261: 600, 1983.
25. MH Boyle. Colloid Polymer Sci 263: 51, 1985.
26. P Debye, E Hiickel. Phys Z 24: 185, 1923.
27. J Sjöblom, B Jonsson, C Nylander, I Lundstrom. J Colloid Interface Sci 96: 504, 1983.
28. J Lyklema, SS Dukhin, VN Shilov. J Electroanal Chem 143: 1, 1983.
29. JF Rathman, JF Scamehorn. J Phys Chem 88: 5807, 1984.
30. C Grosse, KR Foster. J Phys Chem 91: 3073, 1987.
31. R Barchini, DA Saville. J Colloid Interface Sci 173: 86, 1995.
32. G Schwarz. J Phys Chem 66: 2636, 1962.
33. RH Cole, JG Berberian, S Mashimo, G Chryssik, A Burns, E Tombari. J Appl Phys 66: 793, 1989.
34. S Mashimo, T Umehara, T Ota, S Kuwabara, N Shinyashiki, S Yagihara. J Molec Liquids 36: 135, 1987.
35. D Bertolini, M Cassettari, G Salvetti, E Tombari, S Veronesi. Rev Sci Instrum 61: 450, 1990.
36. R Nozaki, TK Bose. IEEE Trans Instrum Meas 39: 945, 1990.
37. B Gestblom, E Noreland, J Sjöblom. J Phys Chem 91: 6329, 1987.
38. Yu Feldman, A Andrianov, E Polygalov, G Romanychev, I Ermolina, Yu Zuev, B Milgotin. Rev Sci Instrum 67: 3208, 1996.
39. A Schonhals, F Kremer, E Schlosser. Phys Rev Lett 67: 999, 1991.
40. U Kaatze, V Lonneckegabel, R Pottel. Z Phys Chem (Int J Res Phys) 175: 165, 1992.
41. K Folgere, T. Friiso, J Hilland, T Tjomsland. Meas Sci Technol 6: 995, 1995.
42. JG Berberian. J Molec Liquids 56: 1, 1993
43. B Gestblom, P Gestblom. Macromolecules 24: 5823, 1991.
44. YuD Feldman, YuF Zuev, EA Polygalov, VD Fedotov. Colloid Polymer Sci 270: 768, 1992.

45. N Miura, N Shinyashiki, S Yagihara, M Shiotsubo. J Am Ceram Soc 81: 213, 1998.
46. Yu Feldman, V Levin. Chem Phys Lett 85: 528, 1982.
47. AM Bottreau, A Merzouki. IEEE Trans Instrum Meas 42: 899, 1993.
48. EK Miller, ed. Time Domain Measurements in Electromagnetics. New York: Van Nostrand Reinhold, 1986.
49. NE Hager III. Rev Sci Instrum 65: 887, 1994.
50. O Götmann, U Kaatze, P Petong. Meas Sci Technol 7: 525, 1996.
51. JG Berberian, RH Cole. Rev Sci Instrum 63: 99, 1992.
52. B Gestblom, H Fordedal, J Sjöblom. J Disp Sci Technol 15: 449, 1994.
53. T Skodvin, T Jakobsen, J Sjöblom. J Disp Sci Technol 15: 423, 1994.
54. GQ Jiang, WH Wong, EY Raskovich, WG Clark, WA Hines, J Sanny. Rev Sci Instrum 64: 1614, 1993.
55. T Jakobsen, K Folgerϕ. Meas Sci Technol 8: 1006, 1997.
56. YJ Lu, HM Cui, J Yu, S Mashimo. Bioelectromagnetics 17: 425, 1996.
57. S Naito, M Hoshi, S Mashimo. Rev Sci Instrum 67: 3633, 1996.
58. JZ Bao, ST Lu, WD Hurt. IEEE Trans Microwave Theory Technol 45: 1730, 1997.
59. T Skodvin, J Sjöblom. Colloid Polym Sci 274: 754, 1996.
60. MS Seyfried, MD Murdock. Soil Sci 161: 87-98, 1996.
61. JM Anderson, CL Sibbald, SS Stuchly. IEEE Trans Microwave Theory Technol 42: 199, 1994.
62. DV Blackham, RD Pollard. IEEE Trans Instrum Meas 46: 1093, 1997.
63. HP Schwan. Ann NY Acad Sci 148: 191, 1968.
64. EH Grant, RJ Sheppard, GP South. Dielectric Behavior of Biological Molecules in Solution. Oxford: Clarendon Press, 1978.
65. J Lyklema. Fundamentals of Interface and Colloid Science. Vol II. Solid-Liquid Interfaces. London: Academic Press, 1995.
66. J O'M Bockris, AKN Reddy. Modern Electrochemistry. Vol 2. New York: Plenum Press, 1977.
67. HP Schwan. Ann Biomed Eng 20: 269, 1992.
68. HP Schwan. Physical Techniques in Biological Research. Vol 6. New York: Academic Press, 1963.
69. CL Davey, GH Marks, DB Kell. Eur Biophys J 18: 255, 1990.
70. R Lisin, B Ginzburg, M Schlesinger, Yu Feldman. Biochim Biophys Acta 1280: 34, 1996. 71. Yu Feldman, R Nigmatullin, E Polygalov, J Texter. Phys Rev E 58: 2179, 1998.
72. Yu Polevaya, I Ermolina, M Schlesinger, B-Z Ginzburg, Yu Feldman. Biochim Biophys Acta 1419: 257-271, 1999.
73. I Ermolina, V Fedotov, Yu Feldman. Phisica A 249: 347, 1998.
74. RR Nigmatullin, in The Proceedings of Bordeaux Summer School-Geometrie Fractale et Hyperbolique. Derivation Fractionnaire et Fractale 3—8 July 1994. Fractals, Solutions and Chaos 11: 1994.
75. T Pajkossy, L Nyikos. Phys Rev B 42: 709, 1990.
76. T Pajkossy. J Electroanal Chem 364: 111, 1994.
77. T Pajkossy, AP Borosy, A Imre, SA Martemyanov, G Nagy, R Schiller, L Nyikos. J Electroanal Chem 366: 69, 1994.
78. SH Liu, Phys Rev Lett 55: 529—532, 1985.
79. T Kaplan, LJ Gray. Phys Rev B 32: 7360, 1985.
80. RM Hill, LA Dissado, RR Nigmatullin. J Phys Condens Matter 3: 9773, 1991.
81. K Oldham, J Spanier. The Fractional Calculus. New York: Academic Press, 1974.
82. M Stromme, A Niklasson, CG Granqvist. Phys Rev B 52: 14192, 1996.
83. JB Hasted. Aqueous Dielectrics. London: Chapman and Hall, 1973.
84. EH Grant, TJ Buchanan, HF Cook. J Chem Phys 26: 156, 1957.
85. B Gestblom, S Urban. Z Naturforsch 50a: 595, 1995.
86. B Pettersen, T Skodvin, J Sjöblom. Colloids Surfaces A 143: 323, 1998.
87. SE Friberg. Microemulsions: Structure and Dynamics. Boca Raton, FL: CRC Press, 1987. 88. B Lindman, ed. Surfactants, Adsorption, Surface Spectroscopy and Disperse Systems. Darmstadt: Steinkopff, 1985.
89. D Langevin, Annu Rev Phys Chem 43: 341, 1992.
90. J Sjöblom, R Lindberg, SE Friberg. Adv Colloid Interface Sci 95: 125, 1996.
91. U Olsson, K Shinoda, B Lindman. J Phys Chem 90: 4083, 1986.
92. PG DeGennes, C Touplin. J Phys Chem 86: 2294, 1982.
93. R Strey, MJ Jonströmer. J Phys Chem 96: 4537, 1992.
94. R Kahlweit, R Strey and G Busse. J. Phys. Chem., 95, 5344, 1991.
95. MA Dijk, G Casteleijn, JGH Joosten, YK Levine. J Chem Phys 85: 626, 1986.
96. Yu Feldman, N Kozlovich, I Nir, N Garti. Phys Rev E 51: 478, 1995.
97. Yu Feldman, N Kozlovich, Y Alexandrov, R Nigmatullin, Y Ryabov. Phys Rev E 54: 5420, 1996.
98. C Cametti, P Codastefano, P Tartaglia, S Chen, J Rouch. Phys Rev A 45: R5358, 1992.
99. F Bordi, C Cametti, J Rouch, F Sciortino, P Tartaglia. J Phys: Condens Matter A19: 8, 1996.
100. C Boned, J Peyrelasse, Z Saidi. Phys Rev E 47: 468, 1993.
101. A Ponton, TK Bose, G Delbos. J Chem Phys 94: 6879, 1991.
102. A D'Aprano, G D'Arrigo, A Paparelli. J Phys Chem 97: 3614, 1993.
103. M Wasserman. Russ Chem Rev 63: 373, 1994.

104. F Mallamace, N Micali, C Vasi, G D'Arrigo. Phys Rev A 43: 5710, 1991.
105. F Sicoli, D Langevin. J Phys Chem 99: 14819, 1995.
106. M Clausse. In: P Becher, ed. Encyclopedia of Emulsion Technology. Basic Theory. Vol 1. New York: Marcel Dekker, 1983.
107. Yu Feldman, N Kozlovich, I Nir, N Garti, V Archipov, Z Idiyatullin, Y Zuev, V Fedotov. J Phys Chem 100: 3745, 1996.
108. JA Beunen, E Ruckenstein. J Colloid Interface Sci. 96: 469, 1983.
109. E Ruckenstein, JA Beunen. Langmuir 4: 77, 1988.
110. HF Eicke, M Bercovec, B Das-Gupta. J Phys Chem 93: 314, 1989.
111. DG Hall, J Phys Chem 94: 429, 1990.
112. SI Chou, DO Shah. J Phys Chem 85: 1480, 1981.
113. C Cametti, P Codastefano, P Tartaglia. Ber Bunsenges Phys Chem 94: 1499, 1990.
114. J Peyrelasse, C Boned. J Phys Chem 89: 370, 1985.
115. MA Dijk, JGH Joosten, YK Levine, D Bedeaux. J Phys Chem 93: 2506, 1989.
116. J Lang, A Jada, A Malliaris. J Phys Chem 92: 1946, 1988.
117. N Kozlovich, A Puzenko, Yu Alexandrov, Yu Feldman. Phys Rev E 58: 2179, 1998.
118. M D'Angelo, D Fioretto, G Onori, L Palmieri, A Santucci. Phys Rev E 52: R4620, 1995.
119. M D'Angelo, D Fioretto, G Onori, L Palmieri, A Santucci. Phys Rev E 54: 993, 1996.
120. G Giammona, F Goffrede, V Turco Liveri, G Vassallo. J Colloid Interface Sci 154: 411, 1992.
121. P Huang Kenez, G Carlström, I Furo, B Halle. J Phys Chem 96: 9524, 1992.
122. M Tomic, N Kallay. J Phys Chem 96: 3874, 1992.
123. P Karpe, E Ruckenstein. J Colloid Interface Sci 137: 408, 1990.
124. M Boas. Mathematical Methods in Physical Sciences. New York: John Wiley, 1983, p 12.
125. M Belletete, M Lachapelle, G Durocher. J Phys Chem 94: 5337, 1990.
126. ALR Bug, SA Safran, GS Grest, I Webman. Phys Rev Lett 55: 1896, 1985.
127. G Grest, I Webman, S Safran, A Bug. Phys Rev A 33: 2842, 1986.
128. C Cametti, P Codastefano, A Di Biasio, P Tartaglia, S Chen. Phys Rev A 40: 1962, 1989.
129. J Klafter, A Blumen. Chem Phys Lett 119: 377, 1985.
130. J Klafter, MF Shlesinger. Proc Natl Acad Sci USA 83: 848, 1986.
131. D Stauffer, A Aharony. Introduction to Percolation Theory. Revised 2nd edn. London: Taylor & Francis, 1994.
132. D Vollmer, J Vollmer, HF Eicke. Europhys Lett 26: 389, 1994.
133. D Vollmer. Europhys Lett 27: 629, 1994.
134. BB Mandelbrot. The Fractal Geometry of Nature. New York: Freeman, 1982.
135. F Feder. Fractals. New York: Plenum Press, 1988.
136. S-H Chen, J Rouch, F Sciortino, P Tartaglia. J Phys: Condens Matter 6: 10855, 1994.
137. A Bunde, S Havlin, J Klafter, G Graff, A Shehter. Phys Rev Lett. 78: 3338, 1997.
138. LH Peebles, Jr. Molecular Weight Distributions in Polymers. New York: Wiley-Interscience, 1971.
139. RR Nigmatullin. J Appl Magn Reson 14: 601, 1998.
140. Yu Alexandrov. Dielectric Spectroscopy Investigation of Dynamic and structural properties of microemulsions. Thesis. Jerusalem, 1998.
141. Yu Feldman, N Kozlovich, I Nir, N Garti. Colloids Surfaces A 128: 47, 1997.
142. J Sjöblom, B Gestblom. J Colloid Interface Sci 115: 535-544, 1987.
143. Yu Feldman, N Kozlovich, I Nir, A Aserin, S Ezrahi, N Garti. J Non-Crystal Solids 172—174: 1109, 1994.
144. SC Mehrotra, B Gestblom, J Sjöblom. Finn Chem Lett 34: 87, 1985.
145. E Noreland, B Gestblom, J Sjöblom. J Solution Chem 18: 303, 1989.
146. MK Kreoger. J Molec Liquids 36: 101, 1987.
147. PC Brot. Ann Phys 2: 714, 1957.
148. SK Garg, CP Smyth. J Phys Chem 69: 1294, 1965.
149. VV Levin, YuD Feldman. Chem Phys Lett 87: 162, 1982.
150. M Fukuzaki, U Toshihiro, D Kurita, S Shioya, M Haida, S Mashimo. J Phys Chem 96: 1087, 1992.
151. Y Marcus. Cell Biochem Function 13: 157, 1995.
152. U Kaatze. J Solution Chem 28: 1049, 1997.
153. J Sjöblom, B Gestblom. In: SE Friberg, B Lindman, eds. Organized Solutions. Surfactants in Science and Technology. New York: Marcel Dekker, 1992, p 193.
154. A Kraszewski. J Microwave Power 12: 215, 1977.
155. A Kraszewski, S Kulinski, M Matuszewski. J Appl Phys 47: 1275, 1976.
156. N Kozlovich, I Nir, B Tsentsiper, VI Zhuravlev, A Aserin, S Ezrahi, N Garti, Yu Feldman. J Surfc Sci Technol. in press.
157. N Garti, A Aserin, S Ezrahi, I Tiunova, G Berkovic. J Colloid Interface Sci 178: 60, 1996.
158. K Asami, T Hanai. Colloid Polymer Sci 270: 78, 1992.
159. ID Chapman. J Phys Chem 75: 537, 1971.
160. B-M Sax, G Schon, S Paasch, MJ Schwuger. Progr Colloid Polymer Sci 77: 109, 1988.
161. T Hanai. Kolloidn Zh 171: 23, 1960.
162. T Hanai. Kolloidn Zh 175: 62, 1961.
163. U Genz, JA Helsen, J Mewis. J Colloid Interface Sci. 165: 212, 1994.
164. J Sjöblom, T Skodvin, T Jakobsen, SS Dukhin. J Disp Sci Technol 15: 401, 1994.
165. T Skodvin, J Sjöblom, JO Saeten, O Urdahl, B Gestblom. J Colloid Interface Sci 166: 43, 1994.

166. T Skodvin, J Sjöblom. J Colloid Interface Sci 182: 190, 1996.
167. T Hanai, K Sekine. Colloid Polymer Sci 265: 888, 1986.
168. T Skodvin, J Sjöblom, JO Saeten, T Warnheim, B Gestblom. Colloids Surfaces A 83: 75, 1994.
169. J Sjöblom, T Skodvin, T Jakobsen. J Disp Sci Technol 15: 423, 1994.
170. H Fordedal, J Sjöblom. J Colloid Interface Sci 181: 1996, 589—594.
171. G Capuzzi, P Baglioni, CMC Gambi, EY Sheu. Phys Rev E 60: 792, 1999.
172. J Peyrelasse, M Moha-Ouchane, C Boned. Phys Rev A 38: 904, 1988.
173. C Thomas, JP Perl, DT Wasan. J Colloid Interface Sci 139: 1, 1990.
174. JP perl, HW Bussey, DT Wasan. J Colloid Interface Sci 108: 528, 1985.
175. M von Stackelberg. Naturwissenschaften 11: 327, 1949.
176. M von Stackelberg, HR Mviller. Z Elektrochem 58: 25, 1954.
177. M von Stackelberg, W Jahns. Z Elektrochem 58: 162, 1954.
178. JA Ripmeester, JS Tse, CI Ratcliffe, BM Powell. Nature 325: 135, 1987.
179. T Jakobsen, J Sjöblom, P Ruoff. Colloids Surfaces A 112: 73, 1996.
180. J Sjöblom, H Fϕrdedal, T Jakobsen, T Skodvin. In: KS Birdi, ed. Handbook of Surfactants. Boca Raton, FL: CRC Press, 1997.
181. B Pettersen, J Sjöblom. Colloids Surfaces A 113: 175, 1996.
182. B Pettersen, L Bergftϕdt, J Sjöblom. Colloids Surfaces A 127: 175, 1997.
183. HP Schwan. Adv Biol Med Phys 5: 147, 1957.
184. F Bordi, C Cametti, A Rosi, A Calcabrini. Biochim Biophys Acta 1153: 77—88, 1993.
185. H Looyenga. Physica 31: 401, 1965.
186. T Hanai, K Asami, N Koizumi. Bull Inst Chem Res Kyoto Univ 57: 297, 1979.
187. K Asami, T Hanai, N Koizumi. Jap J Appl Phys 19: 359, 1980.
188. K Asami, Y Takahashi, S Takashima. BBA 1010: 49, 1989.
189. K Asami, A Irimajiri. Biochim Biophys Acta 778: 570, 1984.
190. A Irimajiri, T Hanai, A Inouye. J Theor Biol 78: 251, 1979.
191. A Irimajiri, Y Doida, T Hanai, A Inouye. J Mem Biol. 38: 209, 1978.
192. K Asami, Y Takahashi, S Takashima. Biophys J. 58: 143, 1990.
193. H Fricke. Nature 4381: 731, 1963.
194. H Fricke. J Phys Chem 57: 934, 1953.
195. R Pethig, DB Kell. Phys Med Biol 32: 933, 1987.
196. A Surowiec, SS Stuchly, C Izaguirre. Phys Med Biol 31: 43, 1986.
197. FF Becker, X-B Wang, Y Huang, R Pethig, J Vykoukal, PRC Gascoyne. Proc Natl Acad Sci USA 92: 860, 1995.
198. A Irimajiri, K Asami, T Ichinowatari, Y Kinoshita. Biochim Biophys Acta 869: 203, 1987.
199. A Irimajiri, K Asami, T Ichinowatari, Y Kinoshita. Biochim Biophys Acta 896: 214—223, 1987.
200. X Hu, WM Arnold, U Zimmerman. Biochim Biophys Acta 1021: 191-200, 1990.
201. GW Snedecor, WG Cochran. Statistical methods. Ames, IA: The Iowa State College Press, 1956.
202. H Pauly, P Schwan. Z Naturforsch 14b: 125, 1959.
203. I Ermolina, Yu Polevaya, Yu Feldman. Eur Biophys J Biophy 29: 141—145, 2000.
204. M Ginzburg, B-Z Ginzburg. Biochim Biophys Acta 584: 398, 1979.
205. A Zmiri, Z Ginzburg. Plant Sci Lett 30: 211, 1983.
206. PRC Gascoyne, R Pethig, JPH Burt, FF Becker. Biochim Biophys Acta 1149: 119—120, 1993.
207. R More, I Yron, S Ben-Sasson, DW Weiss. Cellular Immunol 15: 382, 1975.
208. BCK Rossier, K Geeringh, JP Kraehenbuhl. Trends Biochem Sci 12: 483, 1987.
209. GB Segal, MA Lichtman. J Cell Physiol 93: 277, 1977.
210. S Grinstein, J Dixon. Physiol Rev 69: 417, 1989.
211. C Dingwell, R Laskey. Science 258: 942, 1992.
212. AJM Matzke, AM Matzke. Bioelectrochem Bioenergetics 25: 357, 1991.
213. JO Bustamente. J Mem Biol 138: 105, 1994.
214. MT Santini, C Cametti, PL Indovina, G Morelli, G Donelli. J Biomed Mater Res 35: 165, 1997.